Fakultät für Medizin

II. Medizinische Klinik und Polyklinik

Klinikum rechts der Isar

The role of mutant phosphoinositide 3-kinase p110α in liver and bile duct cancer

Angelika Gertraud Kroemer

Vollständiger Abdruck der von der Fakultät für Medizin der Technischen Universität München zur Erlangung des akademischen Grades eines

Doctor of Philosophy (Ph.D.)

genehmigten Dissertation.

Vorsitzende/r: Univ.-Prof. Dr. Jürgen Ruland

Betreuer/in: apl. Prof. Dieter Karl Maximilian Saur

Prüfer der Dissertation:

1. Priv.-Doz. Dr. Günter Schneider
2. apl. Prof. Dr. Klaus-Peter Janssen

Die Dissertation wurde am 01.07.2015 bei der Fakultät für Medizin der Technischen Universität München eingereicht und durch die Fakultät für Medizin am 27.08.2015 angenommen.

Table of contents

List of tables

List of figures

Abbreviations

×g	times gravity
°C	degree Celsius
µF	microfarad
µg	microgram
µl	microliter
µM	micromolar
µm	micrometer
4E-BP1	eIF4E-binding protein 1
A	alanine
AdCMV-Cre	adenovirus expressing Cre under control of the cytomegalovirus promoter
ADM	acinar-to-ductal metaplasia
AKT	protein kinase B
Alb	albumin
APC	adenomatous polyposis coli
ARAF	A-raf proto-oncogene, serine/threonine kinase
ARID2	AT rich interactive domain 2
Atf4	activating transcription factor 4
BAD	BCL2-associated agonist of cell death
BilIN	biliary intraepithelial neoplasia
bp	base pair
BRAF	B-raf proto-oncogene, serine/threonine kinase
BSA	bovine serum albumin
CAG	CMV-IE enhancer/chicken beta-actin/rabbit beta-globin hybrid promoter
caggs	chicken beta-actin promoter/CMV enhancer/beta-actin intron/bovine globin pA hybrid promoter
Catnb	β-catenin gene
CBD	common bile duct
CCC	cholangiocellular carcinoma
CD	cluster of differentiation
Cdkn2a	cyclin-dependent kinase inhibitor 2A
CK19	cytokeratin 19
cm	centimeter
c-met	met proto-oncogene
c-myc	myelocytomatosis viral oncogene homologue
CO_2	carbon dioxide
CRAF	v-raf-leukemia viral oncogene 1
D	aspartic acid
d	day

DNA	deoxyribonucleic acid
dH_2O	distilled water
dl	deciliter
DMSO	dimethyl sulfoxide
dNTP	deoxynucleotide
DTA	diphtheria toxin A
E	embryonic day
E	glutamic acid
E2F	E2F transcription factor
EDTA	ethylenediaminetetraacetic acid
EGFP	enhanced green fluorescent protein
EGFR	epidermal growth factor receptor
eIF4-E	eukaryotic translation initiation factor 4E
ER	estrogen receptor
erbB2	erb-b2 receptor tyrosine kinase 2
ERK	extracellular regulated MAP kinase
ERT	ER containing G521R mutation
ERT2	ER containing G400V/M543A/L540A mutations
ES cell	embryonic stem cell
et al.	et alii
f	flox
fmol	femtomol
FOXO	forkhead box O transcription factor
FSF	frt-stop-frt
G	glycine
g	gram
GAB	GRB2-associated binding protein
GAP	GTPase activating proteins
GDP	guanosine diphosphate
GEMM	genetically engineered mouse model
GRB2	growth factor receptor-bound protein 2
GSK3β	glycogen synthase kinase 3 β
GTP	guanosine triphosphate
GTPase	guanosine triphosphate hydrolase
H	histidine
h	hour
H&E	hematoxylin and eosin
H_2O_2	hydrogen peroxide
HBV	hepatitis B virus
HCC	hepatocellular carcinoma
HCV	hepatitis C virus
HepPar1	hepatocyte paraffin 1

HRAS	Harvey Rat Sarcoma viral oncogene homolog
IPN-B	intraductal papillary neoplasm of the bile duct
IR	insulin receptor
K	lysine
kb	kilo-base pair
KRAS	Kirsten Rat Sarcoma viral oncogene homolog
l	liter
LB	Luria Broth
LSL	loxP-stop-loxP
M	molar
M	methionine
MAPK	mitogen activated protein kinase
MEF	mouse embryonic fibroblast
MEK	mitogen activated protein kinase kinase
mg	milligram
min	minute
ml	milliliter
MLL3	mixed-lineage leukemia 3
mM	millimolar
mm	millimeter
MMF	Midazolam, Medetomidine, Fentanyl
mRNA	messenger RNA
mTOR	mechanistic target of rapamycin
mTORC	mammalian target of rapamycin complex
myr	myristoylated
NAFLD	Nonalcoholic Fatty Liver Disease
NASH	Nonalcoholic Steatohepatitis
NICD	Notch 1 intracellular domain
NRAS	Neuroblastoma Rat Sarcoma viral oncogene homolog
NSCLC	non-small cell lung cancer
o/n	over night
OD	optical density
ORF	open reading frame
P	postnatal day
p	phospho
p	p-value
p70S6K	ribosomal protein S6 kinase, 70kDa
p110α	phosphatidylinositol-4,5-bisphosphate 3-kinase, catalytic subunit alpha
pA	polyadenylation sequence
PanIN	pancreatic intraepithelial neoplasia
PBS	phosphate buffered saline
PCR	polymerase chain reaction

PDAC	pancreatic ductal adenocarcinoma
PDK1	3-phosphoinositide-dependent protein kinase 1
Pdx1	pancreatic and duodenal homeobox 1
PH	pleckstrin homology
PI3K	phosphoinositide 3-kinase
PIK3CA	phosphatidylinositol-4,5-bisphosphate 3-kinase, catalytic subunit alpha gene
PIP2	phosphatidylinositol-4,5-bisphosphate
PIP3	phosphatidylinositol-3,4,5-trisphosphate
PKC	protein kinase C
PPARγ	peroxisome proliferator-activated receptor γ
PTEN	phosphatase and tensin homolog
Ptf1a	pancreas specific transcription factor 1a
R	arginine
R26	Rosa26
Rac1	RAS-related C3 botulinum substrate 1
RAF	raf kinase, effector of Ras
RAS	rat sarcoma viral oncogene
Rb	retinoblastoma
RNA	ribonucleic acid
rpm	rounds per minute
RT	room temperature
RTK	receptor tyrosine kinases
S	serine
SA	splice acceptor
SCID	severe combined immunodeficiency
s.d.	standard deviation
sec	second
SKP2	S-phase kinase-associated protein 2
Smad4	mothers against decapentaplegic homolog 4
SREBP	sterol regulatory element-binding protein
SV40	*Simian virus 40*
TAE	Tris acetate EDTA
tdTo	tandem dimer tomato
Tgfbr2	TGFβ receptor 2
TGFβ	transforming growth factor β
TSB	tryptic soy broth
TSC2	tuberous sclerosis 2
U	unit
US	United States (of America)
UV	ultraviolet
V	valine
V	volt

W	watt
Wnt	wingless-type MMTV integration site
WT	wild type

1 Introduction

1.1 Liver and biliary tract cancer

Liver and bilary tract are closely interconnected by their anatomical location as well as their function. Hepatocytes, as the main epithelial cell type of the liver, constitute the liver parenchyme. Their function is production and secretion of bile on the one hand, and uptake, processing and secretion of components from the portal venous blood on the other hand (Müsch, 2014). The biliary tract is a complex branched network of ducts, which transport the bile into the intestinal lumen. It can be divided into the intrahepatic bile ducts, the extrahepatic bile ducts and the gallbladder. Intrahepatic bile ducts comprise small ducts and large ducts, which are the first to third branches of either hepatic duct. The extrahepatic bile ducts include left and right hepatic ducts, the commom hepatic duct and the common bile duct (CBD), which empties into the duodenum in the ampullary region. The gallbladder serves for storage and concentration of the bile (Boyer, 2013; Serra, 2014).

Adenocarcinomas with biliary differentiation are known as cholangiocellular carcinomas (CCC) while carcinomas that develop from hepatocytes are called hepatocellular carcinomas (HCC). Liver cancers in general are the second most common cause of cancer related deaths with worldwide approximately 746,000 cases in 2012. At the same time, there was an estimated number of 782,000 new liver cancer cases worldwide demonstrating the dismal prognosis of this disease (Ferlay et al., 2013).

1.1.1 Hepatocellular carcinoma (HCC)

HCC is the major type of primary liver cancer and accounts for more than 90% (Weledji et al., 2014). As 70-90% of HCC cases arise in the context of chronic liver disease and cirrhosis, the main risk factors are conditions of chronic liver infection or metabolic complications resulting in liver cirrhosis. Chronic infection with hepatitis B virus (HBV) or hepatitis C virus (HCV) account for 50% and 25% of HCC cases respectively and therefore constitute the main risk factor. Due to the presence of endemic HBV infections, approximately 85% of the HCC burden are found in developing countries with highest incidence rates in South East Asia and Sub-Saharan Africa (Sanyal et al., 2010; El-Serag, 2011). Nevertheless, HCC incidence has also tripled during the last two decades in the US up to an incidence of 6 in 100,000 and about 20,000 new cases per year. In Western countries, up to 40% of HCC patients are not infected by hepatitis viruses but show signs of the metabolic syndrome such as obesity, type 2 diabetes, Nonalcoholic Fatty Liver Disease (NAFLD) and Nonalcoholic Steatohepatitis (NASH). These conditions are on the rise and

supposed to contribute more and more to HCC development during the upcoming decades (El-Serag, 2011; El-Serag and Kanwal, 2014). Further established risk factors for HCC development are heavy alcohol intake, consumption of aflatoxin B contaminated food, primary biliary cirrhosis, and genetic metabolic diseases such as hereditary hemochromatosis (Whittaker et al., 2010; Sanyal et al., 2010). HCCs can present solitary or multifocal with nodular or diffuse growth and spread locally or form distant metastasis in bone, lung, brain and adrenal glands (Weledji et al., 2014). HCC is diagnosed rarely before an age of 40 years with a peak at around 70 years. Because of an asymptomatic course of the disease in the beginning and unspecific symptoms, such as weight loss and abdominal pain, in locally advanced tumors, HCC diagnosis occurs frequently in advanced stages implicating that more than 80% of the cases are unresectable. Furthermore, orthotopic liver transplantation is more efficient in avoiding tumor recurrence as the underlying chronic liver disease is cleared as well, but very strong criteria are applied for the allocation of liver transplantations. Local radiofrequency ablation is the best treatment option for early-stage HCC patients that are not eligible for surgery or liver transplantation, resulting in excellent short-term outcomes but 5-year recurrence rates of 70%. Patients with intermediate-stage HCC benefit from transarterial chemoembolization while the primary treatment for patients with advanced-stage tumors is oral chemotherapy with the multikinase inhibitor sorafinib. Because of late diagnosis and lack of effective treatments, the 5-year survival remains below 12% (El-Serag, 2011; Weledji et al., 2014).

Two predominant mechanisms for HCC pathogenesis have been suggested (Whittaker et al., 2010). On the one hand, HCC formation seems to be promoted by liver tissue damage and subsequent cirrhosis due to telomere dysfunction as well as secretion of cytokines, growth factors and reactive oxygen species by activated stellate cells (Sanyal et al., 2010). On the other hand, mutations in one or more oncogenes or tumor suppressor genes contribute to HCC initiation and progression. A large proportion of HCCs show chromosomal instability resulting in an accumulation of deleted or amplified genomic loci (Boyault et al., 2007; Laurent-Puig and Zucman-Rossi, 2006). This chromosomal instability can be provoked by integration of the HBV DNA into the host genome and by disruption of DNA repair mechanisms due to p53 inactivation (Hino et al., 1991; Livezey and Simon, 1997; El-Serag and Rudolph, 2007; Artandi et al., 2000). Indeed, p53 is the top altered protein in HCC as it is inactivated by the HBV antigen hepatitis B virus X protein, frequently deleted by the loss of the chromosomal arm 17p, or mutated with the highest mutation incidence in HCC patients from populations exposed to aflatoxin B1, where the R249S hotspot mutation occurs in up to 50% (Wang et al., 1994; Boige et al., 1997; Bressac et al., 1991; Hsu et al., 1991). Gene expression profiling and whole-genome sequencing studies on large HCC cohorts revealed a high degree of heterogeneity within this tumor entity (Boyault et al., 2007; Alexandrov et al.,

2013). Therefore, different studies report highly differing frequencies of somatic mutations depending on their study population and the distribution of etiologies. For example, one study from Korea reported *PIK3CA* mutations in 36% of the patients evaluated, while the frequency was below 2% in studies from France and Japan (Lee et al., 2005; Boyault et al., 2007; Tanaka et al., 2006). Nevertheless, impaired PTEN and PI3K-AKT-mTOR pathway activation seem to occur in up to 45% of HCC cases suggesting a highly important role of the PI3K-AKT-mTOR pathway in HCC formation (Hu et al., 2003; Sahin et al., 2004; Boyault et al., 2007). Further pathways recurrently described to be altered in HCCs include the TGFβ pathway, Wnt/β-catenin signaling and loss of the G1/S cell cycle checkpoint (Laurent-Puig and Zucman-Rossi, 2006; El-Serag and Rudolph, 2007; Whittaker et al., 2010; Shibata and Aburatani, 2014). Recently, disruption of chromatin remodeling genes such as *ARID2* and *MLL3*, and activation of the telomerase reverse transcriptase have been reported as well (Li et al., 2011; Fujimoto et al., 2012; Llovet et al., 2006; Nault et al., 2013).

1.1.2 Cholangiocellular carcinoma (CCC)

In contrast to HCC, CCC is a relatively rare disease accounting for only 3% of gastrointestinal cancers worldwide and most patients are older than 65 years at presentation (Shaib and El-Serag, 2004). The incidence varies between different parts of the world, mainly due to a variable occurrence of the risk factors associated with CCCs. About 10% of CCC cases are preceded by chronic inflammation or cholestasis. Those inflammatory conditions can be caused by the established risk factors, namely primary sclerosing cholangitis, liver fluke infection, choledochal cysts, chronic gallstones, exposure to carcinogens and hepatitis virus infections (Lazaridis and Gores, 2005; Shaib and El-Serag, 2004).

CCCs are most frequently well- to moderately-differentiated tubular adenocarcinomas supported by a dense stroma (Lazaridis and Gores, 2005). They can form in any part of the biliary tract and are divided into intrahepatic and extrahepatic CCCs with a clear prevalence for extrahepatic location constituting about two thirds of all cases. Extrahepatic CCCs have historically been further subdivided into proximal, middle and distal subgroups, but a binary classification makes more sense from the clinical point of few. Therefore, they are classified as perihilar involving the bifurcation of the left and right hepatic ducts, which indicates hilar resection or partial hepatectomy, or distal, which is treated by pancreatoduodenectomy. Hepatectomy is performed in patients with intrahepatic CCC (Nakeeb et al., 1996; Lazaridis and Gores, 2005). Because of unspecific symptoms, such as jaundice, malaise, weight loss and abdominal pain, resulting in late diagnosis and high age of the patients, more than half of the CCC cases are considered as unresectable. Common palliative treatments for patients with unresectable tumors include biliary stenting, photodynamic therapy, radiotherapy and chemotherapy. The current standard of care in patients with advanced, unresectable biliary

tract cancer is chemotherapy with gemcitabine in combination with cisplatin or oxaliplatin, but the benefit from the therapy remains modest. Furthermore, a few cases have been reported where well-chosen patients considerably benefitted from an orthotopic liver transplantation. (Lazaridis and Gores, 2005; Noel and Hezel, 2013; Valle et al., 2010). Besides treatment options, intrahepatic and extrahepatic CCCs differ also concerning incidence and outcome. Intrahepatic CCCs account for 10-20% of all primary liver cancers and show an incidence of 0.6 per 100,000 in the US with a 5-year survival of less than 5%. The highest incidence has been reported for men in Northeast Thailand with 96 per 100,000. Incidence as well as mortality seem to be rising worldwide for intrahepatic CCCs while the incidence for extrahepatic CCCs is stable or decreasing. The incidence for extrahepatic CCC in the US is 0.97 in 100,000 with a 5-year survival of 15-20% (Shaib and El-Serag, 2004; Chung et al., 2009; Rizvi and Gores, 2013; Singal et al., 2011)

As for many other tumor types, e.g. pancreatic ductal adenocarcinoma (Hruban et al., 2000) or colorectal cancer (Fearon and Vogelstein, 1990), it has been proposed that CCCs develop in a stepwise progression from non-malignant precursor lesions to invasive carcinoma. Biliary precursor lesions can be divided in flat dysplastic lesions and mass-forming dysplastic lesions (Serra, 2014). The flat lesions are referred to as biliary intraepithelial neoplasia (BilIN) and are the most common type of precursor lesions. They can be classified as BilIN-1, BilIN-2 and BilIN-3 depending on the grade of cellular alterations assessed by histopathology. This terminology is used for flat dysplastic lesions in all components of the biliary tract. BilIN-1 is characterized by elongated nuclei that are still basally located and uniform in size and shape, while a BilIN-2 epithelium shows a loss of cellular polarity, dysplastic nuclear changes and irregularities in nuclear size and shape. The BilIN-3 stage describes the carcinoma *in situ* with micropapillary appearance, severely distorted cellular polarity, nuclear atypia, and "budding off" of clusters of cells into the bile duct lumen (Zen et al., 2007). The second frequently found precursor lesion is intraductal papillary neoplasm of the bile duct (IPN-B), which is a mass-forming papillary outgrowth within the bile duct lumen supported by a fibrovascular core. Four different epithelial subtypes exist in IPN-B, namely pancreatobiliary, intestinal, oncocytic and gastric type. IPN-B occurs more frequently in extrahepatic bile ducts than in intrahepatic bile ducts and shows a prevalence in male patients (Rocha et al., 2012). In addition to those two most common precursor lesions, there are several rarely occurring mass-forming lesions such as biliary mucinous cystic neoplasms and intraductal tubular neoplasms, which both are mainly found in intrahepatic bile ducts with a higher prevalence in females compared to males (Serra, 2014). Concerning precursor lesions of the gallbladder and the ampullary region, intra-cholecystic papillary-tubular neoplasms and intra-ampullary papillary-tubular neoplasm have been described respectively (Serra, 2014).

For a better understanding of the CCC development, it is crucial to characterize the molecular mechanisms causing neoplastic changes in the biliary tract epithelium as well as molecular alterations involved in the progression to invasive carcinomas. Global gene expression profiles of biliary cancer tissue and cell lines compared to normal epithelium revealed 282 differentially up-regulated genes including proliferation and cell cycle antigens, transcription factors, growth factors and growth factor receptors, enzymes modulating sensitivity to chemotherapy, TGFβ pathway components, genes involved in steroid metabolism and downstream effectors of the PI3K-AKT-mTOR pathway (Hansel et al., 2003). Several studies demonstrated an overactivation of the PI3K-AKT-mTOR pathway in more than 50% of CCC cases evidenced by phosphorylation of AKT, mTOR, 4E-BP1 or eIF4-E, while mutations in the *PIK3CA* gene itself were rarely reported (Chung et al., 2009; Riener et al., 2008; Simbolo et al., 2014; Deshpande et al., 2011; Voss et al., 2013; Borger et al., 2012). Further frequently observed alterations resulting in PI3K-AKT-mTOR pathway activation comprise mutations in *PTEN* and downregulation of the PTEN protein as well as gene amplification and overexpression of the receptor tyrosine kinases (RTKs) epidermal growth factor receptor (EGFR) and erbB2 (Chung et al., 2009; Simbolo et al., 2014; Borger et al., 2012; Suzuki et al., 1993; Nakazawa et al., 2005). The most investigated pathway in CCC is the RAS-RAF-MEK-ERK signaling pathway, which is mainly induced due to activating mutations in *KRAS*. *KRAS* mutations occur more frequently in extrahepatic CCCs (10-47%) than in intrahepatic CCCs (9-16%) (Suto et al., 2000; Deshpande et al., 2011; Voss et al., 2013; Simbolo et al., 2014) and the mutated proportion of *KRAS* seems to be higher in BilINs or IPN-Bs than in advanced carcinomas (Hsu et al., 2013; Suto et al., 2000; Schlitter et al., 2014). In addition, *NRAS* and *BRAF* are occasionally mutated in intrahepatic CCCs while most studies did not observe any mutations in these genes in extrahepatic CCCs (Xu et al., 2011; Voss et al., 2013; Borger et al., 2012; Simbolo et al., 2014; Deshpande et al., 2011). Loss of function of common tumor suppressors, such as p53, p16 or p27, also contributes to biliary carcinogenesis. p53 impairment as seen by mutations, loss of heterozygosity (LOH) or nuclear overexpression occurs in more than 30% of CCCs with a higher prevalence in extrahepatic CCCs compared to intrahepatic CCCs (Hsu et al., 2013; Suto et al., 2000; Jarnagin et al., 2006; Borger et al., 2012; Simbolo et al., 2014). Furthermore, there is only a slight p53 overexpression in BilINs but already pronounced p53 overexpression in IPN-Bs (Hsu et al., 2013; Nakanishi et al., 2008; Schlitter et al., 2014). p16, a tumor suppressor encoded by the *CDKN2A* gene, is overexpressed in reactive biliary epithelium and gets lost in more than 50% of CCCs due to promoter hypermethylation, LOH or homozygous deletion (Ku et al., 2002; Aishima et al., 2014; Tannapfel et al., 2000; Ueki et al., 2004). The cell cycle regulator and tumor suppressor p27 shows reduced or lost expression mainly in extrahepatic CCCs (Jarnagin et al., 2006; Hui et al., 1999). Recently, a high mutation frequency in *isocitrate dehydrogenase 1* and *2* in intrahepatic CCCs has been

observed but no such mutations in extrahepatic CCCs or gallbladder cancer (Kipp et al., 2012; Borger et al., 2012). Furthermore, aberrant expression of β-catenin and APC as well as Smad4 have been frequently described for CCCs of different localization (Abraham et al., 2003; Nakanishi et al., 2008; Ong et al., 2012; Schlitter et al., 2014; Borger et al., 2012; Suto et al., 2000).

1.1.3 Animal models for the study of liver and biliary tract cancer

Several *in vivo* models of HCC and CCC have been generated in order to gain more insight into relevant genetic factors, carcinogenic processes, treatment possibilities or tumor-stroma interactions.

A fast model for drug screens or simple proof-of-principle experiments is ectopic transplantation of human cancer cell lines or primary tumor material into the flank of immune deficient mice (e.g. Huynh et al. 2006). In contrast, orthotopic implantation of mouse hepatoma cells into fibrotic mouse livers better reflects HCC development and enables study of metastatic processes (Kornek et al., 2008). Besides xenografts, administration of carcinogenic chemicals such as N-nitrosodiethylamine (Gray et al., 1991; Hacker et al., 1991), peroxisome proliferators (Rao and Reddy, 1996), aflatoxin B1 (McGlynn et al., 2003), or carbon tetrachloride (Weisburger, 1977; Confer and Stenger, 1966) to mice or rats is still frequently used as HCC model because these models reproduce the human disease progression from injury through fibrosis to malignancy (Heindryckx et al., 2009). Many of the above mentioned chemicals exert their carcinogenic effect particularly in the liver because of their bioactivation through cytochrome P450 (Heindryckx et al., 2009). Further, a choline deficient diet can be combined with ethionine or N-nitrosodiethylamine supplementation to the drinking water and serves as a model for steatohepatitis induced HCC formation (Knight et al., 2000; de Lima et al., 2008).

As the majority of human HCCs develop in the context of chronic HBV or HCV infections, several groups established mouse models for transgenic expression of viral proteins. Transgenic expression of the HBV surface antigen, pre-S, and X antigens or of the X antigen alone is able to induce HCC formation (Yu et al., 1999; Lakhtakia et al., 2003; Sell et al., 1991). In a similar way, transgenic expression of the whole HCV coding region or of the structural proteins only results in hepatic steatosis and HCC development (Naas et al., 2005; Moriya et al., 1998; Lerat et al., 2002). Another genetically engineered mouse model (GEMM) for steatosis and fibrosis related HCC is the liver specific knock-out of the tumor suppressor *Pten* in *Alb-Cre;Pten*$^{f/f}$ mice (Horie et al., 2004). The liver specific transgenic *Alb-Cre* mouse line consists of a fusion of the *albumin* promoter and enhancer region, a nuclear localization sequence-modified *Cre* recombinase gene and a fragment of the human growth hormone gene (Postic et al., 1999; Postic and Magnuson, 2000). As albumin transcripts can

be detected in the ventral foregut as early as day E8-8.5, *Alb-Cre* activity starts already in the hepatic progenitors called hepatoblasts, which differentiate into both hepatocytes and cholangiocytes based on morphogen gradients (Gualdi et al., 1996; Zong and Stanger, 2012). Fusion of coding sequences for oncogenes such as *Simian virus 40* T antigen and c-myc or the epidermal growth factor to the *albumin* promoter and enhancer region mentioned above has been used for the generation of transgenic mice developing HCC (Sandgren et al., 1989; Borlak et al., 2005). In an analogous manner, the human *α1 antitrypsin* promoter and the mouse *metallothionein 1* promoter have been employed for liver specific overexpression of oncogenes and growth factors resulting in HCC formation (Perraud et al., 1991; Jhappan et al., 1990). Tail vein injection of adenoviral *AdCMV-Cre* in double transgenic *LSL-H-ras*^{V12G}*;Catnb*$^{f/f}$ mice is also a potent HCC model (Harada et al., 2004).

Consistent with the described HCC models, CCC *in vivo* models also comprise xenograft models, chemically induced models and GEMMs. First of all, a variety of human CCC cell lines have been used to establish xenograft models by subcutaneous injection into the flanks of nude mice. Cell lines investigated include the gallbladder carcinoma cell line MZ-ChA-1 (Meng et al., 2006; Fava et al., 2005), the hilar CCC cell line GBC939 (Hou et al., 2011; Zhang et al., 2012; Tang et al., 2007), or cell lines derived from malignant ascites from CCC patients (Olaru et al., 2011; Pawar et al., 2009). These xenograft models could show that injections of tamoxifen or magnetic nanoparticles inhibit tumor growth (Pawar et al., 2009; Tang et al., 2007) while overexpression of certain microRNAs favors xenograft growth (Zhang et al., 2012; Olaru et al., 2011). Besides xenograft models for CCC, an orthotopic transplantation model in rats has been described. Immortalized and *in vitro* transformed rat cholangiocyte cell lines have been injected into the left hepatic duct or into the left hepatic lobe of isogenic rats, resulting in the growth of metastatic tumors in the liver accompanied by bile duct obstruction (Sirica et al., 2008). This model was further exploited to isolate cholangiocytes as well as cancer associated fibroblasts from orthotopic tumors in order to study tumor-stroma interactions in three dimensional co-culture experiments (Campbell et al., 2012). Furthermore, some spontaneous carcinogen induced CCC models have been reported. Treatment of rats with furan results in formation of erbB2 and c-met overexpressing intrahepatic CCCs reflecting typical mutations observed in human CCCs (Radaeva et al., 1999). Intrahepatic CCCs are also induced by feeding of thioacetamide to rats or inoculation with liver fluke followed by dimethylnitrosamine administration in hamsters (Plengsuriyakarn et al., 2012; Fava et al., 2008). In addition, left and median bile duct ligation in mice combined with diethylnitrosamine provokes intrahepatic CCC formation in the context of chronic cholestasis (Yang et al., 2011).

The above mentioned animal models are complemented by GEMMs for CCC. Most of these models use a conditional mutagenic approach where organ specificity is achieved by the *Alb-*

Cre mouse line. *Alb-Cre* dependent mouse models inducing predominantly intrahepatic CCCs and to a minor extend HCCs include *Alb-Cre;Pten$^{f/f}$;Smad4$^{f/f}$*, *Alb-Cre;LSL-Kras^{G12D};p53$^{f/f}$*, *Alb-Cre;R26-NICD*, *Alb-Cre;Pten$^{f/f}$;Tgfbr2$^{f/f}$* and simply *Alb-Cre;Pten$^{f/f}$* in certain background strains (Xu et al., 2006; O'Dell et al., 2012; Zender et al., 2013; Kenerson et al., 2013; Morris et al., 2014). A combination of carcinogen induced and genetically induced CCC model presents carbon tetrachloride treatment in *p53* null mice where intrahepatic CCCs arise in a cirrhotic environment (Farazi et al., 2006). The only genetic model up to now involving gallbladder and extrahepatic bile duct carcinogenesis is a model where wild-type rat erbB2 is expressed depending on the *bovine keratin 5* promoter (Kiguchi et al., 2001). Further possibilities to target the extrahepatic ductal compartment are required to identify genetic modifications involved in extrahepatic CCC formation. In this context, the well established transgenic *Pdx1-Cre* mouse line (Hingorani et al., 2003) plays a promising role. Pdx1 is a homeodomain-containing transcription factor involved in embryonic development of the pancreas and other gastrointestinal organs. It could be detected in the dorsal and ventral wall of the primitive gut as early as day E8.5 and was thought be responsible for pancreatic commitment because pancreatic precursor cells develop in this region around day E9.5 (Ohlsson et al., 1993). Further studies revealed Pdx1 expression in the developing duodenum and adult epithelial cells lining the duodenal villi, in the developing antral stomach and CBD, as well as in the CBD including peribiliary glands and mucin producing cells even after birth (P7) (Guz et al., 1995; Offield et al., 1996; Fukuda et al., 2006). *Pdx1-Cre* is frequently used to target all lineages of the pancreas, for example when crossed with the *LSL-Kras^{G12D}* mouse line (further on called *Pdx1-Cre;Kras^{G12D}*) leading to development of pancreatic ductal adenocarcinoma (PDAC) including typical precursor lesions (Hingorani et al., 2003; Jackson et al., 2001). *Pdx1-Cre* activity in organs other than pancreas including skin, stomach and brain has been reported (Mazur et al., 2010; Honig et al., 2010; Park et al., 2014). The group of Prof. Dr. Dieter Saur developed and characterized a *Pdx1* promoter dependent Flp recombinase mouse line (*Pdx1-Flp*), which induces recombination in the pancreas, duodenum and bile duct (Schönhuber et al., 2014). For this reason, *Pdx1-Cre* and *Pdx1-Flp* have been used in this work for targeted mutagenesis in the extrahepatic bile duct.

1.2 Kirsten Rat Sarcoma viral oncogene homolog (KRAS) signaling

Kirsten Rat Sarcoma viral oncogene homolog (KRAS) is the 6th most commonly mutated gene in human cancers with somatic *KRAS* mutations being major drivers especially in non-small cell lung cancer (NSCLC), colorectal cancer, PDAC and biliary tract cancer. KRAS occurs in the two splicing variants KRAS4A and KRAS4B, with KRAS4B being the widely expressed and dominant isoform in humans, and forms the RAS family of GTPases together with HRAS and NRAS, which are less frequently mutated in human cancers (Chetty and

Govender, 2013; Samatar and Poulikakos, 2014). RAS proteins are transducers that couple ligand binding on cell surface receptors to intracellular pathways (Pylayeva-Gupta et al., 2011). Upon stimulation by upstream receptors such as EGFR or platelet-derived growth factor receptor, RAS switches from its inactive GDP-bound state into an active GTP-bound state, which cycles back to the inactive state through GTP hydrolysis. This cycle is regulated by GTPase activating proteins (GAPs) and guanine nucleotide exchange factors, which are influenced by the upstream receptors (Chetty and Govender, 2013; Samatar and Poulikakos, 2014). Active RAS proteins feed into stimulation of several effector proteins including RAF kinases, PI3Ks, RalGDS, p120GAP, MEKK1, RIN1, PLCε, MST1, Rac, Rho, Tiam1 and NF1 (Chetty and Govender, 2013; Eser et al., 2014; Castellano and Downward, 2011). RAF-MEK-ERK and PI3K-AKT-mTOR pathways are the two most extensively studied RAS effector pathways, the latter of which will be described in detail in the next chapter. RAF proteins (encoded by *ARAF*, *BRAF*, *CRAF*) are recruited to the inner leaflet of the plasma membrane through binding to RAS-GTP where they dimerize and get activated. Active RAF activates MEK, a threonine and tyrosine kinase which in turn phosphorylates and thereby activates ERK. Upon activation, ERK can phosphorylate other kinases and transcription factors which results in cell cycle progression, differentiation, protein translation and evasion from cell death (Samatar and Poulikakos, 2014). About one third of human cancers express constitutively active RAS isoforms and additionally, BRAF activation occurs in approximately 8% of human cancers. RAS activating mutations cluster in the amino acid residues 12, 13 and 61 and stabilize the GTP-bound state thus constitutively activating downstream signaling (Samatar and Poulikakos, 2014). GEMMs expressing typical KRAS mutants have been generated for the study of carcinogenesis in various tissues as reviewed by Janssen and colleagues (Janssen et al., 2005). An *LSL-Kras*^{G12D} mouse line has been used in this work for conditional expression of the *Kras*^{G12D} mutation, which disturbs correct orientation of the catalytic glutamine residue and prevents van der Waals bonds between RAS and GAP (Jackson et al., 2001; Pylayeva-Gupta et al., 2011).

1.3 The phosphoinositide 3-kinase (PI3K) signaling pathway

The PI3K-AKT-mTOR signaling pathway is a major RAS effector pathway and one of the most frequently overactivated pathways in human cancers. Overactivation occurs mainly through loss of PTEN, but also by upregulation of RTKs and alterations in PI3K isoforms, and is a frequent event in liver and biliary tract cancers, as described above (Thorpe et al., 2015). PI3Ks comprise a family of kinases that phosphorylate the 3'-hydroxy group of phosphatidylinositides on the inner side of the plasma membrane thereby generating second messenger molecules, most importantly phosphatidylinositol-3,4,5-trisphosphate (PIP3), which can recruit proteins containing pleckstrin homology (PH) domains to the plasma membrane (Castellano and Downward, 2011). PI3Ks are subdivided into three classes with

class IA being the most relevant group concerning tumorigenesis. Class IA PI3Ks are heterodimers of the catalytic subunits p110α, p110β, or p110δ combined with any of the p85-type regulatory subunits, while class IB includes heterodimers of p110γ associated with either p101 or p87. All class I PI3Ks contain RAS binding domains and only p110α and p110β are ubiquitously expressed whereas p110γ and p110δ are mainly found in leukocytes. Class II contains three monomeric lipase kinases named PI3K-C2α, PI3K-C2β and PI3K-C2γ, and class III contains only the heterodimer of catalytic VPS34 and myristoylated VPS15 (Thorpe et al., 2015). Class IA PI3Ks can be activated by direct binding of p85 to activated RTKs, through adaptor complexes containing GRB2, which link PI3Ks and RTKs via GAB or activated RAS, or less frequently through activation of G protein coupled receptors (Castellano and Downward, 2011). Once activated, all class IA isoforms generate PIP3, which leads to plasma membrane recruitment of AKT and PDK1 via their PH domains and phosphorylation of AKT at threonine 308 by PDK1. Additional phosphorylation of AKT at serine 473 by mTORC2 is necessary for full AKT activation (Vanhaesebroeck et al., 2012). More than 100 downstream targets of AKT have been identified up to now, including GSK3β, BAD, p21, p27, forkhead box O transcription factors (FOXOs), and TSC2 whose phosphorylation contributes to mTORC1 activation (Vanhaesebroeck et al., 2012). Furthermore, there are AKT independent PI3K effectors, such as p70S6K, atypical PKC isoforms or Rac1 (Castellano and Downward, 2011; Taniguchi et al., 2006). Altogether, PI3K pathway activation results in cell proliferation, cell growth, cell survival, actin rearrangements, motility, glycogen metabolism, glucose uptake, and protein synthesis (Thorpe et al., 2015; Vanhaesebroeck et al., 2012; Castellano and Downward, 2011). PI3K pathway activation is balanced under physiological conditions by the lipid phosphatase PTEN which removes the 3'-phosphate from PIP3. This control mechanism is frequently lost in cancer or overridden by constitutive production of PIP3 due to mutations in the p110α encoding gene *PIK3CA*, which mainly cluster in the helical domain (E543K, E545K) or in the kinase domain (H1047R) (Thorpe et al., 2015). It is important to note that p110α is not only the most frequently mutated PI3K isoform in cancer but also the major catalytic subunit involved in hepatic insulin signaling (Sopasakis et al., 2010). Lots of GEMMs have been used in the past to study the roles of PI3K isoforms and mutations in physiology and cancer (Thorpe et al., 2015; Carnero and Paramio, 2014). The *LSL-PIK3CA*^{H1047R} mouse line generated by the group of Prof. Dr. Dieter Saur has been used in this work, where the *PIK3CA* hotspot mutation H1047R, constitutively activating p110α independent of RAS-GTP binding, can be conditionally expressed in the organs of interest (Eser et al., 2013; Castellano and Downward, 2011).

1.4 Aims of this work

As depicted above, the PI3K-AKT-mTOR signaling pathway is frequently deregulated in liver and biliary tract cancers but the exact mechanisms driving carcinogenesis are still unknown. Mice overexpressing mutant p110α^{H1047R} in the liver (*Alb-Cre;PIK3CA^{H1047R}*) or in the extrahepatic bile duct and other organs of the gastrointestinal tract (*Pdx1-Cre;PIK3CA^{H1047R}*) have been generated and were analyzed for survival and tumor formation. The *Pdx1-Cre;PIK3CA^{H1047R}* model was compared to the *Pdx1-Cre;Kras^{G12D}* model and combined with deletions of *p53*, *Cdkn2a* or *p27* in order to figure out which molecular pathways are relevant to carcinogenesis in the extrahepatic bile duct. To study carcinogenesis in more sophisticated GEMMs in the future, a new *FSF-PIK3CA^{H1047R}* mouse line has been generated, where the expression of mutant p110α can be activated by a Flp recombinase and ablated later by a tamoxifen-inducible Dre recombinase.

2 Materials

2.1 Technical equipment

Table 2-1: Technical equipment.

Device	Source
Analytical balance A 120 S	Sartorius AG, Göttingen
Analytical balance BP 610	Sartorius AG, Göttingen
Autoclave 2540 EL	Tuttnauer Europe B.V., Breda, The Netherlands
AxioCam HRc	Carl Zeiss AG, Oberkochen
AxioCam MRc	Carl Zeiss AG, Oberkochen
Centrifuge AvantiR J25	Beckman Coulter GmbH, Krefeld
Centrifuge Rotina 46R	Andreas Hettich GmbH & Co. KG, Tuttlingen
CO_2 incubator MCO-5AC 17AI	Sanyo Sales & Marketing Europe GmbH, Munich
Compact L/XL electrophoresis chambers and gel casting apparatus containing gel trays and combs	Biometra GmbH, Göttingen
Confocal microscope Leica TCS SP5 DMI 6000 CS	Leica Microsystems GmbH, Wetzlar
Cryostat Microm HM560	Thermo Fisher Scientific, Inc., Waltham, MA, USA
Dewar carrying flask, type B	KGW-Isotherm, Karlsruhe
Electrophoresis power supply Power Pac 200	Bio-Rad Laboratories GmbH, Munich
Flu-O-Blu	Biozym Scientific GmbH, Hessisch Oldenburg
Gel Doc™ XR+ system	Bio-Rad Laboratories GmbH, Munich
Gene Pulser® II	Bio-Rad Laboratories GmbH, Munich
Glass ware, Schott Duran®	Schott AG, Mainz
Heated paraffin embedding module EG1150 H	Leica Microsystems GmbH, Wetzlar
HERAsafe® biological safety cabinet	Thermo Fisher Scientific, Inc., Waltham, MA, USA
Horizontal gel electrophoresis system	Biozym Scientific GmbH, Hessisch Oldenburg
Incubator	Heraeus Holding GmbH, Hanau
Incubator shaker Thermoshake	C. Gerhardt GmbH & Co. KG, Königswinter
Laminar flow HERAsafe	Heraeus Holding GmbH, Hanau
Magnetic stirrer, Ikamag® RCT	IKA® Werke GmbH & Co. KG, Staufen
Microcentrifuge 5424 R	Eppendorf AG, Hamburg
Microscope Axio Imager A1	Carl Zeiss AG, Oberkochen

Device	Source
Microscope Axiovert 25	Carl Zeiss AG, Oberkochen
Microscope DM LB	Leica Microsystems GmbH, Wetzlar
Microtome Microm HM355S	Thermo Fisher Scientific, Inc., Waltham, MA, USA
Microwave	Siemens
Mini centrifuge MCF-2360	LMS Consult GmbH & Co. KG, Brigachtal
Multipette® stream	Eppendorf AG, Hamburg
NALGENE® Cryo 1°C Freezing Container	Thermo Fisher Scientific, Inc., Waltham, MA, USA
Neubauer hemocytometer, improved	LO-Laboroptik GmbH, Friedrichsdorf
Paraffin tissue floating bath Microm SB80	Thermo Fisher Scientific, Inc., Waltham, MA, USA
pH meter 521	WTW Wissenschaftlich-Technische Werkstätten GmbH, Weilheim
Photometer gene quant pro RNA/DNA calculator	Pharmacia Biotech Inc., Piscataway, NJ, USA
Pipettes Reference®, Research®	Eppendorf AG, Hamburg
Pipetus®	Hirschmann Laborgeräte GmbH & Co. KG, Eberstadt
PTC-200 DNA Engine	MJ Research, GMI Inc., Minnesota, USA
Spectrophotometer NanoDrop® 1000	Peqlab Biotechnologie GmbH, Erlangen
Stereomicroscope Stemi SV 11	Carl Zeiss AG, Oberkochen
Surgical instruments	Thermo Fisher Scientific, Inc., Waltham, MA, USA
Thermocycler T1	Biometra GmbH, Göttingen
Thermocycler TGradient	Biometra GmbH, Göttingen
Thermocycler TPersonal	Biometra GmbH, Göttingen
Tissue processor ASP300	Leica Microsystems GmbH, Wetzlar
Vortex Genius 3	IKA® Werke GmbH & Co. KG, Staufen
Water bath 1003	GFL Gesellschaft für Labortechnik mbH, Burgwedel

2.2 Disposables

Table 2-2: Disposables.

Disposable	Source
Cell culture plastics	Becton Dickinson GmbH, Franklin Lakes, NJ, USA; Greiner Bio-One GmbH, Frickenhausen
Combitips BioPur®	Eppendorf AG, Hamburg
Conical tubes 15 ml, 50 ml	Greiner Bio-One GmbH, Frickenhausen

Disposable	Source
Cover slips	Gerhard Menzel, Glasbearbeitungswerk GmbH & Co. KG, Braunschweig
CryoPure tubes	Sarstedt AG & Co., Nümbrecht
Cuvette	Greiner Bio-One GmbH, Frickenhausen
Disposable scalpels	Feather Safety Razor Co., Ltd., Osaka, Japan
Electroporation cuvettes (0.2 cm gap)	Bio-Rad Laboratories GmbH, Munich
Filter tips for pipettes	nerbe plus GmbH, Winsen/Luhe
Filtropur S 0.2	Sarstedt AG & Co., Nümbrecht
Filtropur S 0.45	Sarstedt AG & Co., Nümbrecht
Glass slides Superfrost® Plus	Gerhard Menzel, Glasbearbeitungswerk GmbH & Co. KG, Braunschweig
Inoculation loop, sterile	Greiner Bio-One GmbH, Frickenhausen
Inoculation spreader, sterile	Sarstedt AG & Co., Nümbrecht
Microtome blades S35 and C35	Feather Safety Razor Co., Ltd., Osaka, Japan
Microvette® 500 Z-Gel tube	Sarstedt AG & Co., Nümbrecht
Parafilm M	Brand GmbH & Co. KG, Wertheim
Pasteur pipettes	Hirschmann Laborgeräte GmbH & Co. KG, Eberstadt
PCR reaction tubes	Brand GmbH & Co. KG, Wertheim; Eppendorf AG, Hamburg
Petri dishes	Sarstedt AG & Co., Nümbrecht
Pipette tips	Sarstedt AG & Co., Nümbrecht
Reaction tubes, 0.5 ml, 1.5 ml and 2 ml	Eppendorf AG, Hamburg
Safe-lock reaction tubes BioPur®	Eppendorf AG, Hamburg
Serological pipettes	Sarstedt AG & Co., Nümbrecht
Single use needles Sterican® 27 gauge	B. Braun Melsungen AG, Melsungen
Single use syringes Omnifix®	B. Braun Melsungen AG, Melsungen
Tissue embedding cassette system	Medite GmbH, Burgdorf

2.3 Reagents and enzymes

Table 2-3: Reagents and enzymes.

Reagent/enzyme	Source
1 kb extension ladder	Invitrogen GmbH, Karlsruhe
2-log DNA ladder (0.1–10.0 kb)	New England Biolabs GmbH, Frankfurt am Main

Reagent/enzyme	Source
2-Mercaptoethanol	Sigma-Aldrich Chemie GmbH, Taufkirchen
2-Propanol	Carl Roth GmbH & Co. KG, Karlsruhe
Agarose	Sigma-Aldrich Chemie GmbH, Taufkirchen
Ammonium sulfate ($(NH_4)_2SO_4$)	Sigma-Aldrich Chemie GmbH, Taufkirchen
Ampicillin sodium salt	Carl Roth GmbH & Co. KG, Karlsruhe
Bovine serum albumin (BSA)	Serva Electrophoresis GmbH, Heidelberg
Calcium chloride ($CaCl_2$)	Sigma-Aldrich Chemie GmbH, Taufkirchen
Cresol red	AppliChem GmbH, Darmstadt
Dimethyl sulfoxide (DMSO)	Carl Roth GmbH & Co. KG, Karlsruhe
dNTP Mix, 10 µM each	Sigma-Aldrich Chemie GmbH, Taufkirchen
Ethanol (100%)	Merck KGaA, Darmstadt
Ethidium bromide	Sigma-Aldrich Chemie GmbH, Taufkirchen
Ethylenediaminetetraacetic acid (EDTA)	Invitrogen GmbH, Karlsruhe
Forene® isoflurane	Abbott GmbH & Co. KG, Ludwigshafen
Gateway® LR Clonase™	Invitrogen GmbH, Karlsruhe
GelStar™ Nucleic Acid Stain	Lonza, Basel, Switzerland
Gene Ruler™ 100bp DNA ladder	Fermentas GmbH, St. Leon-Rot
Glycerol	Sigma-Aldrich Chemie GmbH, Taufkirchen
High Fidelity (HF™) restriction endonucleases	New England Biolabs GmbH, Frankfurt am Main
HotStarTaq DNA Polymerase	Qiagen GmbH, Hilden
Hydrochloric acid (HCl)	Merck KGaA, Darmstadt
Kanamycin sulphate	Carl Roth GmbH & Co. KG, Karlsruhe
LB medium (Luria/Miller)	Carl Roth GmbH & Co. KG, Karlsruhe
LB-Agar (Luria/Miller)	Carl Roth GmbH & Co. KG, Karlsruhe
LB-Broth (Luria/Miller)	Carl Roth GmbH & Co. KG, Karlsruhe
Magnesium chloride ($MgCl_2$)	Carl Roth GmbH & Co. KG, Karlsruhe
Magnesium sulfate ($MgSO_4$)	Merck KGaA, Darmstadt
Methanol	Merck KGaA, Darmstadt
N,N-Dimethylformamide	Sigma-Aldrich Chemie GmbH, Taufkirchen
Orange G	Carl Roth GmbH & Co. KG, Karlsruhe
Phosphate buffered saline (PBS) Dulbecco, powder	Merck KGaA, Darmstadt
Polyethylene glycol 4000	Merck KGaA, Darmstadt

Reagent/enzyme	Source
Potassium chloride (KCl)	Sigma-Aldrich Chemie GmbH, Taufkirchen
Proteinase K, recombinant, PCR grade	Roche Deutschland Holding GmbH, Grenzach-Wyhlen
Quick T4 Ligase	New England Biolabs GmbH, Frankfurt am Main
rAPid alkaline phosphatase	Roche Deutschland Holding GmbH, Grenzach-Wyhlen
REDTaq® ReadyMix™ PCR reaction mix	Sigma-Aldrich Chemie GmbH, Taufkirchen
Restriction endonucleases	New England Biolabs GmbH, Frankfurt am Main
Roti® Histofix 4%	Carl Roth GmbH & Co. KG, Karlsruhe
Saponin	AppliChem GmbH, Darmstadt
Sodium acetate buffer solution	Sigma-Aldrich Chemie GmbH, Taufkirchen
Sodium chloride (NaCl)	Merck KGaA, Darmstadt
Sodium dodecyl sulfate (SDS)	Serva Electrophoresis GmbH, Heidelberg
Sucrose	Merck KGaA, Darmstadt
T4 DNA Ligase	Invitrogen GmbH, Karlsruhe
Taq DNA Polymerase, buffer S	Peqlab Biotechnologie GmbH, Erlangen
Tissue-Tek® O.C.T.™ compound	Sakura Finetek Europe B.V, Alphen aan den Rijn, The Netherlands
Tris hydrochloride	J.T.Baker® Chemicals, Phillipsburg, NJ, USA
Tris Pufferan®	Carl Roth GmbH & Co. KG, Karlsruhe
Triton® X-100	Merck KGaA, Darmstadt
Tween® 20	Carl Roth GmbH, Karlsruhe
X-Gal	Peqlab Biotechnologie GmbH, Erlangen

2.4 Kits

Table 2-4: Kits.

Kit	Source
EndoFree® Plasmid Maxi Kit	Qiagen GmbH, Hilden
QIAGEN® Plasmid Midi Kit	Qiagen GmbH, Hilden
QIAprep® Spin Miniprep Kit	Qiagen GmbH, Hilden
QIAquick® Gel Extraction Kit	Qiagen GmbH, Hilden
Quick Blunting™ Kit	New England Biolabs GmbH, Frankfurt am Main

2.5 Plasmids and bacterial strains

All plasmids were amplified in One shot® Stbl3™ chemically competent *E. coli* bacteria (Invitrogen GmbH, Karlsruhe).

Table 2-5: Plasmids.

Plasmid	Abbreviation	Modification
pBlu-SA-rsr-MCS-pA	kad #18	Generated in the laboratory of Prof. Saur, Munich from ayp4; modification of pBluescript SK+ (Stratagene, La Jolla, CA, USA) containing SA-rox-stop-rox
pEntr-frt-gt-neostop-frt-MCS-pA	kaf #11	Generated in the laboratory of Prof. Saur, Munich; modification of pENTR™/D-TOPO® (Invitrogen GmbH, Karlsruhe) containing frt-stop-frt
pEntr-SA-rox-frt-gt-neostop-frt-MCS-pA	kag #13	Generated in the laboratory of Prof. Saur, Munich; modification of pENTR™/D-TOPO®: Ligation of SA-rox-stop-rox from kad #18 into kaf #11
pEntr-SA-rox-frt-gt-neostop-frt-MCS-pA-rox	kal #16	Generated in the laboratory of Prof. Saur, Munich; modification of pENTR™/D-TOPO®: Insertion of the 2nd rox-site into kag #13
pEntr-SA-rox-frt-gt-neostop-frt-PIK3CA-pA-rox	kam #3	Generated in the laboratory of Prof. Saur, Munich; modification of pENTR™/D-TOPO®: Insertion of the *PIK3CA*^{H1047R} ORF into kal #16
pRosa26-Att-CCDB-Att	aqt1	Generated in the laboratory of Prof. Saur, Munich; Gateway® LR Clonase™ *Rosa26* destination vector
pRosa26-FSF-PIK3CA^{H1047R}	kan #4	Targeting vector generated in the laboratory of Prof. Saur, Munich; Gateway® LR Clonase™ shuttling of rox-frt-stop-frt- PIK3CA^{H1047R} from kam #3 into aqt1

2.6 Primers

All oligonucleotides were produced by Eurofins Genomics (Ebersberg).

Table 2-6: Primers for genotyping and recombination PCRs.

PCR	Primer	Sequence (5'-3')
Alb-Cre	Alb-Cre-UP	GTAATGGGGTAGGAACCAATGA
	Cre-neu-LP	CAGGGTGTTATAAGCAATCCC
	Gabra1-UP	AACACACACTGGAGGACTGGCTAGG
	Gabra1-LP	CAATGGTAGGCTCACTCTGGGAGATGATA
PIK3CA	pGL3-pA-pause4645-UP	TGAATAGTTAATTGGAGCGGCCGCAATA
	PI3K-genotyp-RevPr	AAATAGCCGCAGGTCACAAAGTCTCCG

PCR	Primer	Sequence (5'-3')
Rosa26	R26-Tva-GT-UP	AAAGTCGCTCTGAGTTGTTAT
	R26-Tva-GT-SA-mut-LP	GCGAAGAGTTTGTCCTCAACC
	R26-Tva-GT-WT-LP	GGAGCGGGAGAAATGGATATG
Pdx1-Cre	Pdx-Prom-UP2	GCTCATTGGGAGCGGTTTTG
	V-Cre-LP2	ACATCTTCAGGTTCTGCGGG
	PdxKON-LP1	CACGTGGTTTACCCTGGAGC
$R26^{tdTo}$	tdTomato-tdEG-UP	CAAGGGAGAGGAGGTCATCAAAG
	tdTomato-tdEG- LP	GCTTGGTGTCCACGTAGTAGTAGC
$R26^{mT/mG}$	R26-Tva-GT-UP	AAAGTCGCTCTGAGTTGTTAT
	CAG-sc-LP	GTACTTGGCATATGATACACTTGATGTAC
	R26-Tva-GT-WT-LP	GGAGCGGGAGAAATGGATATG
LSL-Kras	Kras-WT-UP1	CACCAGCTTCGGCTTCCTATT
	Kras-URP-LP1	AGCTAATGGCTCTCAAAGGAATGTA
	KrasG12Dmut-UP	CCATGGCTTGAGTAAGTCTGC
$p53^{f}$	p53 berns UP-E	CACAAAAAACAGGTTAAACCCAGC
	p53 berns LP-F	GCACCTTTGATCCCAGCACATA
$Cdkn2a^{f}$	INK4A-UP	CCAAGTGTGCAAACCCAGGCTCC
	INK4A-LP	TTGTTGGCCCAGGATGCCGACATC
p27 knock-out	mgk3	TGGAACCCTGTGCCATCTCTAT
	Neo-1	CCTTCTATGGCCTTCTTGACG
p27 wild type	mgk3	TGGAACCCTGTGCCATCTCTAT
	mck5	GAGCAGACGCCCAAGAAGC
Pdx1-Flp	pdx5ut-scUP	AGAGAGAAAATTGAAACAAGTGCAGGT
	Flpopt-scLP	CGTTGTAAGGGATGATGGTGAACT
	Gabra1-UP	AACACACACTGGAGGACTGGCTAGG
	Gabra1-LP	CAATGGTAGGCTCACTCTGGGAGATGATA
rox	Broad PA5038	CGCTTTCTTGCTGTCCAATTTCTAT
	REVsacxhoroxasc	CGCGCCTAACTTTAAATAATTGGCATTATTTAAAGTTACTCGAGCT
PIK3CA del	Soriano_SA_UP	CAGTAGTCCAGGGTTTCCTTGATG
	pGL3-pA-pause4645-UP	TGAATAGTTAATTGGAGCGGCCGCAATA
	PI3K-genotyp-RevPr	AAATAGCCGCAGGTCACAAAGTCTCCG

PCR	Primer	Sequence (5'-3')
$R26^{mT/mG}$ del	caggs-sc-UP4	GTTCGGCTTCTGGCGTGT
	tdTomato-tdEG-LP	GCTTGGTGTCCACGTAGTAGTAGC
	EGFP-tdEG-LP	CCATGTGATCGCGCTTCTCGT

Table 2-7: Primers and oligonucleotides for cloning and validation of ES cell clones.

PCR	Primer	Sequence (5'-3')
Cloning PCR Screen	M831Blue-RP	ACACAGGAAACAGCTATGACCATGA
	BrPaUP1	CTAGAAGCTCGCTTTCTTGCTGTCCAATTTCT
Cloning PCR Screen	M597Blue-UP	GTTGTAAAACGACGGCCAGTGA
	Neo-TM-LP1	GTGCCCAGTCATAGCCGAAT
Cloning PCR Screen	pGL3-pA-pause-4645-UP	TGAATAGTTAATTGGAGCGGCCGCAATA
	pBroad-pA-5268-LP	CCAAGGTTTGAACTAGCTCTTCATTT
Cloning PCR Screen	pEntrscUP1	GTTGTAAAACGACGGCCAGTCTT
	FSFneoNcoLp	GCATCGCCATGGGTCACGACGA
Oligo Annealing	FORsacxhoroxascLI	CGAGTAACTTTAAATAATGCCAATTATTTAAAGTTAGG
	REVsacxhoroxascLI	CGCGCCTAACTTTAAATAATTGGCATTATTTAAAGTTACTCG AGCT
Cloning PCR Screen	pEntr sc LP	GCTGCCAGGAAACAGCTATGAC
	BroadPA- 5219-UP	GGTCAGTGCATTTAAAACATAAAGAAATG
Cloning PCR Screen	pEntr sc LP	GCTGCCAGGAAACAGCTATGAC
	FORsacxhoroxascLI	CGAGTAACTTTAAATAATGCCAATTATTTAAAGTTAGG
Cloning PCR Screen	pGL3-pA-pause4645-UP	TGAATAGTTAATTGGAGCGGCCGCAATA
	PI3K-genotyp-RevPr	AAATAGCCGCAGGTCACAAAGTCTCCG
ES Cell Screen	RosES-UP2	GCTCCTCAGAGAGCCTCGGCTAGGTAG
	RosES-LP1	GGAGCCTGCTTTTTTGTACAAAGTTGTGA
ES PCR1	RosES-UP2	GCTCCTCAGAGAGCCTCGGCTAGGTAG
	RosES-LP1	GGAGCCTGCTTTTTTGTACAAAGTTGTGA
ES PCR2	R26-Tva-GT-UP	AAAGTCGCTCTGAGTTGTTAT
	fsaSFneosc-lp2	ATTGCATCAGCCATGATGGATACTTTCT
ES PCR3	Neo-TM-UP1	TGGATTGCACGCAGGTTCT
	PI3K-genotyp-RevPr	AAATAGCCGCAGGTCACAAAGTCTCCG
ES PCR4	pGL3-pA-pause4645-UP	TGAATAGTTAATTGGAGCGGCCGCAATA
	PI3K-genotyp-RevPr	AAATAGCCGCAGGTCACAAAGTCTCCG

PCR	Primer	Sequence (5'-3')
ES PCR5	pGL3-pA-pause4645-UP	TGAATAGTTAATTGGAGCGGCCGCAATA
	BrPaLP1	TAAAATACAGCATAGCAAAACTTTAACCTCCAAATC
ES PCR6	Broad PA5038	CGCTTTCTTGCTGTCCAATTTCTAT
	R26-lA_LP1	CATTCTCAGTGGCTCAACAACACT

Table 2-8: Primers for testing for mycoplasm contamination.

Primer	Sequence (5'-3')
Forward primer mix	CGCCTGAGTAGTACGTTCGC
	CGCCTGAGTAGTACGTACGC
	TGCCTGGGTAGTACATTCGC
	TGCCTGAGTAGTACATTCGC
	CGCCTGAGTAGTATGCTCGC
	CACCTGAGTAGTATGCTCGC
	CGCCTGGGTAGTACATTCGC
Reverse primer mix	GCGGTGTGTACAAGACCCGA
	GCGGTGTGTACAAAACCCGA
	GCGGTGTGTACAAACCCCGA

2.7 Cell culture

Table 2-9: Cell lines.

Cell line	Source
W4/129S6 embryonic stem (ES) cells	Taconic Farms, Inc., Hudson, NY, USA

Table 2-10: Reagents for cell culture.

Reagent	Source
2-Mercaptoethanol	Sigma-Aldrich Chemie GmbH, Taufkirchen
Dimethyl sulfoxide (DMSO)	Carl Roth GmbH & Co. KG, Karlsruhe
Dulbecco's modified eagle medium (D-MEM) high glucose, w/o L-glutamine	Gibco, Life Technologies GmbH, Darmstadt
Dulbecco's Phosphate Buffered Saline (PBS)	Gibco, Life Technologies GmbH, Darmstadt
ESGRO® Leukemia Inhibitory Factor (LIF)	Merck KGaA, Darmstadt
Fetal bovine serum (FBS), ES cell quality, USA origin	Gibco, Life Technologies GmbH, Darmstadt
Fetal calf serum (FCS)	Biochrom AG, Berlin

Reagent	Source
G418, Geneticin®	Gibco, Life Technologies GmbH, Darmstadt
Gelatin from porcine skin Type A	Sigma-Aldrich Chemie GmbH, Taufkirchen
L-glutamine 200 mM	Gibco, Life Technologies GmbH, Darmstadt
MEM non-essential amino acids	Gibco, Life Technologies GmbH, Darmstadt
Penicillin (10000 units/ml)-streptomycin (10000µg/ml) solution	Gibco, Life Technologies GmbH, Darmstadt
Sodium pyruvate MEM	Gibco, Life Technologies GmbH, Darmstadt
Trypsin, 0.05% with 0.53 mM EDTA•4Na	Gibco, Life Technologies GmbH, Darmstadt

Table 2-11: Media for cell culture.

Medium	Components
MEF medium	D-MEM (high glucose, w/o L-glutamine)
	10% FCS (Biochrom)
	1% L-glutamine
	1% Penicillin-streptomycin
ES cell medium	D-MEM (high glucose, w/o L-glutamine)
	15% FBS (Gibco)
	1% L-glutamine
	1% MEM non-essential amino acids
	1% Sodium pyruvate MEM
	1% Penicillin-streptomycin
	0.1% 0.1 M 2-Mercaptoethanol
	1000 U/ml LIF

2.8 Histology

Table 2-12: Reagents and kits for histological stainings.

Reagent/kit	Source
Aluminium sulphate ($Al_2(SO_4)_3$)	Honeywell Specialty Chemicals Seelze GmbH, Seelze
Antigen unmasking solution, citric acid based	Vector Laboratories, Inc., Burlingame, CA, USA
Avidin/biotin blocking kit	Vector Laboratories, Inc., Burlingame, CA, USA
Certistain® Nuclear fast red	Merck KGaA, Darmstadt
DAB peroxidase substrate kit, 3,3'-diaminobenzidine	Vector Laboratories, Inc., Burlingame, CA, USA
Dako Target Retrieval Solution (pH6)	Dako Deutschland GmbH, Hamburg

Reagent/kit	Source
DCS detection line system AD050POL-K	DCS Diagnostics, Hamburg
Eosin	Waldeck GmbH & Co KG, Münster
Goat serum G9023	Sigma-Aldrich Chemie GmbH, Taufkirchen
Hematoxylin	Merck KGaA, Darmstadt
Hydrogen peroxide 30%	Merck KGaA, Darmstadt
Oil Red O	Sigma-Aldrich Chemie GmbH, Taufkirchen
Permanent AP Red Kit ZUC001-125	Zytomed Systems GmbH, Berlin-Zehlendorf
Pertex mounting medium	Medite GmbH, Burgdorf
Roti® Histofix 4%	Carl Roth GmbH & Co. KG, Karlsruhe
Roti® Histol	Carl Roth GmbH & Co. KG, Karlsruhe
Senescence beta-Galactosidase Staining Kit	Cell Signaling Technology, Inc, Danvers, MA, USA
TOPRO®-3 iodide	Invitrogen GmbH, Karlsruhe
Vectashield® Mounting Medium	Vector Laboratories, Inc., Burlingame, CA, USA
Vectastain® Elite ABC Kit	Vector Laboratories, Inc., Burlingame, CA, USA

Table 2-13: Buffers for histological stainings.

Buffer	Components
Nuclear Fast Red	0.1% Nuclear fast red
	2.5% Aluminium sulphate
Oil Red O stock	0.5% Oil Red O
	In 2-propanol
Oil Red O working solution	60% Oil Red O stock
	In H_2O

2.9 Antibodies

Table 2-14: Antibodies.

Antibody	Source
Anti-rabbit IgG (H+L) (DyLight™ 680 Conjugate), #5366 (1:100)	Cell Signaling Technology, Inc, Danvers, MA, USA
Biotinylated anti-mouse IgG (H+L), BA-9200 (1:500)	Vector Laboratories, Burlingame, CA, USA
Biotinylated anti-rabbit IgG (H+L), BA-1000 (1:500)	Vector Laboratories, Burlingame, CA, USA
Biotinylated anti-rat IgG (H+L), BA-9400 (1:500)	Vector Laboratories, Burlingame, CA, USA
CK19 (Troma-III) (1:300)	Developmental studies hybridoma bank, Iowa City, IA, USA

Antibody	Source
CK19, ab62364 (1:100)	Abcam plc, Cambridge, UK
HepPar1, M7158 (1:50)	Dako Deutschland GmbH, Hamburg
p27, ab62364 (1:500)	Abcam plc, Cambridge, UK
Phospho-GSK3β-S9, #9323 (1:100)	Cell Signaling Technology, Inc, Danvers, MA, USA
Phospho-AKT-S473, #4060 (1:50)	Cell Signaling Technology, Inc, Danvers, MA, USA
Phospho-AKT-T308, #2965 (1:50)	Cell Signaling Technology, Inc, Danvers, MA, USA
Phospho-ERK1/2-T202/Y204, #4370 (1:300)	Cell Signaling Technology, Inc, Danvers, MA, USA

2.10 Buffers and solutions

All buffers were prepared with bidistilled H_2O if not declared otherwise.

Table 2-15: Buffers and solutions.

Buffer/solution	Components
10x Gitschier's buffer	670 mM Tris, pH 8.8
	166 mM $(NH_4)_2SO_4$
	67 mM $MgCl_2$
20x Oligo Annealing Buffer	200 mM Tris-HCl, pH=8.0
	1 M NaCl
	40 mM $MgCl_2$
	10 mM EDTA
50x Tris acetate EDTA (TAE) buffer, pH 8.5	2 M Tris
	50 mM EDTA
	5.71% Acetic acid
5x KCM buffer	500 mM KCl
	150 mM $CaCl_2$
	250 mM $MgCl_2$
DNA lysis buffer (Soriano)	0.5% Triton® X-100
	1% 2-Mercaptoethanol
	1x Gitschier's buffer
	400 µg/ml Proteinase K (add prior to use)

Buffer/solution	Components
ES cell DNA lysis buffer	100 mM Tris, pH 8.5
	5 mM EDTA
	0.8 mM HCl
	0.2% SDS
	200 mM NaCl
	100 µg/ml Proteinase K (add prior to use)
PreMix (PCR)	1x Buffer S
	6% sucrose
	20% SucRed
	0.4 µM dNTP, each
	60 U/ml Taq DNA Polymerase (Peqlab)
SucRed	10 mM Tris, pH 9
	370 µM cresol red
	30% sucrose
Tryptic soy broth (TSB) Buffer	10% PEG 4000
	5% DMSO
	10 mM $MgCl_2$
	10 mM $MgSO_4$
	In LB Broth pH6.1

3 Methods

3.1 Molecular biological techniques

3.1.1 Cloning of the targeting construct

3.1.1.1 Generation and transformation of competent bacteria

KCM competent One shot® Stbl3™ *E. coli* bacteria were used for amplification of manipulated plasmid DNA. To generate a batch of KCM competent bacteria, 5 ml LB medium were inoculated with 100 µl frozen Stbl3 bacteria and grown o/n shaking at 37 °C without antibiotics. 1,6 ml of this preculture were transferred to 100 ml LB medium without antibiotics and grown until an OD of 0.3-0.4 was reached. Bacteria were immediately placed on ice until centrifugation for 10 min at 1000×g and 4 °C. The resulting pellet was resuspended in 10 ml cold TSB buffer and the mixture was incubated on ice for 10 min. 100 µl aliquots of this solution were snap frozen in liquid nitrogen and stored at -80 °C until use.

In order to transform KCM competent bacteria with plasmid DNA, approximately 10 fmol of plasmid DNA were mixed with 20 µl 5x KCM buffer and filled up with dH_2O to 100 µl. This mixture was added to an 100 µl aliquot of competent bacteria immediately after thawing of the bacteria on ice, and incubated for 20 min at 4 °C followed by 10 min at RT. After addition of 1 ml LB medium, the bacteria were grown for 2 h shaking at 25 °C without antibiotics. In the end, various amounts of this culture were streaked on LB agar plates containing the appropriate antibiotics for selection of bacterial clones that were successfully transformed with the plasmid of interest. These plates were incubated at 25 °C until single colonies were visible and reached a size of 1 mm in diameter.

3.1.1.2 Isolation and cloning of plasmid DNA

For amplification and subsequent extraction of plasmid DNA, 5 ml LB medium supplemented with the appropriate antibiotics were inoculated with a single bacterial colony scratched from an LB agar plate with an autoclaved toothpick. Alternatively, glycerol stocks of bacterial clones were used for inoculation. For isolation of small amounts of plasmid DNA, the 5 ml culture was centrifuged for 10 min at 7500 rpm and 4 °C and the bacterial pellet was used for plasmid DNA purification with the QIAprep® Spin Miniprep Kit according to the manufacturer's protocol. If large amounts of plasmid DNA were required, e.g. for a restriction digest followed by gel extraction, 50 to 120 ml LB medium plus antibiotics were inoculated 1:1000 from a saturated 5 ml culture and grown shaking at 25 °C until the solution reached an OD of 1.0-1.3. After subsequent centrifugation for 10 min at 7500 rpm and 4 °C, DNA was

isolated from the bacterial pellet using the QIAGEN® Plasmid Midi Kit or for the final construct the EndoFree® Plasmid Maxi Kit according to the manufacturer's protocol with one exception. After dissolving of the isopropanol precipitated DNA pellet, the DNA was again precipitated by addition of 0.1 volumes of sodium acetate and 2.5 volumes of 100% ethanol and stored at -20 °C o/n or longer. Before use, the precipitated DNA was centrifuged for 30 min at 14000 rpm and 4 °C, the pellet was washed once with 70% ethanol and redissolved in EB buffer. The final DNA concentration was determined with the spectrophotometer NanoDrop® 1000.

All restriction digests were performed with restriction enzymes from New England Biolabs or High Fidelity (HF™) enzymes from New England Biolabs in the recommended buffer and supplemented with 10% BSA where required. Digests were conducted at the optimal reaction temperature for up to 8 h followed by a 20 min inactivation step at 65 or 80 °C according to the manufacturer's recommendation. Conversion of sticky-ended DNA into blunt-ended DNA was conducted with the Quick Blunting™ Kit if required.

The destination vector was usually linearized through a digest with one or two restriction enzymes and dephosphorylated using rAPid alkaline phosphatase. Insert DNA was obtained either directly from a digested plasmid if the antibiotic resistance was different from the resistance of the destination plasmid or by a digest of 30 µg of the plasmid containing the fragment of interest and DNA extraction from an agarose gel. In the latter case, the band corresponding to the desired fragment was excised and DNA was isolated using the QIAquick® Gel Extraction Kit. For insertion of very small DNA fragments, two complementary single stranded DNA oligonucleotides with single strand overhangs suitable for ligation into the digested destination vector were annealed. Therefore, 19 µl of each oligonucleotide at an initial concentration of 100 µM were mixed with 2 µl 20x Oligo Annealing Buffer and incubated according to the conditions depicted in Table 3-1. Annealed oligonucleotides were then used in two different dilutions (1:50 and 1:500) for ligation.

Table 3-1: Oligo annealing conditions.

98 °C	10 sec
95 °C	3 min
Ramp down from 90 °C to 81 °C in 1.0 °C steps	20 sec each
Ramp down from 80 °C to 25 °C in 1.0 °C steps	2 min each

Ligation of 90 fmol of insert DNA and 30 fmol of the destination vector was performed with the enzyme T4 DNA Ligase using the supplied 5x ligase reaction buffer at 22 °C o/n. Alternatively, ligations were carried out with the Quick T4 DNA Ligase using the supplied 2x Quick Ligation Reaction Buffer at 25 °C for 1 h. Shuttling of the rox-frt-stop-frt-PIK3CA^{H1047R}-rox expression cassette into a vector containing *Rosa26* homologous arms was performed with the Gateway® LR Clonase™ technology.

Competent bacteria were transformed with newly generated plasmids (see 3.1.1.1). Single colonies of transformed bacteria were scratched from agar plates using autoclaved toothpicks, dissolved in 40 µl dH_2O and in parallel streaked out on fresh agar plates for further culturing. Dissolved bacteria were boiled for 5 min to release the DNA and polymerase chain reaction (PCR) analysis was performed in order to identify those clones that carry the correct plasmid. Those were then grown in liquid culture for plasmid DNA isolation as described in the beginning of the chapter. Isolated DNA was digested with several restriction enzymes in order to prove correct ligation and total size of the newly generated plasmids. At certain steps additionally sequencing of regions of the plasmid DNA was done by Eurofins Genomics (Ebersberg). Furthermore, glycerol stocks were prepared for long-term storage at -80 °C by mixing 500 µl of a saturated liquid culture with 400 µl glycerol.

3.1.1.3 Cloning strategy for the *pRosa26-FSF-PIK3CA^{H1047R}* targeting vector

A mouse model for the conditional Flp recombinase dependent expression of mutant p110α^{H1047R} was generated by insertion of a rox-frt-stop-frt-PIK3CA^{H1047R}-rox expression cassette into the ubiquitously active *Rosa26* gene locus. The expression of the constitutively active mutant p110α^{H1047R} is silenced by a stop cassette composed of a neomycin resistance gene, three consecutive *SV40* derived pA signals, and an RNA polymerase pausing element. This stop cassette is flanked by two frt sites for removal upon Flp recombinase activity. Rox sites upstream of the first frt site and downstream of the *PIK3CA* open reading frame respectively allow removal of the whole expression cassette via Dre recombinase. This enables Flp mediated activation of the mutant *PIK3CA* followed by Dre mediated deactivation at a later time point.

A modified pENTR^{TM}/D-TOPO® vector containing an frt-stop-frt element was available from previous cloning (pEntr-frt-gt-neostop-frt-MCS-pA) and was digested with PspOMI and SnaBI. A splice acceptor (SA) and subsequent rox site was obtained from the equally available modified pBluescript SK+ vector containing a splice acceptor and the rox-stop-rox element (pBlu-SA-rsr-MCS-pA) by restriction digest with AgeI, conversion into blunt-ended DNA and a second digest with PspOMI. This SA-rox fragment was ligated upstream of the first frt site into the before mentioned pENTR™/D-TOPO® vector. The resulting vector was digested with AscI and SacI and a second rox site was inserted downstream of the pA sequence by ligation with a double strand oligonucleotide consisting of the rox sequence as well as restriction sites for SacI, XhoI and AscI. The vector resulting from this ligation was digested with PfoI to open it between the second frt site and the pA site. The mutant *PIK3CA^{H1047R}* open reading frame was inserted at this position after PfoI digest of a vector from the cloning of the *LSL-PIK3CA^{H1047R}* mouse line and isolation of the corresponding

fragment from an agarose gel. Finally, the whole rox-frt-stop-frt-PIK3CA^{H1047R}-rox expression cassette was cloned into the pRosa26-Att-CCDB-Att vector by use of the Gateway® LR Clonase™ enzyme mix resulting in the *pRosa26-FSF-PIK3CA^{H1047R}* targeting vector. This vector was linearized through digest with PacI immediately before the targeting of embryonic stem (ES) cells.

3.1.2 Isolation of genomic DNA

Isolation of genomic DNA from mouse tail tips or tissues for PCR analysis was done by adding 50 µl DNA lysis buffer (Soriano). Proteinase K was diluted 1:50 in DNA lysis buffer directly before use. Tissue lysis was performed at 55 °C for 90 min followed by proteinase K inactivation at 95 °C for 15 min. The lysed tissue was mixed vigorously and pelleted through centrifugation at full speed for 10 min. The DNA containing supernatant was transferred to new reaction tubes and generally 1 µl was applied in a 25 µl PCR reaction.

Genomic DNA from ES cell clones for screening was isolated from single clone cultures in a 96-well format. After aspiration of the medium, 20 µl DNA lysis buffer (Soriano) containing proteinase K in a dilution of 1:100 were added per well and incubated at 55 °C for 1 h. Subsequently, released DNA was sheared through pipetting and transferred to reaction tubes containing 10 µl dH_2O. Enzyme inactivation was done at 95 °C for 10 min and 2 µl DNA were used in a 50 µl PCR reaction. Unsheared genomic DNA was isolated from selected ES cell clones for PCR amplification of large genomic regions. Therefore, 2 ml ES cell DNA lysis buffer were added to confluent cultures in a 6-well plate after aspiration of the medium. Proteinase K was diluted 1:200 in ES cell DNA lysis buffer directly before use. The lysis was conducted at 55 °C o/n in a wet chamber, 4 ml 100% ethanol were added on the next day without destroying the cell layer and the mix was incubated at RT o/n. The mixture of ES cell DNA lysis buffer and ethanol was discarded, the cell layer was carefully washed three times with 70% ethanol and subsequently shortly dried. Finally, the DNA was dissolved in 300 µl dH_2O, transferred to reaction tubes without extensive pipetting using cell saver tips and stored at 4 °C.

3.1.3 Polymerase chain reaction

Standard PCR was used for genotyping of murine tail DNA, analysis of recombination in murine tissues, for screening of plasmid DNA during cloning, and for screening and validation of ES cell clones. PCR products were kept at 4 °C until application on an agarose gel.

Genotyping and recombination PCRs on genomic DNA were performed with a *Taq* DNA polymerase at the conditions described in Table 3-2. Specific primers for detecting the presence and zygosity of mutant alleles are listed in Table 2-6 and the annealing

temperatures and sizes of PCR products are given in Table 3-3 for regular genotyping and Table 3-4 for recombination PCRs.

Table 3-2: Reaction mix and conditions for genotyping and recombination PCRs.

Reaction mix		**Conditions**		
12.5 µl	PreMix	95 °C	5 min	
0.3-1.0 µl	forward primer (10 µM)	95 °C	45 sec	
0.3-1.0 µl	reverse primer (10 µM)	55-64 °C	1 min	40x
1.0 µl	DNA	72 °C	1 min 30 sec	
Ad 25 µl	dH_2O	72 °C	5 min	

Table 3-3: Annealing temperatures and PCR products of genotyping PCRs.

(mut=mutant allele; WT=wild type allele)

Name of PCR	**Annealing temperature**	**PCR products (bp)**
Alb-Cre	58 °C	800(mut)/290(internal control)
PIK3CA	64 °C	630(LSL-PIK3CA^{H1047R}); 590(FSF-PIK3CA^{H1047R})
Rosa26	62 °C	400(LSL-PIK3CA^{H1047R}/FSF-PIK3CA^{H1047R})/600(WT)
Pdx1-Cre	64 °C	670(mut)/200(internal control)
R26^{tdTo}	60 °C	580(mut)
R26$^{mT/mG}$	62 °C	450(mut)/600(WT)
LSL-Kras	55 °C	170(mut)/270(WT)
p53^{f}	64 °C	370(mut)/290(WT)
Cdkn2a^{f}	58 °C	180(mut)/140(WT)
p27 knock-out	58 °C	600(mut)
p27 wild type	60 °C	1300(WT)
Pdx1-Flp	55 °C	620(mut)/290(internal control)
rox	64 °C	450(mut)

Table 3-4: Annealing temperatures and PCR products of recombination PCRs.

(mut=mutant allele; del=recombined allele)

Name of PCR	**Annealing temperature**	**PCR products**
PIK3CA del	60 °C	630(mut)/550(del) (LSL-PIK3CA^{H1047R});
		590(mut)/520(del) (FSF-PIK3CA^{H1047R})
R26$^{mT/mG}$ del	62 °C	850(mut)/1020(del)

Screening of plasmid DNA from single colonies was done according to the conditions presented in Table 3-5. Screening primers are listed in Table 2-7.

Table 3-5: Reaction mix and conditions for screening of plasmid DNA.

Reaction mix		**Conditions**		
12.5 µl	PreMix	94 °C	2 min	
0.8 µl	Forward primer (10 µM)	94 °C	45 sec	
0.8 µl	Reverse primer (10 µM)	60 °C	1 min	35x
5.0 µl	DNA	72 °C	1 min 30 sec	
Ad 25 µl	dH_2O	72 °C	5 min	

Due to amplification of relatively long DNA fragments, a HotStarTaq DNA polymerase and special PCR conditions were applied for screening and validation of ES cell clones. Primers for the screening as well as validation of selected ES cell clones are given in Table 2-7. The reaction conditions for the screen are presented in Table 3-6, conditions for the PCRs validating the presence of all components of the targeting construct are shown in Table 3-7.

.

Table 3-6: Reaction mix and conditions for screening of ES cell clones (Touch Down PCR).

Reaction mix		**Conditions**		
2.5 µl	RosES-UP2 (10 µM)	95 °C	17 min	
2.5 µl	RosES-LP1 (10 µM)	72 °C	3 min	
11 µl	5x Q-Solution	95 °C	45 sec	5x
0.35 µl	HotStarTaq	70 °C	3 min	
5 µl	10x Buffer	95 °C	45 sec	5x
1 µl	dNTPs (10 µM each)	69 °C	3 min	
2 µl	DNA	95 °C	45 sec	
Ad 50 µl	dH_2O	68 °C	45 sec	5x
		68 °C	3 min 30 sec	
		95 °C	45 sec	
		67 °C	45 sec	5x
		68 °C	3 min 40sec	
		95 °C	45 sec	
		66 °C	45 sec	5x
		68 °C	3 min 50 sec	
		95 °C	45 sec	
		65 °C	45 sec	5x
		68 °C	4 min	
		95 °C	45 sec	
		64 °C	45 sec	5x
		68 °C	4 min 10 sec	
		95 °C	45 sec	
		63 °C	45 sec	15x
		68 °C	4 min 20 sec	
		68 °C	10 min	

Table 3-7: Reaction mix and conditions for validation of ES cell clones.

Reaction mix		**Conditions**		
2 µl	Forward primer (10 µM)	95 °C	20 min	**PCR3/PCR5/PCR6**
2 µl	Reverse primer (10 µM)	95 °C	35 sec	
0.35 µl	HotStarTaq	65 °C	1 min	ΔT -1°C 10x
5 µl	10x Buffer	65 °C	10 min	
2 µl	dNTPs (10 µM each)	95 °C	35 sec	
1 µl	DNA	55 °C	45 sec	40x
Ad 50 µl	dH_2O	65 °C	10 min	Δt 5 sec
		65 °C	20 min	
2 µl	Forward primer (10 µM)	95 °C	16 min	**PCR2**
2 µl	Reverse primer (10 µM)	95 °C	40 sec	
0.35 µl	HotStarTaq	62 °C	45 sec	45x
5 µl	10x Buffer	65 °C	4 min	Δt 3 sec
1 µl	dNTPs (10 µM each)	65 °C	10 min	
1 µl	DNA			
Ad 50 µl	dH_2O			
2 µl	Forward primer (10 µM)	95 °C	16 min	**PCR4**
2µl	Reverse primer (10 µM)	95 °C	45 sec	
0.35 µl	HotStarTaq	64 °C	45 sec	40x
5 µl	10x Buffer	72 °C	1 min 30 sec	
1 µl	dNTPs (10 µM each)	68 °C	10 min	
1 µl	DNA			
Ad 50 µl	dH_2O			
2.5 µl	Forward primer (10 µM)			**PCR1**
2.5 µl	Reverse primer (10 µM)	Conditions identical with ES cell screen		
11 µl	5x Q-Solution	Table 3-6		
0.35 µl	HotStarTaq			
5 µl	10x Buffer			
1 µl	dNTPs (10 µM each)			
2 µl	DNA			
Ad 50 µl	dH_2O			

Conditioned medium from ES cell clones grown in the absence of antibiotics was tested for the presence of mycoplasm DNA. A mix of seven forward primers and three reverse primers as listed in Table 2-8 was used and the PCR conditions are shown in Table 3-8. Two positive controls were included in each experiment and resulted in a PCR product of approximately 500 bp.

Table 3-8: Reaction mix and PCR conditions for testing for mycoplasm contamination.

Reaction mix		**Conditions**		
15 µl	REDTaq® ReadyMix™	95 °C	15 min	
2 µl	Forward primer mix (10 µM each)	94 °C	1 min	
2 µl	Reverse primer mix (10 µM each)	60 °C	1 min	40x
2 µl	DNA	74 °C	1 min	
Ad 30 µl	dH_2O	72 °C	10 min	

3.1.4 Agarose gel electrophoresis

PCR products or restriction digests were analyzed by analytical agarose gel electrophoresis. Depending on the size of the expected PCR products or DNA fragments, gels containing 0.8 to 2% agarose in TAE buffer were prepared. TAE buffer was used as running buffer in electrophoresis chambers as well. For visualization of DNA, ethidium bromide was added to the agarose gel (0.06 mg/l) and to the running buffer (0.2 mg/l). Usually 12-20 µl sample were applied, and if necessary Orange G solution was added as loading buffer before loading to the gel. DNA standards in the correct size range were loaded on the gel for determination of the band size. These were GeneRuler™ 100bp DNA ladder for bands up to 1000 bp, 2-Log DNA ladder for up to 10 kb and 1 kb DNA extension ladder for very large DNA fragments. The gel was run at 120 V for 1-1.5 h or until the bands were sufficiently separated. Visualization of the band was achieved by UV transillumination with the Gel Doc™ XR+ system.

Preparative agarose gel electrophoresis was performed in the absence of ethidium bromide. GelStar™ Nucleic Acid Gel Stain was used instead for labeling of the DNA, bands were visualized with a Flu-O-Blu illumination table, cut with a scalpel and DNA was isolated using the QIAquick® Gel Extraction Kit.

3.2 Embryonic stem (ES) cell culture

3.2.1 Culture conditions, passaging and cryopreservation

W4/129S6 ES cells were grown on a monolayer of irradiated (34Gray), mitotically inactivated, Geneticin®-resistant mouse embryonic fibroblasts (MEFs) in ES cell medium.

MEFs were seeded on plastic cell culture dishes coated with 0.1% gelatin in MEF medium several hours before seeding of ES cells. The ES cell medium was renewed daily and ES cells were passaged regularly before they reached confluency in order to keep them in an undifferentiated state. Cells were cultivated at 37 °C and 5% CO_2.

For passaging of ES cells the medium was removed, cell culture dishes were washed once with PBS and a sufficient amount of Trypsin/EDTA covering all cells was added. Cells were incubated for 4-5 min at 37 °C, the reaction was stopped by addition of ES cell medium and ES cells and MEFs together were resuspended and seeded in a fresh dish on a MEF monolayer. For cryopreservation, trypsinized cells were centrifuged at RT and 1200 rpm for 5 min and the cell pellet was resuspended in cold ES cell medium supplemented with 10% DMSO. The suspension was transferred to CryoPure tubes, which were slowly cooled down to -80 °C in a precooled freezing container filled with 2-propanol. The tubes were transferred to liquid nitrogen after 24 h for long term storage.

3.2.2 Transfection and selection of ES cells

The linearized targeting vector generated as described in chapter 3.1.1 was shuttled into ES cells through electroporation. ES cells were trypsinized as described above from one 10 cm cell culture dish and counted in a Neubauer hemocytometer. 1×10^7 cells were diluted in 750 µl ice cold PBS and transferred into a pre-cooled electroporation cuvette. 50 µl of the PacI restriction digest containing 25 µg linearized targeting vector were added into the cuvette and mixed. Electroporation was performed using the electroporation system Gene Pulser® II at 250 V and 500 µF. Transfected cells were immediately diluted in pre-warmed ES cell medium and seeded on five MEF-coated 10 cm cell culture dishes.

Selection of clones that integrated the rox-frt-stop-frt-PIK3CA^{H1047R}-rox expression cassette through homologous recombination with the *Rosa26* locus was started 18 h after electroporation by the addition of 250 µg/ml Geneticin® to the ES cell medium. The ES cell medium was subsequently always supplemented with Geneticin® and renewed at least once per day. Those ES cell clones that were still alive after 7 days of selection and had an undifferentiated morphology were picked under the microscope and transferred into 96-well plates. Dissociation of the cells was achieved by incubation in 100 µl trypsin/EDTA at 37 °C for 4 min and subsequent pipetting. 90 µl of the resulting cell suspension were seeded on top of a MEF monolayer in a 24-well plate for expansion. The remaining 10 µl were cultivated in the 96-well plate on plastic until they became confluent. Subsequently, DNA was isolated using the DNA lysis buffer (Soriano) as described in chapter 3.1.2 for ES cell screening. Positive ES cell clones were expanded by passaging into a MEF-coated 6-well plate and subsequently into a MEF-coated 6 cm cell culture dish. Cryopreservation was performed at different passaging steps and cells were seeded in a non-coated 6-well plate for DNA

isolation using the ES cell DNA lysis buffer (chapter 3.1.2). In addition, positive ES cell clones were also cultivated in a non-coated 24-well plate in the absence of antibiotics in order to test for mycoplasm contamination. After 14 days without antibiotics, the conditioned medium from ES clones was processed and analyzed by PCR reaction. The medium was centrifuged at RT and 250×g for 2 min, the supernatant was further centrifuged at RT and 20000×g for 10 min. The resulting pellet was dissolved in 30-50 µl dH_2O and boiled at 95 °C for 3 min for liberation of the DNA and subsequent PCR analysis.

3.3 Mouse experiments

All animal studies were conducted meeting the requirements of the European guidelines for the care and use of laboratory animals and were approved by the local authorities.

3.3.1 Mouse strains

For tissue specific targeted mutagenesis, the Cre-loxP and Flp-frt technologies have been used in this work. This means that tissue specific Cre lines were crossed with conditional alleles containing loxP sites for Cre mediated activation or deletion. Analogous, a Flp mouse line has been crossed with a frt site containing conditional allele. All animals were on a mixed *C57Bl/6*;*129S6/SvEv* genetic background.

Alb-Cre (Postic et al., 1999; Postic and Magnuson, 2000) This transgenic mouse strain was purchased from The Jackson Laboratory. It consists of the fusion of the *albumin* promoter and enhancer region, a nuclear localization sequence-modified Cre recombinase gene and a fragment of the human growth hormone gene.

LSL-PIK3CA$^{H1047R/+}$ (Eser et al., 2013) This knock-in mouse strain was generated in the laboratory of Prof. Dr. Dieter Saur. It consists of a lox-stop-lox silenced mutant $PIK3CA^{H1047R}$ expression cassette targeted to the *Rosa26* gene locus. The expression cassette is flanked by frt sites.

Pdx1-Cre (Hingorani et al., 2003) This transgenic mouse strain was kindly provided by Prof. David Tuveson (Cold Spring Harbor Laboratory, Princeton, NJ, USA). It was generated by injection of the *Pdx1-Cre* transgene into fertilized oocytes.

R26^{tdTo} (Madisen et al., 2010) This reporter mouse strain was purchased from The Jackson Laboratory. It is a *Rosa26* knock-in strain with a lox-stop-lox cassette silencing the *CAG* promoter-driven tdTomato protein expression.

R26$^{mT/mG}$ (Muzumdar et al., 2007) This reporter mouse strain was purchased from The Jackson Laboratory. It is a *Rosa26* knock-in strain where the tdTomato protein is expressed under the control of the *caggs* promoter. As its sequence is flanked by loxP sites, Cre-

mediated recombination results in excision of the tdTomato sequence and subsequent expression of the downstream located EGFP protein (also see Figure 4-5-B).

LSL-Kras^{G12D} (Hingorani et al., 2003; Jackson et al., 2001) This knock-in mouse strain was kindly provided by Prof. Tyler Jacks (Massachusetts Institute of Technology, Cambridge, MA, USA). It consists of a lox-stop-lox cassette followed by a mutant exon 1 carrying the G12D point mutation integrated into the endogenous *Kras* locus.

p53$^{f/+}$ (Jonkers et al., 2001) This knock-in mouse strain was kindly provided by Prof. Anton Berns (Netherlands Cancer Institute, Amsterdam, Netherlands). It is a conditional knock-out mouse strain where the exons 2 to 10 of the *p53* gene are flanked by loxP sites.

Cdkn2a$^{f/+}$ (Aguirre et al., 2003) This knock-out mouse strain was kindly provided by Prof. Nabeel Berdeesy (Harvard Medical School, Boston, MA, USA). It is a conditional knock-out mouse strain where the *Cdkn2a* exons 2 and 3 are flanked by loxP sites. Cre mediated recombination results in deletion of p16 and p19, which are both encoded by this locus due to alternative splicing.

p27$^{+/-}$ (Fero et al., 1996) This knock-out mouse strain was kindly provided by James Roberts (Fred Hutchinson Cancer Research Center, Seattle, Washington, USA). It is a general knock-out strain where the two coding exons of *p27* are replaced by a PGK-neomycin resistance cassette.

Pdx1-Flp (Schönhuber et al., 2014) This transgenic mouse strain was generated in the laboratory of Prof. Dr. Dieter Saur. It consists of the fusion of the *Pdx1* promoter and the codon optimized *Flp-o* coding sequence.

FSF-PIK3CA$^{H1047R/+}$ (not published) This knock-in mouse strain was generated in the laboratory of Prof. Dr. Dieter Saur as part of this work. It consists of a frt-stop-frt silenced mutant PIK3CA^{H1047R} expression cassette targeted to the *Rosa26* gene locus. The expression cassette is flanked by rox sites.

3.3.2 Genotyping

At an age of 2-3 weeks, an approximately 1 mm long piece of the tail tip was cut from an isoflurane anesthetized mouse using a sterile scalpel. This sample was used for isolation of genomic DNA and genotyping PCR analysis. At the same time, earmarks were punched for later identification of the animals.

3.3.3 Serum collection and analysis

Blood samples for serum analysis were taken from living mice from the retrobulbar venous plexus after anesthesia at 1-month intervals starting at an age of two months. Up to 300 µl of blood (not more than 10% of the estimated blood volume) were collected into a Microvette® 500 Z-Gel tube and centrifuged at 20 °C and 10000×g for 5 min. The supernatant containing the serum was used for analysis of aspartate amino transferase, alanine amino transferase, alkaline phosphatase, triglyceride and cholesterol concentrations. The measurements were performed in the routine clinical diagnostic laboratory at the Institute for Clinical Chemistry and Pathobiochemistry (Klinikum rechts der Isar, Technische Universität München, Munich).

3.3.4 Necropsy

Animals that reached a specific time point (1, 3, 6, 9, 12 months) or appeared moribund were euthanized with isoflurane and MMF and were subjected to a focused necropsy. All instruments and the mouse itself were disinfected with 70% ethanol. The mouse's body condition was evaluated, the whole body was weighed and the tail tip was cut to recheck the genotype. The mouse was secured with pins and the ventral skin was dissected away. The abdominal musculature was dissected and all abdominal organs were evaluated for abnormalities. CBD with cystic duct and gallbladder, spleen, pancreas, liver, intestine, kidneys, heart, lung and any abnormal tissue in other structures were dissected, washed in PBS and trimmed. The weight of spleen, pancreas and liver as well as the length of small and large intestine and the CBD diameter were measured and macroscopic pictures were taken as needed with the stereomicroscope Stemi SV 11. Tissue samples were further processed for paraffin sections or frozen sections.

3.4 Histological techniques

3.4.1 Tissue fixation, sectioning and documentation

Dissected and trimmed organs were processed either for paraffin sections or for frozen sections depending on the application. Tissue for paraffin section was fixed in 4% Roti® Histofix for 24 h at 4 °C. Dehydration, clearing and paraffin wax infiltration was performed using the tissue processor ASP300, samples were subsequently embedded in paraffin and stored at RT until further use. A series of 2.5 µm thick sections was prepared with the microtome Microm HM355S. Sections were dried o/n at RT or for 2 h at 37 °C prior to staining. Tissue samples that were used for frozen sections were fixed in 4% Roti® Histofix for 2 h only at 4 °C. A stepwise dehydration was achieved by incubation for 4 h in 15% sucrose followed by 30% sucrose o/n. Samples were embedded in Tissue-Tek® O.C.T.™ compound, snap frozen and stored at -80 °C. The cryostat Micro HM560 was used to

prepare 10 µm thick sections for H&E, Oil Red O or senescence-associated β-galactosidase staining and 30 µm thick sections for confocal microscopy. Frozen sections were stored at -20 °C and dried o/n at RT prior to use.

Stained slides were photographed using the microscope Axio Imager A1 with AxioCam HRc and the software AxioVision 4.8 and saved as .zvi file. Pictures were converted into 8bit .tif images and levels were adjusted in Adobe Photoshop CS4. Confocal pictures of immunofluorescence stainings were acquired using the Leica TCS SP5 DMI 6000 CS microscope equipped with a 40/1.25 oil-immersion objective.

3.4.2 Hematoxylin and eosin staining on paraffin and frozen sections

Paraffin sections were dewaxed in Roti® Histol (2x5 min) and rehydrated in a series of decreasing ethanol concentrations (2x99%, 2x96%, 2x80%). The sections were stained in hematoxylin for 5 sec, washed with tap water for 5 min and stained in eosin for 8 sec. After a series of rising ethanol concentrations (2x80%, 2x96%, 2x99%), the sections were again incubated in Roti® Histol (2x5 min) and subsequently mounted with Pertex mounting medium.

Frozen sections were fixed for 10 min in 4% Roti® Histofix, washed 3 times with PBS and once with dH_2O. The sections were stained in hematoxylin for 15 sec, washed with tap water for 10 min and stained in eosin for 20 sec. After a series of rising ethanol concentrations (2x80%, 2x96%, 2x99%) the sections were incubated in Roti® Histol (2x5 min) and subsequently mounted with Pertex mounting medium.

3.4.3 Immunohistochemistry

Paraffin sections were dewaxed and dehydrated as described in 3.4.2. Antigen retrieval was performed in antigen unmasking solution in a microwave (3 min 800 W, 12 min 360 W) followed by a cool down at RT for at least 30 min. After washing with dH_2O, endogenous peroxidase activity was blocked by incubation in 3% H_2O_2 for 15 min. Following washing with dH_2O and PBS, sections were blocked in 5% serum in PBS containing Avidin (one drop per 200 µl) for 30 min and 5% serum in PBS containing Biotin (one drop per 200 µl) for 30 min. The slides were washed in PBS three times and incubated o/n at 4 °C with the primary antibody diluted 1:50 to 1:300 in 5% serum in PBS. After washing (PBS, PBS 0.1% Tween® 20, PBS), sections were incubated at RT for 1 h with the appropriate biotinylated secondary antibody diluted 1:500 in 5% serum in PBS. Detection was performed using the Vectastain® Elite ABC Kit and DAB peroxidase substrate kit. The sections were counterstained by a short dip into hematoxylin and were dehydrated and mounted as described in 3.4.2.

p27 immunohistochemistry was performed in the group of Prof. Dr. Wilko Weichert (Ruprecht-Karls-Universität, Heidelberg). Dewaxing and dehydration was done in xylene (3x5

min) and a series of decreasing ethanol concentrations (2x100%, 2x96%, 2x70%). Antigen retrieval was performed in Dako Target Retrieval Solution (pH6) for 30 min in a steamer followed by a cool down on ice. Sections were incubated with the primary antibody diluted 1:500 for 1 h at RT. The DCS detection line system (AD050POL-K) was used and staining was performed with Permanent AP Red Kit. The staining was evaluated by an experienced pathologist (Prof. Dr. Wilko Weichert). The intensity of the staining (=strength of expression) as well as the number of p27 expressing cells in the bile duct area and associated neoplastic lesions was investigated. The quantitation of positive cells for the predominant intensity (absent/low/moderate/strong) was given in %.

3.4.4 Oil Red O staining on frozen sections

Frozen sections were fixed for 10 min in 4% Roti® Histofix, washed in 60% isopropanol and incubated in freshly prepared Oil Red O working solution for 15 min. After washing in 60% isopropanol, counterstaining was performed by five dips into hematoxylin and subsequent washing in H_2O. Sections were mounted in aqueous mounting medium.

3.4.5 TOPRO®-3 staining on frozen sections

Frozen sections were fixed for 1 min in 4% Roti® Histofix, washed twice in PBS and incubated in blocking solution (3% BSA, 1% Saponin, 1%Triton-X 100 in PBS) for 1 h at RT. Nuclei were stained with TOPRO®-3 iodide diluted 1:1000 in blocking solution for 2 h in the dark. After washing in blocking solution and PBS, sections were mounted in Vectashield® Mounting Medium and stored at 4 °C until examination.

3.4.6 Immunofluorescence staining on frozen sections

Frozen sections were fixed for 10 min in ice cold methanol, washed in PBS and incubated in blocking solution (1.5% BSA in PBS) for 1 h at RT. The sections were incubated with the primary antibody diluted 1:100 in staining solution (1.5% BSA, 3% goat serum, 0.2% Triton-X 100) for 72 h at 4 °C. After washing in PBS, the secondary antibody Anti-rabbit IgG (H+L) conjugated to DyLight™ 680 fluorescent dye was applied for 48 h at 4 °C. The sections were subsequently washed in PBS, mounted in Vectashield® Mounting Medium and stored at 4 °C until examination.

3.4.7 Senescence-associated β-galactosidase staining on frozen sections

Senescence-associated β-galactosidase staining was performed with reagents from the Senescence beta-Galactosidase Staining Kit. Frozen sections were rinsed with PBS, fixed with the Fixative Solution for 10 min and washed again with PBS. The Staining Solution was prepared according to the manufacturer's protocol and applied on the sections o/n at 37 °C.

After washing in PBS, counter staining was performed in Nuclear Fast Red and the sections were dehydrated and mounted as described in 3.4.2.

3.5 Statistical analysis

Graphical representations and statistical tests except for the Wilcoxon Rank Sum test were performed in GraphPad Prism 5 (La Jolla, CA, USA). The Wilcoxon Rank Sum test was calculated in R Language (R Development Core Team, 2014).

4 Results

4.1 Analysis of the role of PI3K signaling in liver tumorigenesis

The PI3K-AKT-mTOR signaling pathway is aberrantly activated in many human tumors including liver cancer. Up to 45% of HCC and more than 50% of CCC cases show activation of this pathway although mutations in the *PIK3CA* gene itself occur in less than 10% (Sahin et al., 2004; Boyault et al., 2007; Chung et al., 2009; Simbolo et al., 2014; Riener et al., 2008; Schulze et al., 2015; Forbes et al., 2015). Therefore, the effect of constitutive PI3K signaling on liver physiology and tumorigenesis was investigated in a GEMM.

4.1.1 Liver specific expression of mutant p110α results in hepatomegaly due to lipid accumulation

A mouse line harboring a knock-in of a conditional *PIK3CA*^{H1047R} hotspot mutation in the *Rosa26* locus was crossed with the liver specific transgenic *Alb-Cre* mouse line for constitutive activation of p110α in the liver of *Alb-Cre;PIK3CA*$^{H10470R/+}$ mice (Eser et al., 2013; Postic et al., 1999). PCR analysis of various tissues from *Alb-Cre;PIK3CA*$^{H10470R/+}$ mice revealed that Cre mediated recombination and thus excision of the lox-stop-lox cassette occurred only in the liver but not in any of the other organs studied (Figure 4-1-A). Nevertheless, the recombined band with a size of 550 bp was present in the liver together with the non-recombined band with a size of approximately 630 bp, possibly due to non-recombined cell types such as fibroblasts or immune cells. Young *Alb-Cre;PIK3CA*$^{H10470R/+}$ mice were examined concerning body weight as well as liver weight and size. The course of body weight gain in the first 3 months was not significantly different between *Alb-Cre;PIK3CA*$^{H10470R/+}$ and control mice for both males and females although there was a tendency that *Alb-Cre;PIK3CA*$^{H10470R/+}$ females had a slightly lower body weight compared to controls (Figure 4-1-B). In contrast, there was a dramatic effect of mutant p110α on the liver weight/body weight ratio already in 1-month-old mice and more extensive in 3-month-old mice (Figure 4-1-C). In control animals, the liver makes up about 5% of the body weight and this ratio remains stable during aging. *Alb-Cre;PIK3CA*$^{H10470R/+}$ mice showed a significantly increased liver weight/body weight ratio of more than 10% at an age of 1 month and the ratio was further increasing to roughly 20% at 3 months of age. Overall, there was a highly significant difference in liver growth between *Alb-Cre;PIK3CA*$^{H10470R/+}$ and control mice although the total body weight was comparable, meaning that other tissues have to be underdeveloped. Indeed, aged *Alb-Cre;PIK3CA*$^{H10470R/+}$ mice are extremely lean on the back while the abdomen is enlarged (data not shown). The increase in liver/body weight ratio is also reflected in the macroscopic aspect of the livers from *Alb-Cre;PIK3CA*$^{H1047R/+}$ mice

compared to control animals (Figure 4-1-D). The entire liver shows an extensive increase in size involving all liver lobes. In addition, the livers from *Alb-Cre;PIK3CA*$^{H1047R/+}$ mice have a tan mottled surface that is paler and less glistening than in control livers. Furthermore, those livers are soft and easily pulled apart.

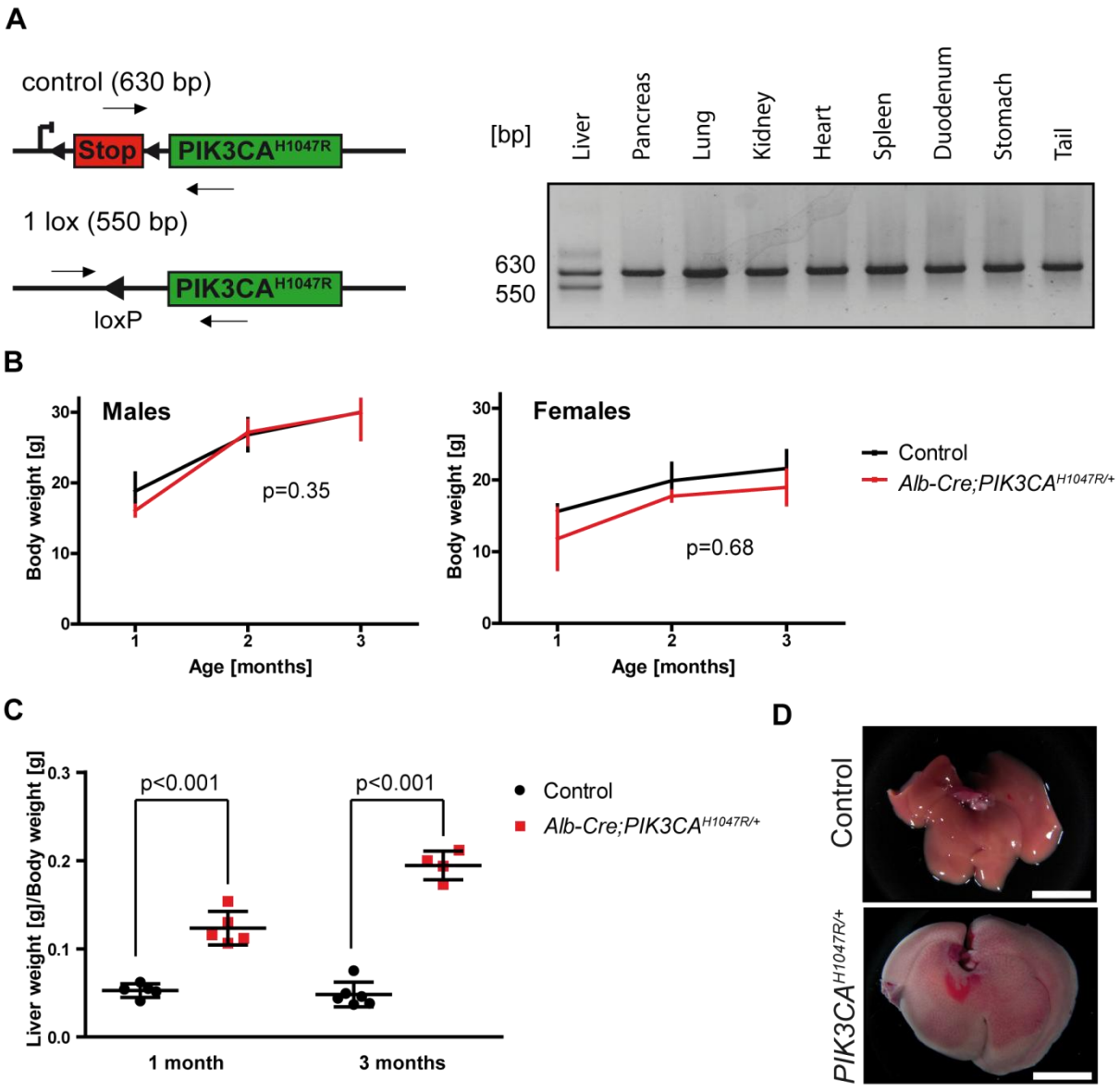

Figure 4-1: Increased liver/body weight ratio in mice expressing mutant p110α in the liver.

A: Recombination scheme of the *LSL-PIK3CA*$^{H1047R/+}$ allele including primers for PCR analysis and PCR analysis of DNA from different tissues from *Alb-Cre;PIK3CA*$^{H1047R/+}$ mice after Cre-mediated recombination. **B:** Body weight of *Alb-Cre;PIK3CA*$^{H1047R/+}$ mice (n=4) and control mice (n=4) separated by sex up to an age of 3 months. Data are represented as mean ± s.d., statistical differences between the two genotypes were assessed by ANOVA for repeated measurements and p-values for the interaction between age and genotype are shown. **C:** Analysis of liver weight relative to body weight in 1- and 3-month-old *Alb-Cre;PIK3CA*$^{H1047R/+}$ mice (n=4-5) and control mice (n=5-6). Each point represents one animal, mean values are shown as horizontal lines, error bars indicate s.d. Two-way ANOVA revealed a strong interaction between age and genotype (p<0.0001). Bonferroni posttests were used to analyze statistical differences between the two genotypes for each time point with p-values indicated in the diagram. **D:** Macroscopic pictures of livers from 3-month-old *Alb-Cre;PIK3CA*$^{H1047R/+}$ and control mice. Scale bars represent 1 cm.

Histological examination of livers from *Alb-Cre;PIK3CA*$^{H10470R/+}$ and control mice revealed the changes underlying the distinct hepatomegaly in *Alb-Cre;PIK3CA*$^{H10470R/+}$ mice (Figure 4-2-A). Representative pictures of H&E stained livers from control mice show the normal liver histology including the typical liver zonation. Periportal hepatocytes surrounding the portal triad consisting of arterioles, venules, bile ductules and lymphatics are highly eosinophilic, while the centrilobular hepatocytes display pale irregular staining due to glycogen accumulation and cytoplasmic clearing (Rogers and Dintzis, 2012). The insert for the 3-month-old control animal shows cells from the centrilobular region, whereas the insert for the 6-month-old control animal magnifies cells from the periportal region. Binucleated cells are not uncommon in the healthy liver and can be observed in the pictures shown here.

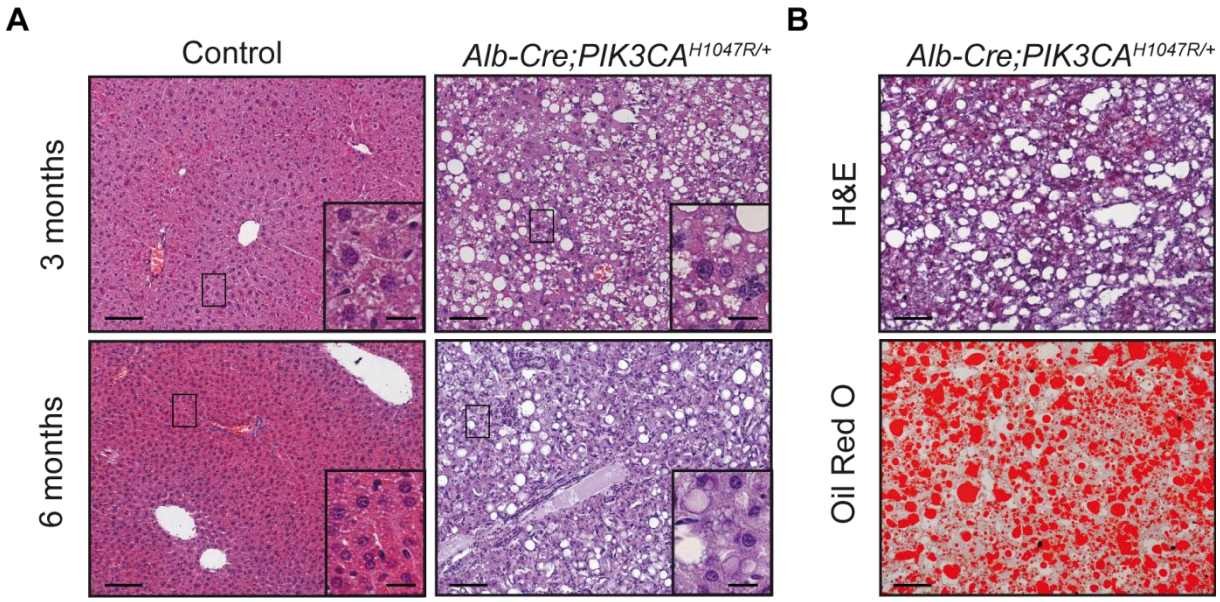

Figure 4-2: Mutant p110α induces lipid accumulation in the liver.

A: H&E staining of liver sections from 3- and 6-month-old *Alb-Cre;PIK3CA*$^{H1047R/+}$ and control mice. Scale bars represent 100 µm in main pictures and 20 µm in inserts. **B:** Liver H&E staining and Oil red O staining on serial frozen sections from a 4-month-old *Alb-Cre;PIK3CA*$^{H1047R/+}$ mouse. Scale bars represent 100 µm.

In contrast, 3-month-old *Alb-Cre;PIK3CA*$^{H10470R/+}$ mice demonstrate a loss of the liver zonation and clear vacuoles within and between the hepatocytes. The hepatocytes are polygonal, mostly large with indistinct margins and abundant, amphophilic cytoplasm filled with vacuoles. Nuclei are round to ovoid, paracentral or eccentric, marginated with finely stippled chromatin and one to five deeply eosinophilic nucleoli per nucleus. There is marked anisocytosis and anisokaryosis and cells with giant nuclei as well as binucleated cells are present. Similar changes have been observed in 6-month-old *Alb-Cre;PIK3CA*$^{H10470R/+}$ mice. The cytoplasm is even less eosinophilic than at 3 months of age, the content of vacuoles is more elevated and immune cell infiltration occurs. Oil Red O staining on frozen sections revealed that the clear vacuoles seen on processed and paraffin embedded tissue correspond to lipid deposits (Figure 4-2-B). In summary, *Alb-Cre;PIK3CA*$^{H10470R/+}$ mice

display severe hepatomegaly with an early onset due to extensive lipid accumulation affecting the entire liver.

4.1.2 Signs of liver damage and increased cholesterol production in mice expressing mutant p110α in the liver

The findings that the physiological liver architecture, which is essential for normal liver function, is lost in *Alb-Cre;PIK3CA*$^{H10470R/+}$ mice suggested that severe liver damage with systemic implications might occur in these mice. In addition, *Alb-Cre;PIK3CA*$^{H10470R/+}$ mice exhibited a high fluctuation in their health condition with short periods of apathy followed by normal behavior (data not shown), which prompted us to analyze the serum of these mice. Quantification of liver enzymes in the serum can provide hints about disturbed hepatocyte integrity or cholestasis (Giannini et al., 2005). Elevated serum concentrations of the aminotransferases aspartate amino transferase and alanine amino transferase indicate a hepatocellular predominance of the disease whereas increased serum alkaline phosphatase argues for a cholestatic predominance (Giannini et al., 2005; Pratt and Kaplan, 2000). The hepatic enzymes mentioned above as well as serum triglycerides and total cholesterol were measured in the serum of *Alb-Cre;PIK3CA*$^{H10470R/+}$ and control mice at different time points (Figure 4-3-A). The results were mainly consistent between 3-month-old, 6-month-old and more than 6-month-old animals. *Alb-Cre;PIK3CA*$^{H10470R/+}$ mice displayed a more than two-fold increase in serum alkaline phosphatase and serum cholesterol with a high significance. Serum levels of alanine amino transferase were up to 15-fold increased in *Alb-Cre;PIK3CA*$^{H10470R/+}$ mice. In contrast, aspartate amino transferase levels did not significantly differ between *Alb-Cre;PIK3CA*$^{H10470R/+}$ mice and controls at 3 and 6 months of age, but there was a significant increase in older *Alb-Cre;PIK3CA*$^{H10470R/+}$ mice. Last, serum triglyceride levels were moderately reduced in 3-month-old *Alb-Cre;PIK3CA*$^{H10470R/+}$ mice compared to controls, but did not reveal any significant differences at later time points.

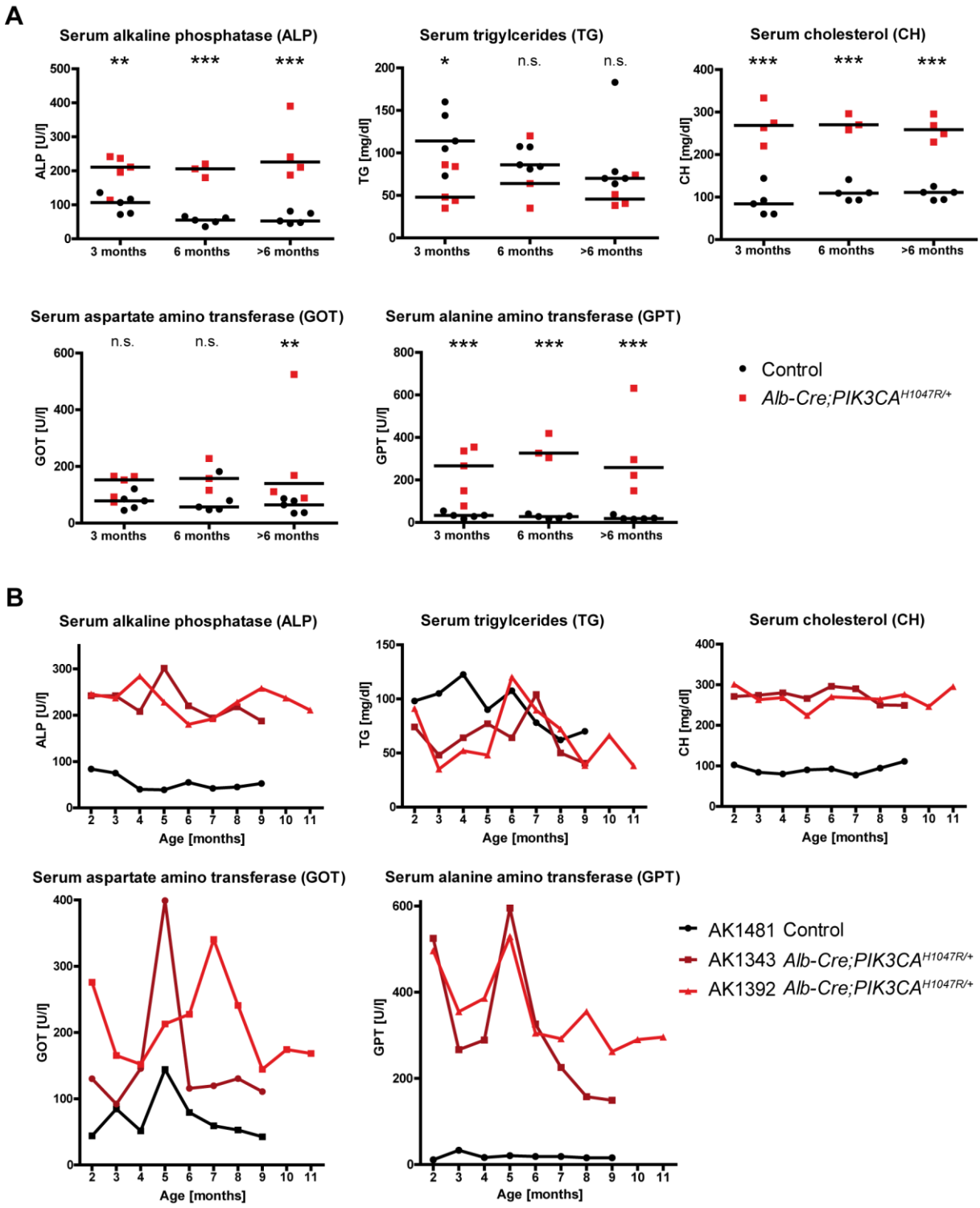

Figure 4-3: Expression of mutant p110α in the liver results in liver damage and increased serum cholesterol.

A: Biochemical analysis of serum taken at the indicated time points from *Alb-Cre;PIK3CA*$^{H1047R/+}$ (n=3-5) and control mice (n=5). Each point represents one animal, repetitive sampling was possible but not always the case. The median values are displayed as horizontal lines. On the assumption of a log-normal distribution of the serum concentrations, the two different genotypes were compared by two-way ANOVA calculation on log-transformed data with the following results: The genotype had a significant effect on all serum parameters averaged over the time points (ALP p<0.0001, TG p=0.0012, CH p<0.0001, GOT p=0.0004, GPT p<0.0001) while only the alkaline phosphatase concentration showed a significant interaction between genotype and age (p=0.012). Bonferroni post testing was used to compare the two genotypes for each time point (n.s., not significant; *p=0.01 to 0.05; **p=0.001 to 0.01; ***p < 0.001). **B:** Biochemical analysis of serum taken monthly from two *Alb-Cre;PIK3CA*$^{H1047R/+}$ mice and one control mouse.

A monthly long-term observation of serum parameters from two *Alb-Cre;PIK3CA*$^{H10470R/+}$ mice and one control animal was used to address the question if liver damage or lipid concentrations undergo fluctuations that might account for the varying health condition observed in *Alb-Cre;PIK3CA*$^{H10470R/+}$ mice (Figure 4-3-B). Concentrations of alkaline phosphatase, alanine amino transferase and cholesterol were considerably increased in *Alb-Cre;PIK3CA*$^{H10470R/+}$ mice over a period of 2 to 11 months of age thus underpinning the highly significant differences observed at distinct time points. While the cholesterol concentration remained stable between 200 and 300 mg/dl, the concentrations of alkaline transferase and alanine amino transferase underwent considerable fluctuations but remained always clearly elevated compared to controls. The most extensive variations were observed for aspartate amino transferase concentrations in *Alb-Cre;PIK3CA*$^{H10470R/+}$ mice ranging from 100 to 400 U/l in one animal, but this parameter was also fluctuating in the control mouse. Serum triglyceride concentrations were equally fluctuating in both *Alb-Cre;PIK3CA*$^{H10470R/+}$ and control mice and the curves were overlapping explaining why no significant difference was observed in 6-month-old and older mice. Taken together, these results indicate that the liver of *Alb-Cre;PIK3CA*$^{H10470R/+}$ mice is severely damaged already at an age of 3 months and that serum cholesterol levels are highly increased.

4.1.3 Mutant p110α drives hepatocellular and intrahepatic cholangiocellular carcinogenesis

In order to study the effect of constitutive PI3K pathway activation on liver tumorigenesis, *Alb-Cre;PIK3CA*$^{H10470R/+}$ mice were monitored longitudinally until they showed distinct signs of disease. The median survival of these mice was 160 days, thus being significantly shorter than the median survival of control mice (Figure 4-4-A). Not all of these mice died due to tumor burden but rather due to the liver damage described above. Especially *Alb-Cre;PIK3CA*$^{H10470R/+}$ mice younger than 142 days neither harbored macroscopically visible tumors nor microscopically detectable lesions, but severe hepatomegaly and liver steatosis. In contrast, all *Alb-Cre;PIK3CA*$^{H10470R/+}$ mice that survived until an age of more than 196 days developed liver tumors, while the tumor incidence was 60% in 143- to 196-day-old animals. Figure 4-4-B shows two examples of the tumor burden in livers from older *Alb-Cre;PIK3CA*$^{H1047R/+}$ mice. Usually, all liver lobes were affected with a prevalence on the ventral side. Up to 50% of the liver were covered by multifocal, nodular tumors with a diameter of 1 mm up to 1.5 cm. The tumors were tan, firm and in part prominently vascularized. Histological evaluation revealed that both HCCs and CCCs were present in livers from *Alb-Cre;PIK3CA*$^{H10470R/+}$ mice as shown in representative examples in Figure 4-4-C. The upper row shows a 1 mm diameter nodular, moderately cellular, relatively well demarcated expansile liver mass with a pseudocapsule of compressed ducts and fibrous tissue. The tumor cells have a compact arrangement and are densely packed where lipid

deposition is absent. The cells are polygonal, moderately sized to large with abundant amphophilic, granular cytoplasm and indistinct margins. Nuclei are round, central or paracentral with finely stippled marginated chromatin and one to four large and deeply eosinophilic nucleoli. The mass displays occasional karyomegaly, bi- or trinucleated cells and few aberrant mitotic figures. Occasional invasion of the pseudocapsule and inflammation could be observed. The majority of the cells stains positive for the HCC marker HepPar1 while only ductules are positive for the ductal marker CK19.

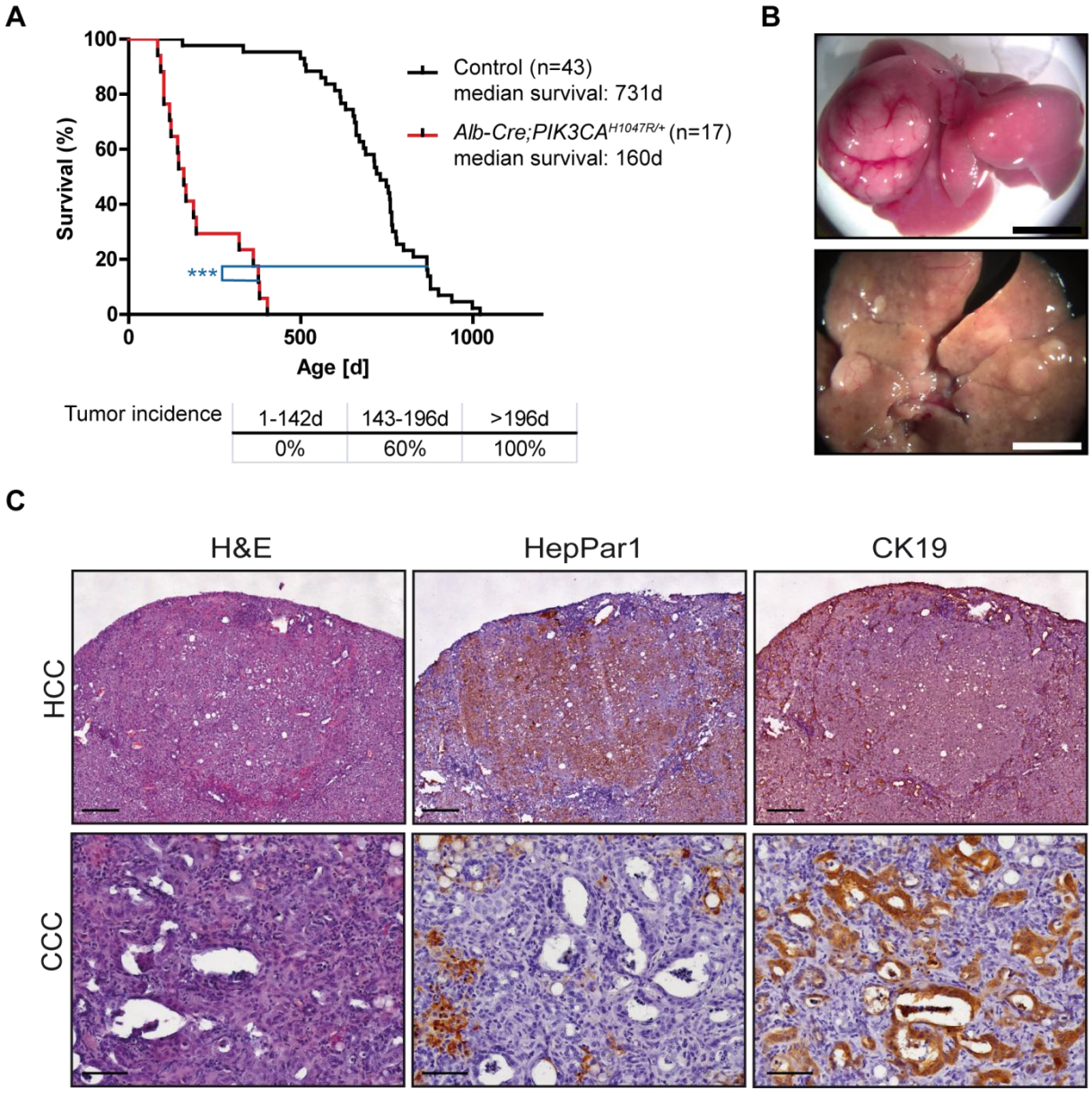

Figure 4-4: Mice expressing mutant p110α in the liver show reduced survival and formation of HCC and CCC.

A: Kaplan-Meier survival curves of the indicated genotypes (***p < 0.001, log-rank test). Tumor incidence in *Alb-Cre;PIK3CA*$^{H1047R/+}$ mice is indicated for different age intervals. **B:** Macroscopic pictures of liver tumors from *Alb-Cre;PIK3CA*$^{H1047R/+}$ mice. Scale bars represent 1 cm. **C:** H&E staining and HepPar1 as well as CK19 immunohistochemistry on paraffin sections of liver tumors from *Alb-Cre;PIK3CA*$^{H1047R/+}$ mice. HepPar1 and CK19 serve as markers for hepatocellular carcinoma (HCC) and cholangiocellular carcinoma (CCC) respectively. Scale bars represent 200 µm in HCC pictures and 50 µm in CCC pictures.

The lower row shows part of a densely packed, poorly demarcated, irregularly shaped and infiltrative liver mass. The tumor cells display a tubular and dense arrangement surrounded by abundant stroma. The tumor cells are cuboidal, moderately sized with indistinct margins and a moderate amount of eosinophilic to amphophilic homogenous cytoplasm. Nuclei are round to ovoid, centrally located, with sparse finely stippled chromatin and one to three small nucleoli. In contrast to the other lesion, HepPar1 staining is not detectable in this tumor, but the tumor cells show distinct CK19 positivity while the stroma is negative for both markers. Tumors of both hepatocellular and cholangiocellular origin could be observed within the same animal. Altogether, these data suggest that mutant *PIK3CA* drives hepatocellular as well as intrahepatic cholangiocellular carcinogenesis with a long latency.

4.2 Analysis of molecular mechanisms involved in extrahepatic cholangiocellular carcinoma formation

Given the importance of mutant p110α in inducing intrahepatic cholangiocellular carcinogenesis, the question arose if mutant p110α equally plays an important role in extrahepatic CCC formation. Although both intrahepatic and extrahepatic CCCs arise from cholangiocytes, they considerably differ concerning mutations and pathways involved in tumorigenesis as described in chapter 1.1.2. In addition, they derive from different progenitor cell lineages – intrahepatic cholangiocytes from Alb^+ common liver precursors, and extrahepatic cholangiocytes from $Pdx1^+$ progenitors. Therefore, findings obtained in intrahepatic CCCs cannot directly be extrapolated to extrahepatic CCCs. As described in chapter 1.1.3, appropriate mouse models for the study of extrahepatic CCCs are mostly lacking. In this work, the combination of the two existing mouse lines *Pdx1-Cre* (Hingorani et al., 2003) and *LSL-PIK3CA*^{H1047R} (Eser et al., 2013) gave rise to a GEMM for p110α-induced extrahepatic CCC, which was further used as a starting point for the analysis of additional molecular players involved in extrahepatic CCC formation.

4.2.1 Targeting of the extrahepatic bile duct via *Pdx1-Cre* and characterization of the *Pdx1-Cre;PIK3CA*$^{H1047R/+}$ mouse model

The homeodomain-containing transcription factor Pdx1 is expressed in the developing pancreas, duodenum, antral stomach, and CBD (Ohlsson et al., 1993; Guz et al., 1995; Offield et al., 1996; Fukuda et al., 2006). Therefore, we speculated that *Pdx1-Cre* is eligible for targeted conditional mutagenesis in the extrahepatic biliary epithelium.

Two different fluorescent reporter mouse lines were used to identify in which tissues *Pdx1-Cre* is active. The *R26*^{tdTo} mouse line (Madisen et al., 2010) gives excellent results in macroscopic stereomicroscopic pictures as there is little background auto-fluorescence that interferes with the tdTomato fluorophore (scheme Figure 4-5-A). The *R26*$^{mT/mG}$ reporter allele

(Muzumdar et al., 2007) results in a switch from membrane tagged red to membrane tagged green fluorescence upon Cre mediated recombination and has been used for confocal microscopy (scheme Figure 4-5-B).

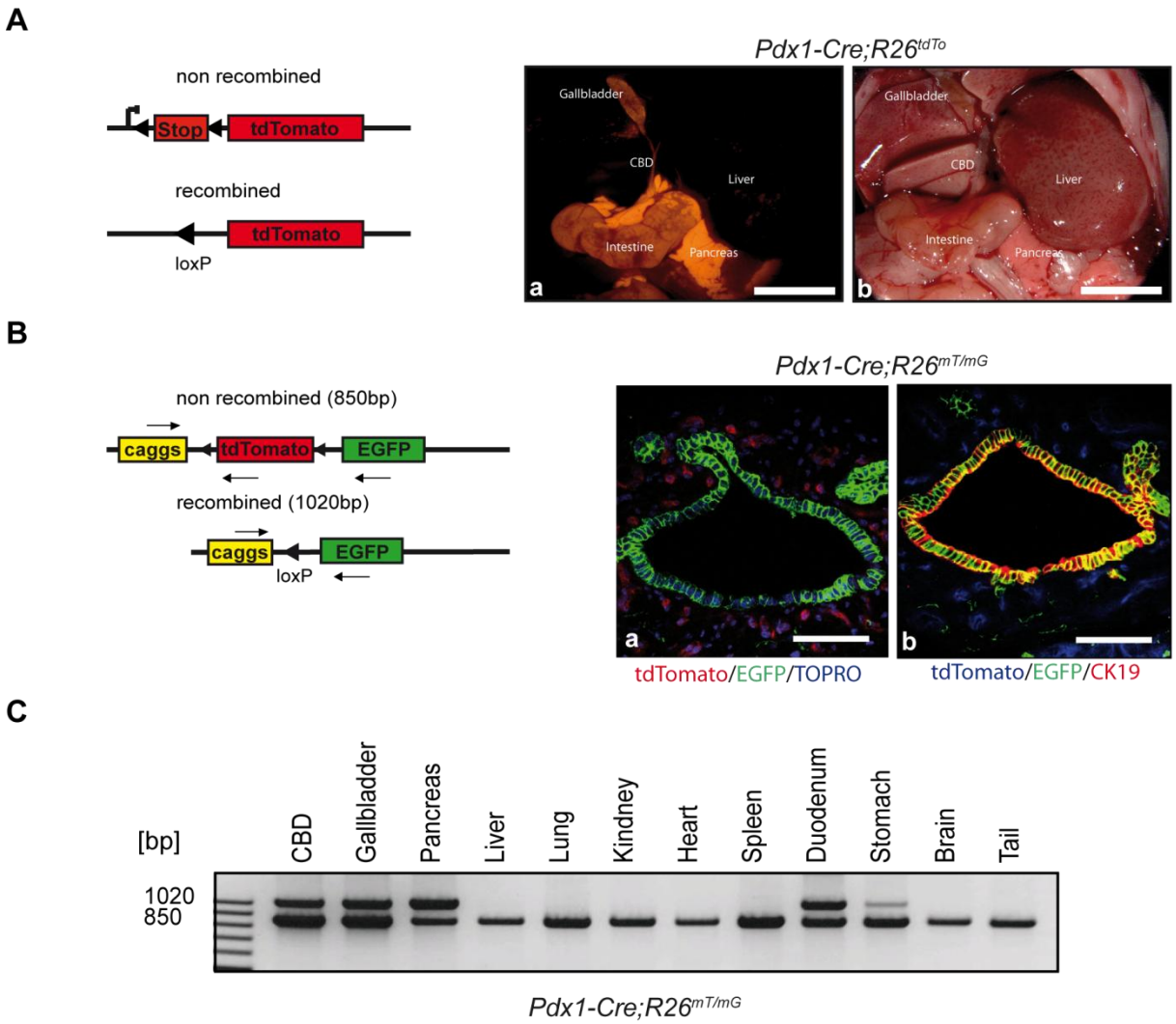

Figure 4-5: *Pdx1-Cre* is active in the epithelium of the extrahepatic bile duct.

A: Recombination scheme of the *R26*^{tdTo} reporter allele and macroscopic fluorescence (a) and bright field (b) pictures of a *Pdx1-Cre;R26*^{tdTo} reporter mouse where the recombined tissues pancreas, duodenum, gallbladder and common bile duct show red fluorescence (a). Scale bars represent 1 cm. **B:** Recombination scheme of the *R26*$^{mT/mG}$ reporter allele including primers for PCR analysis. Confocal microscopic images of tdTomato (red, non-recombined cells) and Cre induced EGFP (green, recombined cells) expression in the extrahepatic bile duct. Nuclei were counterstained with TOPRO-3 (a; blue). CK19 staining reveals colocalization of EGFP positive recombined cells with the bile duct epithelium (b). Scale bars represent 50 µm. **C:** PCR analysis of DNA from different tissues of *Pdx1-Cre;R26*$^{mT/mG}$ mice after Cre-mediated recombination using the primers illustrated in the scheme above.

Figure 4-5-A shows macroscopic fluorescence (a) and bright field (b) pictures of a *Pdx1-Cre;R26*^{tdTo} reporter mouse. The pictures represent the open abdominal cavity with craniodorsal reflection of the right liver lobe in order to enable the view on gallbladder and CBD. The proximal intestine and the pancreas are visible as well. As the expression of the red fluorescence protein tdTomato is dependent on Cre mediated recombination, the localization of the red fluorescence signal reveals *Pdx1-Cre* activity in various tissues. A very

strong and diffuse signal can be observed in the entire pancreas. Gallbladder and CBD exhibit weak red fluorescence, while fluorescence is absent in the liver. The duodenum shows a mosaic like pattern with some spots of strong fluorescence especially in the very proximal region. *Pdx1-Cre* activity in the extrahepatic bile duct epithelium could be confirmed at cellular resolution on frozen sections of *Pdx1-Cre;R26*$^{mT/mG}$ mice (Figure 4-5-B). Recombination occurred exclusively in the epithelium of the extrahepatic bile duct evidenced by EGFP fluorescence while surrounding fibromuscular tissue cells were tdTomato positive (a). Furthermore, EGFP fluorescence colocalized with the immunofluorescence staining for the ductal marker CK19 (b), thus validating *Pdx1-Cre* activity solely in the epithelium. Cre mediated excision of the tdTomato encoding sequence from the *R26*$^{mT/mG}$ allele could also be detected via PCR analysis using primers specifically binding in the tdTomato or EGFP sequence (scheme Figure 4-5-B). The recombination status was assessed in 12 different tissues from a *Pdx1-Cre;R26*$^{mT/mG}$ mouse, revealing recombination in the CBD, gallbladder, pancreas, duodenum and slightly in the stomach (Figure 4-5-C). In all these organs, the lower band showing the non-recombined allele was still present suggesting a mixture of recombined and non-recombined cells. In conclusion, *Pdx1-Cre* is suitable for targeted mutagenesis in the extrahepatic bile duct epithelium, but several other organs are targeted in parallel.

Due to the spectrum of *Pdx1-Cre* activity described above, *Pdx1-Cre;PIK3CA*$^{H1047R/+}$ mice show a multi-organ phenotype with pathological changes in several organs. Representative macroscopic pictures are shown in Figure 4-6-A. Already pancreata from very young mice of an age of 1 month present with increased size and a whitish slightly more firm appearance than in control animals. A large proportion of *Pdx1-Cre;PIK3CA*$^{H1047R/+}$ mice develops cysts and mainly cystic PDAC later on (a). Cysts and carcinomas can occur in head, body and tail of the pancreas. The lesions can be focal or multifocal and coalescing (see picture), they are transparent or turbid, fluctuant and can have solid aspects in advanced stages. Pancreatic tumors reach sizes of up to 2.5 cm^3. Approximately one fifth of *Pdx1-Cre;PIK3CA*$^{H1047R/+}$ mice show lesions in the liver (b). These lesions appear as localized small patches or more diffuse outgrowth mainly projecting on the liver surface on both ventral and dorsal sides. They are irregularly shaped, whitish and soft with a smooth surface. *Pdx1-Cre;PIK3CA*$^{H1047R/+}$ mice additionally exhibit hyperplasia in the duodenum and about one animal in ten develops an adenoma at the most proximal part of the duodenum (c). These adenomas are focal spherical tumors with a diameter of up to 5 mm growing transmurally into the intestinal lumen, and are pale and firm with a corrugated surface. Furthermore, the CBD shows commonly dilatation of few millimeters up to 1.5 cm mainly in the distal part (c). The wall of the bile duct is thickened and can get less transparent with solid aspects and vasculature. Gallstones are rarely observed.

Microscopy of the changes described above reveals more detail as shown in Figure 4-6-B. Panel (a) shows a highly cellular, poorly demarcated, irregular shaped, infiltrative pancreatic mass with a maximum length of 8 mm and a maximum width of 5 mm surrounded by a pseudocapsule. The tumor cells are densely arranged in a tubular pattern supported by an abundant stroma. The cells are cuboidal to columnar, moderately sized showing indistinct margins and a moderate amount of amphophilic, homogeneous cytoplasm. Nuclei are round to ovoid with basal or paracentral location and sparse, marginated chromatin containing one to five eccentric, deeply eosinophilic nucleoli. There is moderate anisocytosis and anisokaryosis and up to 12 mitotic figures per high power field can be observed in the most rapidly growing area with most of them being tri- or quadripolar. Invasion of the stroma occurs. A microscopic representation of the liver lesion (b) depicts areas of decreased eosin staining with clear vacuoles within and between the cells adjacent to normal liver tissue. The cells in this area are polygonal, large, with indistinct margins and abundant, amphophilic, granular cytoplasm filled with vacuoles. The nuclei are mainly round, eccentric or paracentral, with dense, occasionally eosinophilic chromatin containing two to four deeply eosinophilic nucleoli. Marked anisocytosis and anisokaryosis are visible. Histology of the proximal duodenum (c) reveals elongated villi with increased density. The epithelial cells grow in a serrated, densely packed architecture and are columnar, moderately sized with indistinct margins and a moderate amount of amphophilic granular cytoplasm. Nuclei are ovoid to round, basally or paracentrally located with sparse, finely stippled, marginated chromatin and contain up to seven deeply eosinophilic nucleoli. Moderate anisokaryosis and occasional apoptosis are present.

The presence of lesions in the liver was not expected based on the *Pdx1-Cre* activity pattern illustrated in Figure 4-5. Therefore, the nature and origin of the lesions were further analyzed (Figure 4-6-C). Clear vacuoles observed in the aberrant liver areas (a) turned out to be lipid deposits as demonstrated by Oil Red O staining on a parallel frozen section (b) thereby elucidating the presence of focal fatty changes. Furthermore, *Pdx1-Cre;PIK3CA*$^{H1047R/+}$*;R26*$^{mT/mG}$ mice revealed that the fatty changes are directly derived from rare cells displaying *Pdx1-Cre* initiated expression of EGFP and do not occur due to secondary mechanisms.

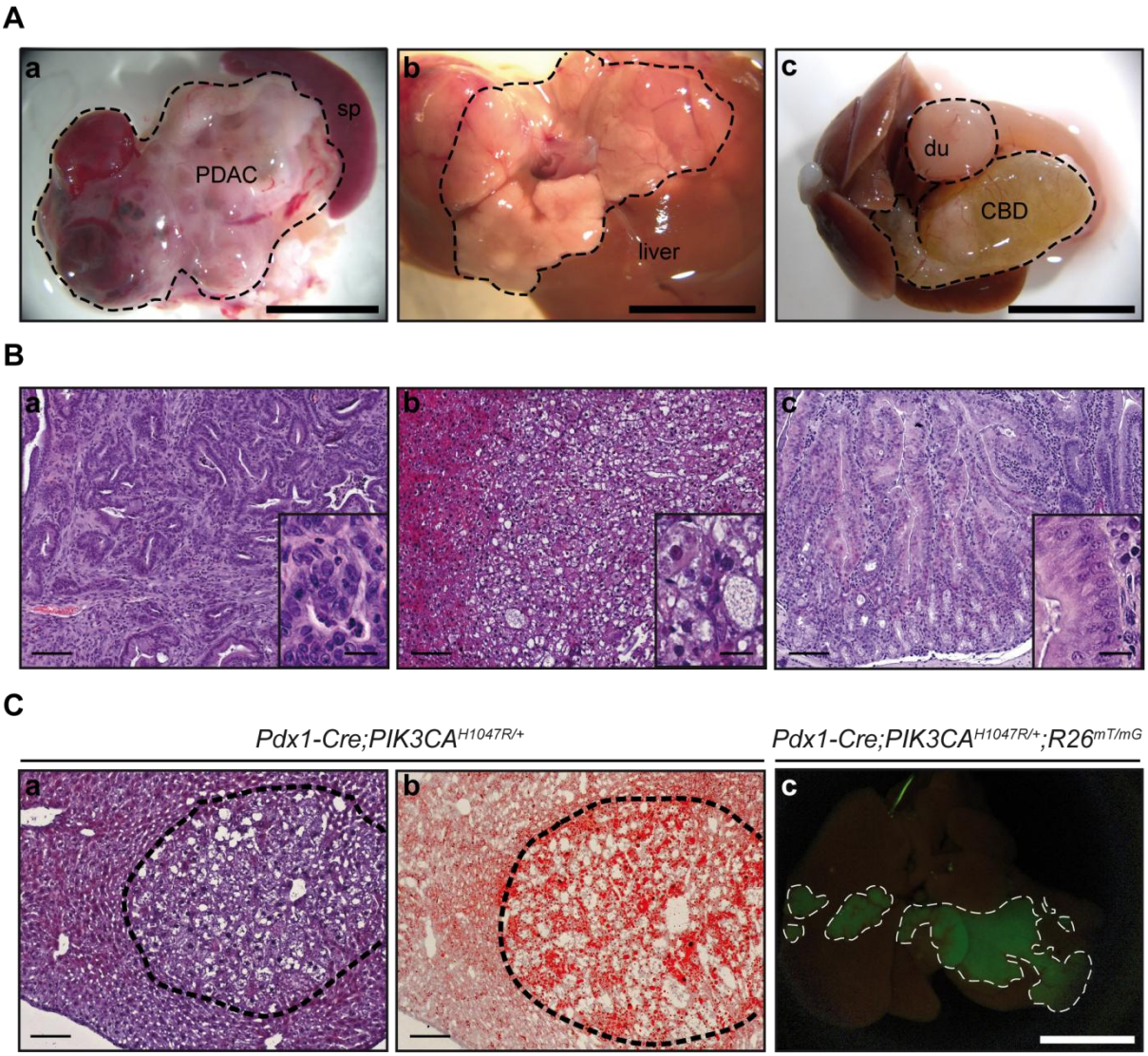

Figure 4-6: *Pdx1-Cre;PIK3CA*$^{H1047R/+}$ mice show lesions in the pancreas, liver, duodenum and bile duct.

A: Macroscopic pictures showing spleen (sp) and PDAC (a), fatty changes (dashed line) in the liver (b), an adenoma in the proximal duodenum (du), and dilatation and solid changes in the common bile duct (CBD) (c) of *Pdx1-Cre;PIK3CA*$^{H1047R/+}$ mice. Scale bars represent 1 cm. **B:** H&E stainings showing PDAC (a), fatty changes in the liver (b), and an adenoma in the proximal part of the duodenum (c) of *Pdx1-Cre;PIK3CA*$^{H1047R/+}$ mice. Scale bars represent 100 µm in main pictures and 20 µm in inserts. **C:** Liver H&E staining (a) and Oil red O staining (b) on serial frozen sections from a 3-month-old *Pdx1-Cre;PIK3CA*$^{H1047R/+}$ mouse, as well as a macroscopic fluorescence picture of a 3-month-old *Pdx1-Cre;PIK3CA*$^{H1047R/+}$*;R26*$^{mT/mG}$ mouse (c) where the recombined tissue appears in green (EGFP). Scale bars represent 100 µm in microscopic pictures and 1 cm in the macroscopic picture.

The CBD phenotype of *Pdx1-Cre;PIK3CA*$^{H1047R/+}$ mice will be described in more detail in the upcoming sections. It has to be kept in mind that *Pdx1-Cre;PIK3CA*$^{H1047R/+}$ mice are never a model of pure bile duct mutagenesis, but that several neoplastic processes in the gastrointestinal tract occur in parallel with differing penetrance and possible interactions with each other.

4.2.2 The *PIK3CA* activating mutation is more relevant in extrahepatic bile duct carcinogenesis than the *Kras* activating mutation

This work will further on mainly focus on the CBD phenotype of *Pdx1-Cre;PIK3CA*$^{H1047R/+}$ mice as there are only few murine studies on the extrahepatic bile duct up to now. The differences in the appearance of CBDs from wild type and *Pdx1-Cre;PIK3CA*$^{H1047R/+}$ mice are already obvious at an age of 6 months (Figure 4-7-A). While the normal bile duct is minuscule with a diameter of less than 0.5 mm, the CBD from *Pdx1-Cre;PIK3CA*$^{H1047R/+}$ mice displays mild dilatation by a few millimeters, thickening of the bile duct wall and whitening of bile duct and gallbladder.

Histological analysis of the CBDs from *Pdx1-Cre;PIK3CA*$^{H1047R/+}$ mice (Figure 4-7-B) revealed the presence of epithelial dysplasia that resembles flat dysplastic lesions described in the human biliary tract (Serra, 2014). These are considered to be the most frequent precursors to malignancy and have been classified as BilIN-1, BilIN-2 and BilIN-3 based on the grade of dysplasia (Zen et al., 2007). All BilIN lesions show a thickening of the biliary epithelium due to elongation of the cells and presence of micropapillary structures but no formation of large intraductal masses. BilIN lesions of different grades can occur within the same animal and there is a smooth, poorly-demarcated transition between adjacent lesions of different grades. BilIN-1 lesions display a flat or micropapillary epithelium and a moderate amount of stroma. Epithelial cells are columnar, moderately sized, with an increased amount of granular cytoplasm and distinct margins. Their nuclei are round to ovoid, located in the basal two thirds of the cell, and show densely packed chromatin and mostly two nucleoli. Mild anisokaryosis is observed. BilIN-2 lesions grow mostly micropapillary with high cellularity supported by an increased amount of stroma. The cells are columnar, moderately sized with an increased amount of granular cytoplasm and indistinct margins. Their nuclei are round to ovoid with variable location resulting in pseudostratification and contain dense, marginated chromatin with mostly two nucleoli. Moderate anisokaryosis and anisocytosis is present. Mostly micropapillary, highly cellular epithelium with "budding off" of clusters of cells into the lumen is characteristic for BilIN-3 lesions. Stroma is abundant and the cells are columnar or polygonal, moderately sized with a moderate amount of granular cytoplasm and indistinct margins. The nuclei are round to ovoid, eccentric or paracentral with sparse finely stippled, marginated chromatin and up to four nucleoli. There is marked anisocytosis and anisokaryosis and more than ten mitotic figures with frequent aberrations are present per high magnification field. Immunohistochemical staining with antibodies specific for AKT activating phosphorylations (threonine 308 and serine 473) as well as for the AKT mediated phosphorylation of GSK3β indicate activation of the PI3K-AKT-mTOR pathway in the CBD epithelium in low-grade and high-grade BilIN lesions. In conclusion, activation of the PI3K-

AKT-mTOR signaling cascade in the CBD epithelium initiated by mutant p110α causes progression through all grades of BilIN lesions thereby reflecting human tumorigenesis.

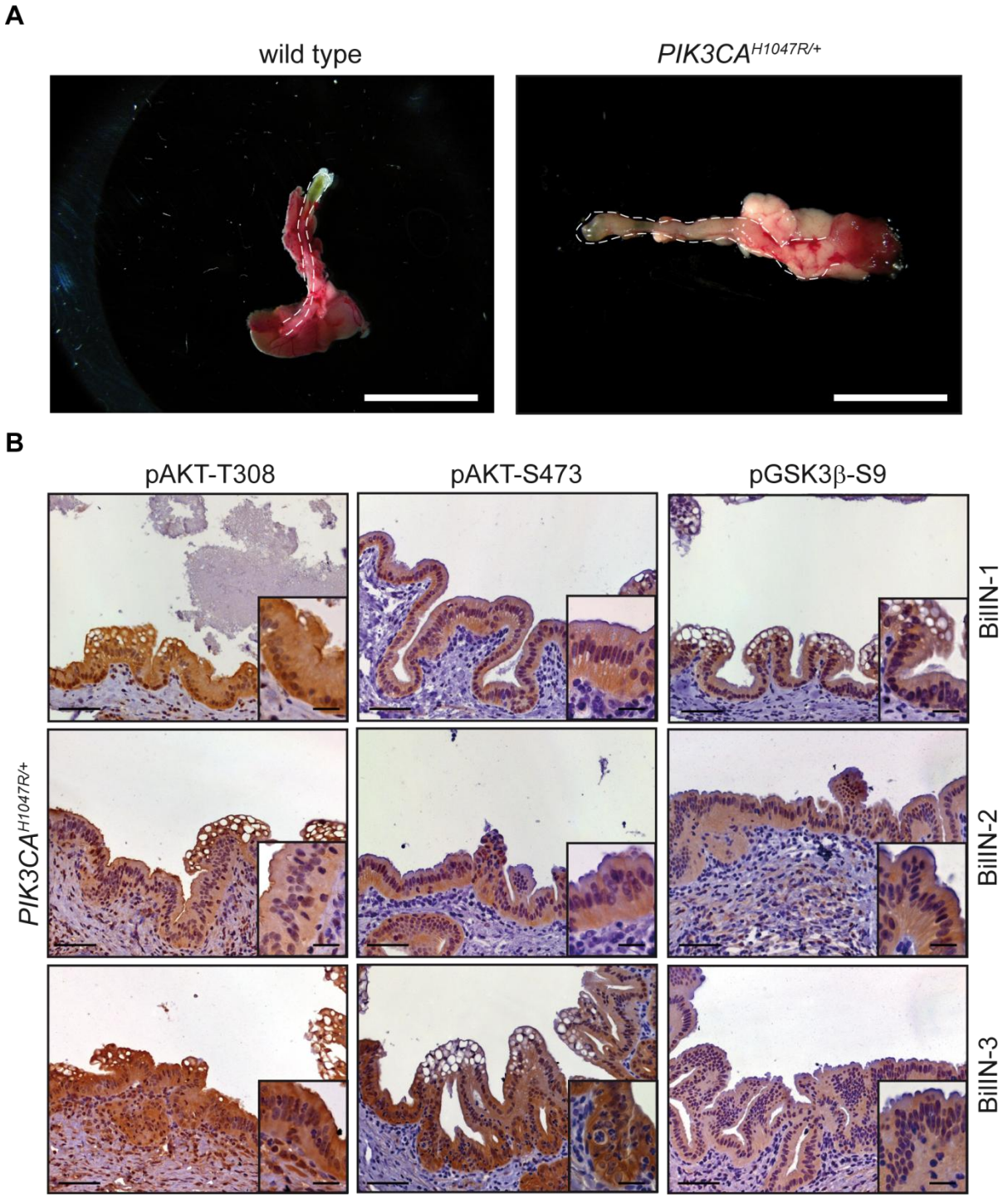

Figure 4-7: *Pdx1-Cre;PIK3CA*$^{H1047R/+}$ mice develop biliary intraepithelial neoplasia.

A: Macroscopic pictures of common bile ducts from 6-month-old wild type and *Pdx1-Cre;PIK3CA*$^{H1047R/+}$ mice. Scale bars represent 1 cm. **B:** Immunohistochemical analysis of PI3K pathway activation in all different BilIN grades from *Pdx1-Cre;PIK3CA*$^{H1047R/+}$ mice. Scale bars represent 50 µm in main pictures and 20 µm in inserts.

Since *Kras* activating mutations have been described in 10-47% of human extrahepatic CCCs (Suto et al., 2000; Deshpande et al., 2011; Voss et al., 2013; Simbolo et al., 2014),

Pdx1-Cre;Kras$^{G12D/+}$ mice were compared to the *Pdx1-Cre;PIK3CA*$^{H1047R/+}$ model. It has been shown in the laboratory of Prof. Dr. Dieter Saur that *Ptf1a*$^{Cre/+}$*;PIK3CA*$^{H1047R/+}$ mice phenocopy the well established *Ptf1a*$^{Cre/+}$*;Kras*$^{G12D/+}$ model, which is widely used for the study of PDAC formation (Eser et al., 2013; Hingorani et al., 2003). Interestingly, *Pdx1-Cre;PIK3CA*$^{H1047R/+}$ mice differ in their phenotype from *Pdx1-Cre;Kras*$^{G12D/+}$ mice. Pictures of the abdominal cavity of 12-month-old mice show the typical neoplastic changes observed in *Pdx1-Cre;PIK3CA*$^{H1047R/+}$ and *Pdx1-Cre;Kras*$^{G12D/+}$ mice compared with wild type mice (Figure 4-8-A). Both genetically modified models show pathological changes in the pancreas with whitish tissue and a cystic PDAC in the *Pdx1-Cre;PIK3CA*$^{H1047R/+}$ mouse depicted here and only mild changes in the *Pdx1-Cre;Kras*$^{G12D/+}$ mouse. Mice from both genotypes frequently display hyperplasia in the duodenum, but dilation of the CBD or neoplasia in the liver occurs only in the *Pdx1-Cre;PIK3CA*$^{H1047R/+}$ model. The CBD at an age of 12 months can be dilated to a diameter of 5 mm or more and the bile duct wall gets turbid.

Histological comparison of the CBD epithelium from the three genotypes at an age of 9 months equally demonstrates marked differences (Figure 4-8-B). The epithelium of wild type mice consists of a thin, uniform layer of cuboidal cells, while the epithelium of *Pdx1-Cre;PIK3CA*$^{H1047R/+}$ mice has undergone malignant transformation. A poorly demarcated, papillary, infiltrative mass originating from the biliary epithelium is shown here. The tumor cells grow in a papillary or tubular pattern supported by abundant stroma. The cells are cuboidal or polygonal, moderately sized, with a moderate amount of granular cytoplasm with vacuoles on the luminal surface and indistinct margins. The nuclei are round to ovoid, eccentric or paracentral, with sparse marginated chromatin and up to seven nucleoli. Marked anisokaryosis can be observed and especially in the very right picture a high number of mitotic figures. The tumor cells invade the stroma. In contrast, the CBD epithelium of *Pdx1-Cre;Kras*$^{G12D/+}$ mice at the same age displays only moderate changes corresponding to BilIN-1 such as nuclear elongation. As in the previous figure, immunohistochemistry was used in order to confirm the PI3K-AKT-mTOR pathway activation. Epithelial cells from both *Pdx1-Cre;PIK3CA*$^{H1047R/+}$ and *Pdx1-Cre;Kras*$^{G12D/+}$ mice display a positive staining with antibodies detecting AKT phosphorylation at threonine 308 or serine 473 or GSK3β phosphorylation at serine 9 indicating activation of the PI3K-AKT-mTOR pathway. In contrast, wild type epithelium only shows mild staining for AKT phosphorylation. In addition, an antibody detecting ERK1/2 phosphorylation at threonine 202 and tyrosine 204 was used to test for RAF-MEK-ERK signaling as a major KRAS effector pathway. All epithelial cells from *Pdx1-Cre;Kras*$^{G12D/+}$ mice stained positive while a small fraction of *PIK3CA* mutant epithelial cells was clearly negative.

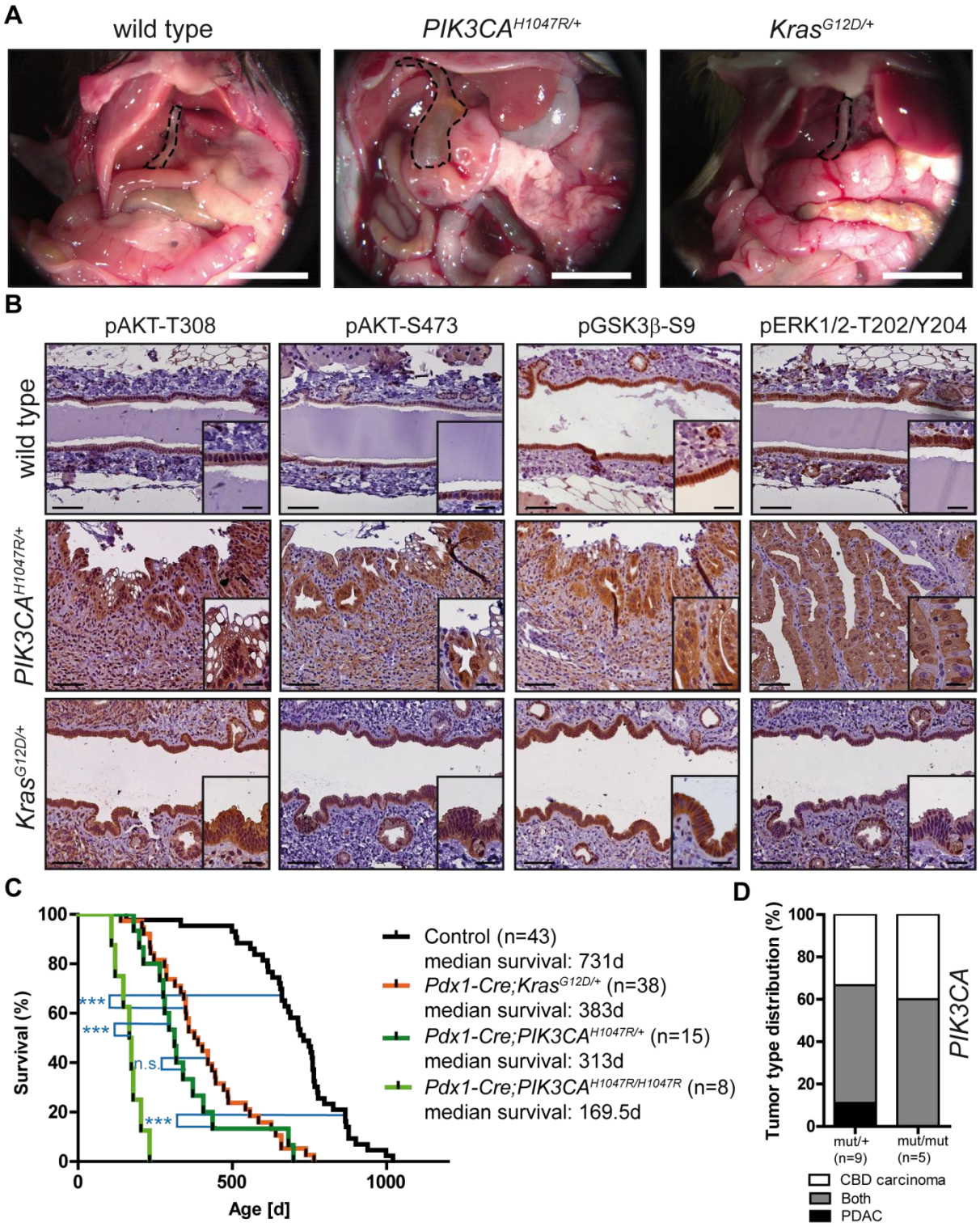

Figure 4-8: Mutant p110α but not mutant Kras can induce tumor formation in the extrahepatic bile duct.

A: Macroscopic *in situ* pictures of 12-month-old wild type, *Pdx1-Cre;PIK3CA*$^{H1047R/+}$ and *Pdx1-Cre;Kras*$^{G12D/+}$ mice. The extrahepatic bile ducts are demarcated by dashed lines, scale bars represent 1 cm. **B:** Immunohistochemical analysis of PI3K and RAS pathway activation in extrahepatic bile duct tissue from 9-month-old wild type, *Pdx1-Cre;PIK3CA*$^{H1047R/+}$ and *Pdx1-Cre;Kras*$^{G12D/+}$ mice. Scale bars represent 50 µm in main pictures and 20 µm in inserts. **C:** Kaplan-Meier survival curves of the indicated genotypes (n.s., not significant; ***p < 0.001, log-rank test). **D:** Tumor type distribution based on histological analysis of common bile duct and pancreas tissue from *Pdx1-Cre;PIK3CA*$^{H1047R/+}$ and *Pdx1-Cre;PIK3CA*$^{H1047R/H1047R}$ mice.

Despite differences between *Pdx1-Cre;PIK3CA*$^{H1047R/+}$ and *Pdx1-Cre;Kras*$^{G12D/+}$ mice concerning the CBD related phenotype, the median survival of both genotypes was similar with 313 and 383 days respectively. There was no significant difference between the two genotypes but both lived significantly shorter than control animals. Furthermore, a gene dose effect of mutant *PIK3CA*^{H1047R} has been observed as *Pdx1-Cre;PIK3CA*$^{H1047R/H1047R}$ mice carrying two copies of the mutant allele exhibited a highly significant further reduction in median survival down to 169.5 days (Figure 4-8C). It has been reported before that *Pdx1-Cre;Kras*$^{G12D/+}$ mice develop PDAC (Hingorani et al., 2003) and carcinomas in the CBD have never been observed in these mice. In contrast, the majority of *Pdx1-Cre;PIK3CA*$^{H1047R/+}$ mice presented with both PDAC and CBD tumor when they reached a condition displaying distinct signs of disease (Figure 4-8-D). Only 11% developed exclusively PDAC and one third showed a CBD carcinoma without presence of PDAC. Homozygous *Pdx1-Cre;PIK3CA*$^{H1047R/H1047R}$ mice even developed CBD carcinomas with full penetrance and 60% harbored both tumor types. Taken together, these results show that mutant Kras induces only mild changes in the extrahepatic bile duct but drives pancreatic carcinogenesis while mutant p110α favors tumor formation in both pancreas and CBD. An increased dose of mutant *PIK3CA* accelerates disease progression and leads to CBD carcinogenesis with 100% penetrance.

The long latency for the development of carcinomas in the extrahepatic bile duct suggests that mutant p110α can initiate carcinogenesis but that cellular protective mechanisms prevent tumor progression and need to be eliminated before carcinomas can form. One established protective mechanism that blocks tumor progression is senescence, a state of stable and long-term cell cycle arrest, which can be induced by high oncogene expression and is found in premalignant lesions. The most constant marker for the *in vivo* study of senescence is senescence-associated ß-galactosidase staining (Collado and Serrano, 2010). Therefore, senescence-associated ß-galactosidase staining was performed on frozen sections of CBD tissue presenting low-grade BilIN lesions. Due to the differences in the CBD related phenotypes described before, CBD tissue from 1- and 3-month-old *Pdx1-Cre;PIK3CA*$^{H1047R/+}$ mice but from a 12-month-old *Pdx1-Cre;Kras*$^{G12D/+}$ mice was used (Figure 4-9-A). While there was no β-galactosidase staining detectable in the CBD of 1-month-old *Pdx1-Cre;PIK3CA*$^{H1047R/+}$ mice, distinct blue crystals formed along the biliary epithelium of 3-month-old *Pdx1-Cre;PIK3CA*$^{H1047R/+}$ mice indicating the presence of senescence. In contrast to that, the epithelium of the 12-month-old *Pdx1-Cre;Kras*$^{G12D/+}$ mouse showed mild neoplastic changes but senescence could not be detected at all. This experiment further confirms, that the two mouse models differ in terms of extrahepatic bile duct carcinogenesis.

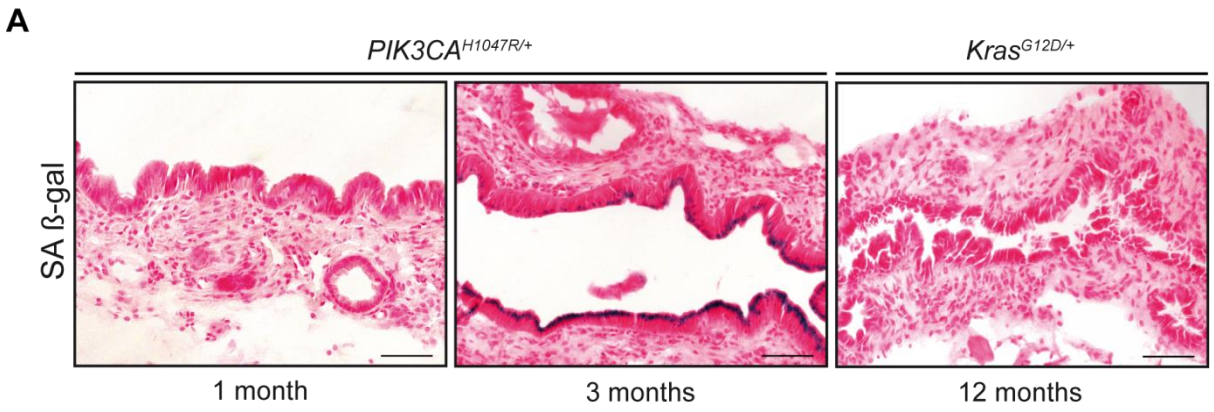

Figure 4-9: Mutant p110α but not mutant Kras induces oncogene-induced senescence in the extrahepatic bile duct.

A: Senescence-associated β-galactosidase staining on frozen sections of the common bile duct from *Pdx1-Cre; PIK3CA*$^{H1047R/+}$ and *Pdx1-Cre;Kras*$^{G12D/+}$ mice at the indicated age. Scale bars represent 50 µm.

4.2.3 p53 loss favors pancreatic carcinogenesis

It has been shown that oncogene-induced senescence is mainly mediated by the three tumor suppressors p53, INK4a and ARF and that loss of these tumor suppressors genes can impair senescence thereby inducing tumor progression (Collado and Serrano, 2010). For this reason, *Pdx1-Cre;PIK3CA*$^{H1047R/+}$ and *Pdx1-Cre;Kras*$^{G12D/+}$ mice were crossed with a mouse line for conditional deletion of *p53* exons 2 to 10 (Jonkers et al., 2001). A heterozygous loss of *p53* in combination with mutant p110α expression significantly reduced the median survival to 150 days compared to 313 days in *Pdx1-Cre;PIK3CA*$^{H1047R/+}$ mice (Figure 4-10-A). A homozygous *p53* knock-out in this model resulted in a further decrease in median survival to only 80.5 days. Besides the fact that loss of the tumor suppressor p53 accelerated tumor formation, it also changed the tumor type distribution to a dominance of pancreatic tumors (Figure 4-10-B). While the great majority of *Pdx1-Cre;PIK3CA*$^{H1047R/+}$ mice developed CBD carcinoma, most of them together with PDAC, only 50% of *Pdx1-Cre;PIK3CA*$^{H1047R/+}$*;p53*$^{f/+}$ mice presented with CBD carcinoma and a total of 60% developed PDAC. This indicates, that p53 loss accelerates pancreatic tumorigenesis to a higher extent than bile duct tumorigenesis. Furthermore, heterozygous loss of *p53* in the *Pdx1-Cre;Kras*$^{G12D/+}$ model significantly reduced survival in a similar way to 138 days (Figure 4-10-A). All *Pdx1-Cre;Kras*$^{G12D/+}$*;p53*$^{f/+}$ mice developed only PDAC. Altogether, the tumor suppressor p53 seems to be more relevant for pancreatic tumorigenesis compared to extrahepatic bile duct carcinogenesis in the investigated mouse models.

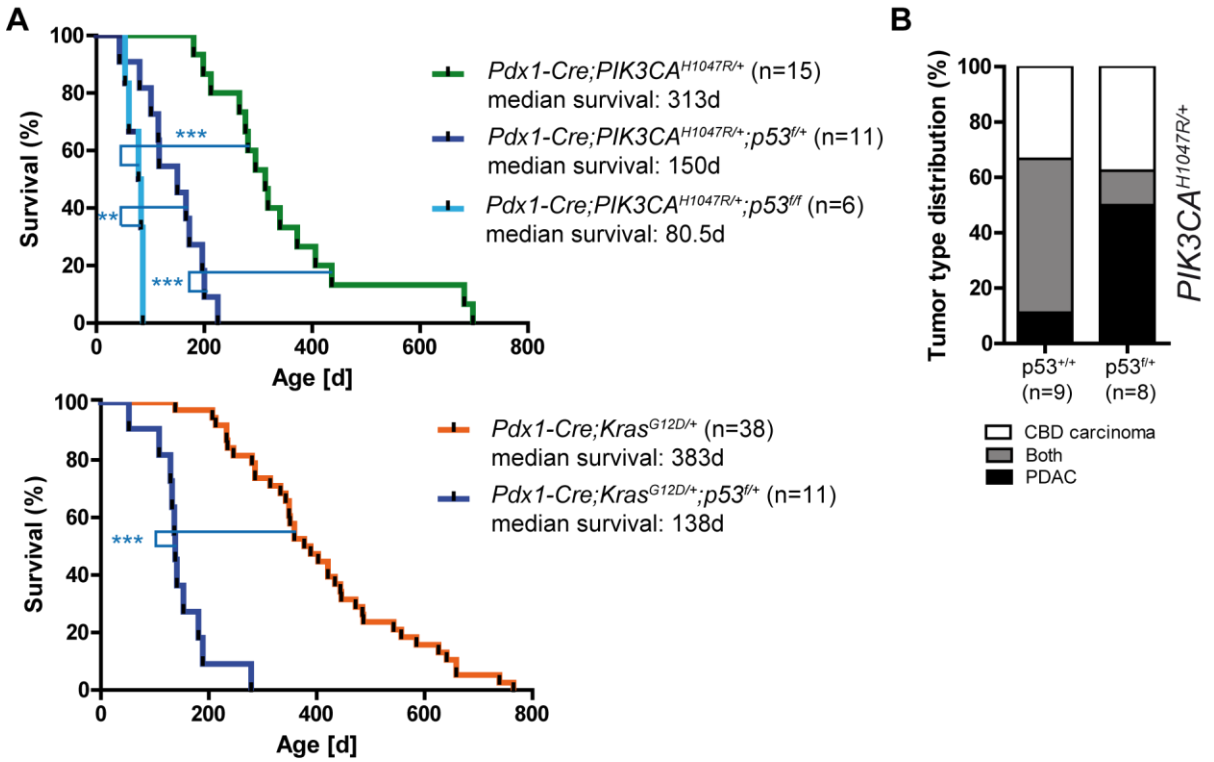

Figure 4-10: The role of p53 in bile duct and pancreatic carcinogenesis.

A: Kaplan-Meier survival curves of the indicated genotypes (**p=0.001 to 0.01; ***p < 0.001, log-rank test). **B:** Tumor type distribution based on histological analysis of common bile duct and pancreas tissue from *Pdx1-Cre;PIK3CA*$^{H1047R/+}$ and *Pdx1-Cre;PIK3CA*$^{H1047R/+}$*;p53*$^{f/+}$ mice.

4.2.4 Disruption of cell cycle regulators is essential for tumor progression in the extrahepatic bile duct

As mentioned before, INK4A and ARF are also thought to induce tumor senescence and are both transcribed from the *CDKN2A* locus via alternative splicing. Their expression itself can serve as a marker of senescence (Collado and Serrano, 2010). *In vivo* analysis of the relevance of Ink4a and Arf (also known as p16 and p19 respectively) has been conducted by the use of a mouse line where the common exons 2 and 3 are floxed, further on termed *Cdkn2a*^{f} (Aguirre et al., 2003). Longitudinal monitoring of *Pdx1-Cre;PIK3CA*$^{H1047R/+}$*;Cdkn2a*$^{f/+}$ mice revealed no significant difference concerning survival when compared to *Pdx1-Cre;PIK3CA*$^{H1047R/+}$ mice (Figure 4-11-A). In addition, the tumor type distribution of *Pdx1-Cre;PIK3CA*$^{H1047R/+}$*;Cdkn2a*$^{f/+}$ mice was similar to that of *Pdx1-Cre;PIK3CA*$^{H1047R/+}$ mice (Figure 4-11-B, left graph). In both genotypes, CBD carcinomas and PDACs frequently occur with a slight dominance of the CBD carcinomas. One case of a full knock-out of *Cdkn2a* in the *Pdx1-Cre;PIK3CA*$^{H1047R/+}$ model has been analyzed so far. This mouse died at an age of 142 days and showed PDAC as well as high-grade BilINs in the CBD.

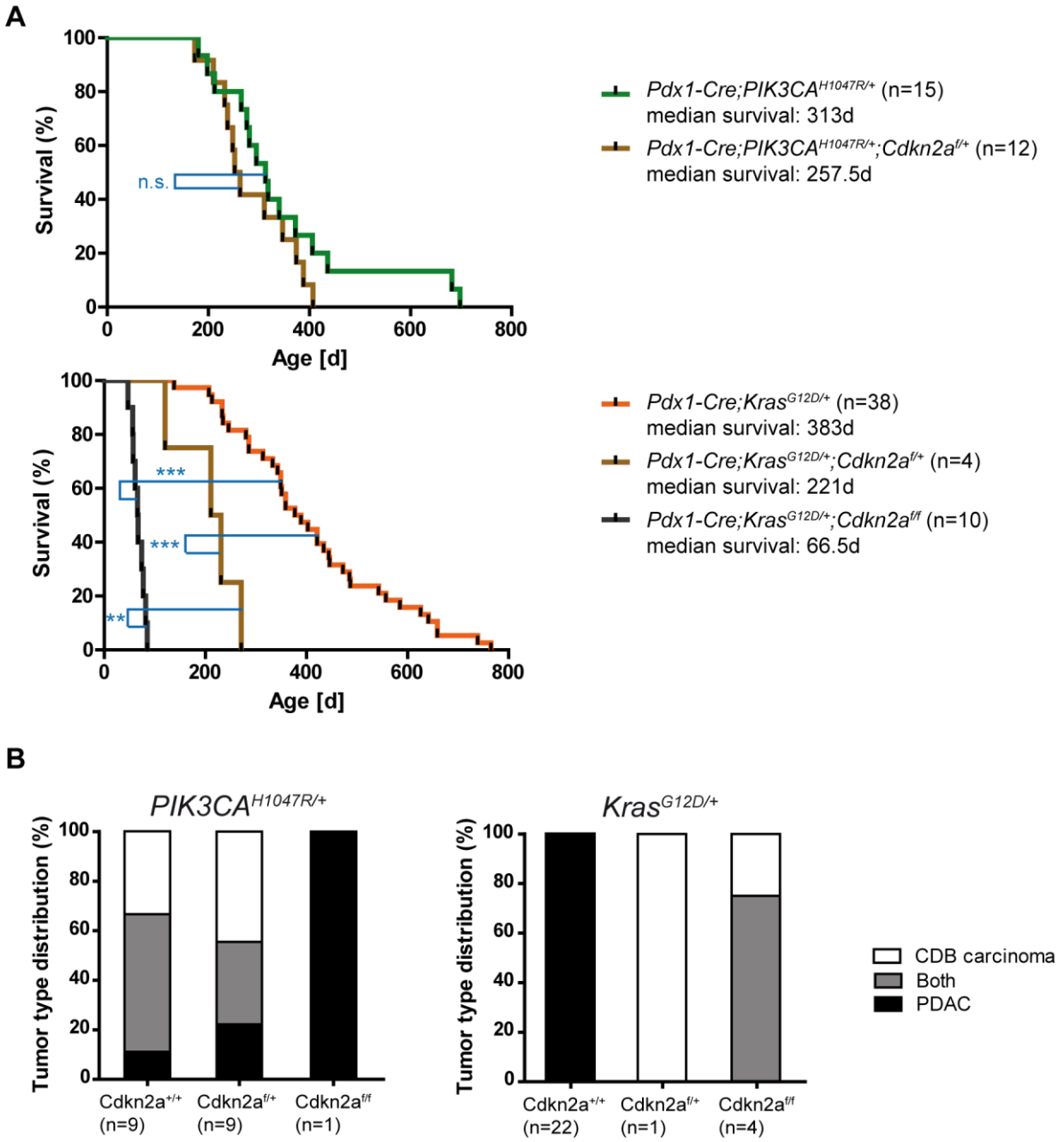

Figure 4-11: Loss of *Cdkn2a* and expression of mutant Kras cooperate in tumor progression in the extrahepatic bile duct.

A: Kaplan-Meier survival curves of the indicated genotypes (n.s., non-significant; **p=0.001 to 0.01; ***p < 0.001, log-rank test). **B:** Tumor type distribution based on histological analysis of common bile duct and pancreas tissue from *Pdx1-Cre;PIK3CA$^{H1047R/+}$*, *Pdx1-Cre;PIK3CA$^{H1047R/+}$;Cdkn2a$^{f/+}$* and *Pdx1-Cre;PIK3CA$^{H1047R/+}$;Cdkn2a$^{f/f}$* mice (left diagram) as well as *Pdx1-Cre;Kras$^{G12D/+}$* (or *Pdx1-Flp;Kras$^{G12D/+}$*), *Pdx1-Cre;Kras$^{G12D/+}$;Cdkn2a$^{f/+}$* and *Pdx1-Cre;Kras$^{G12D/+}$;Cdkn2a$^{f/f}$* mice (right diagram).

A completely different outcome has been observed when combining the *Cdkn2a* loss with the *Pdx1-Cre;Kras$^{G12D/+}$* model. In this case, a heterozygous loss of *Cdkn2a* already reduced the survival significantly down to a median survival of 221 days (Figure 4-11-A). *Pdx1-Cre;Kras$^{G12D/+}$* mice with complete *Cdkn2a* knock-out all died before they reached an age of three months with a median survival of 66.5 days. More importantly, *Pdx1-Cre;Kras$^{G12D/+}$* mice with a heterozygous or homozygous deletion of *Cdkn2a* developed carcinomas in the CBD (Figure 4-11-B, right graph). Only one animal with a heterozygous loss of *Cdkn2a* has

been analyzed histologically and showed only CBD carcinoma. All animals with *Cdkn2a* knock-out developed CBD carcinomas and the majority harbored PDACs as well. These *in vivo* data suggest that *Cdkn2a* is involved in tumor progression in the extrahepatic bile duct, but the requirement for *Cdkn2a* loss depends on the oncogene initiating tumorigenesis. Mutant Kras and *Cdkn2a* deletion seem to cooperate in CBD carcinogenesis, while mutant p110α-driven CBD carcinogenesis does not depend on *Cdkn2a* loss.

Most research on oncogene-induced senescence is based on tumors carrying oncogenic mutations in *RAS* genes or *BRAF* where p53 and INK4A/ARF play an important role (Collado and Serrano, 2010). In contrast, Majumder and coworkers suggested a p27 dependent checkpoint inducing senescence in a mouse model for prostate cancer driven by activated AKT (Majumder et al., 2008). In this study, mice with concomitant AKT activation and loss of one or both *p27* alleles developed invasive cancers while mice expressing only activated AKT were arrested in the prostatic intraepithelial neoplasia state.

Interestingly, immunohistochemical analysis of CBD tissue from wild type, *Pdx1-Cre;PIK3CA*$^{H1047R/+}$ and *Pdx1-Cre;Kras*$^{G12D/+}$ mice revealed a reduction of p27 expression in the extrahepatic bile duct epithelium from *Pdx1-Cre;PIK3CA*$^{H1047R/+}$ mice (Figure 4-12-A), giving a first hint that p27 might be relevant for CBD tumorigenesis. While the percentage of p27 positive epithelial cells was similar in wild type and *Pdx1-Cre;Kras*$^{G12D/+}$ mice at 3, 6, and 9 months of age, there was a tendency for reduced p27 expression in the *Pdx1-Cre;PIK3CA*$^{H1047R/+}$ mice at all time points (Figure 4-12-B). Homozygous *Pdx1-Cre;PIK3CA*$^{H1047R/H1047R}$ mice with an age of 6 months were investigated in addition, showing a significant reduction in p27 positive cells compared to *Pdx1-Cre;Kras*$^{G12D/+}$ mice. These immunohistochemical stainings indicate that the expression of mutant p110α can induce downregulation of p27 whereas expression of mutant Kras does not influence p27 expression. As these differences might contribute to the fact that mutant p110α but not mutant Kras induces tumor formation in the CBD, the role of p27 was further studied *in vivo* using a genetic general knock-out of *p27* (Fero et al., 1996). A heterozygous loss of *p27* in the *Pdx1-Cre;PIK3CA*$^{H1047R/+}$ model significantly shortened the median survival from 313 to 166 days (Figure 4-12-C). In addition, it clearly reduced the tumor formation in the pancreas (Figure 4-12-D, upper graph). All of the *Pdx1-Cre;PIK3CA*$^{H1047R/+}$*;p27*$^{+/-}$ mice developed carcinomas in the extrahepatic bile duct and only a small fraction additionally developed PDAC. Two *Pdx1-Cre;PIK3CA*$^{H1047R/+}$ mice with a complete *p27* knock-out have been analyzed so far and showed both CBD carcinoma and PDAC.

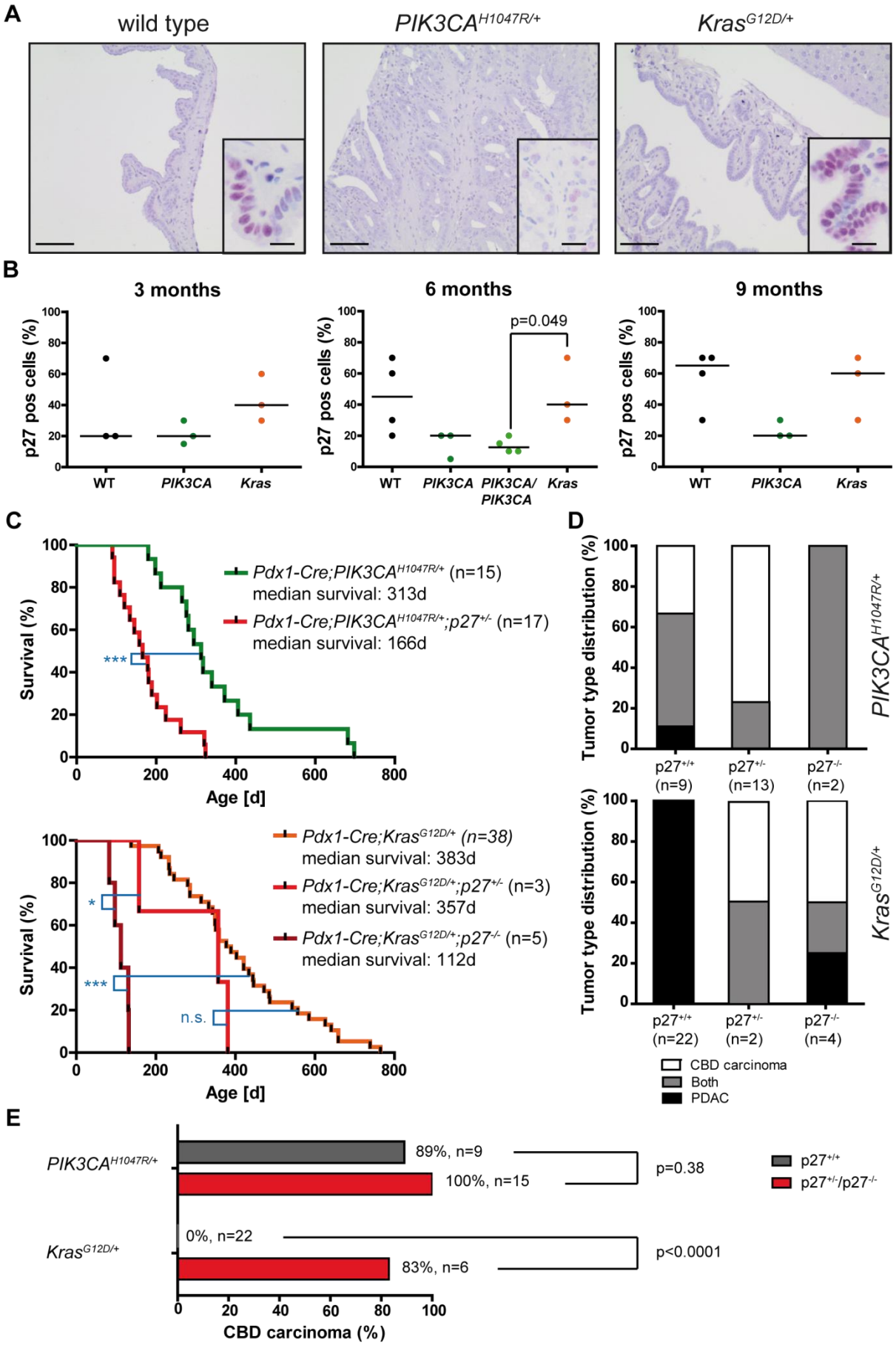

Figure 4-12: Low levels of p27 are induced by mutant p110α and promote tumor progression in the extrahepatic bile duct.

A: Representative p27 immunohistochemistry on paraffin sections of extrahepatic bile ducts from wild type, *Pdx1-Cre;PIK3CA*$^{H1047R/+}$ and *Pdx1-Cre;Kras*$^{G12D/+}$ mice. Scale bars represent 50 µm in main pictures and 20 µm in inserts. **B:** Quantification of p27 positive bile duct epithelial cells in wild type, *Pdx1-Cre;PIK3CA*$^{H1047R/+}$, *Pdx1-Cre;PIK3CA*$^{H1047R/H1047R}$ and *Pdx1-Cre;Kras*$^{G12D/+}$ mice at 3, 6, and 9 months of age (n=3 to 4). Each point represents one animal, horizontal lines represent medians. Kruskal-Wallis testing was performed for each time point and revealed a significant regulation at 6 months only (p=0.03). *Pdx1-Cre;PIK3CA*$^{H1047R/H1047R}$ and *Pdx1-Cre;Kras*$^{G12D/+}$ mice were specifically compared for this time point using the Wilcoxon Rank Sum test as indicated in the graph. **C:** Kaplan-Meier survival curves of the indicated genotypes (n.s., non-significant; *p=0.01 to 0.05; ***p < 0.001, log-rank test). **D:** Tumor type distribution based on histological analysis of common bile duct and pancreas tissue from *Pdx1-Cre;PIK3CA*$^{H1047R/+}$, *Pdx1-Cre;PIK3CA*$^{H1047R/+}$*;p27*$^{+/-}$ and *Pdx1-Cre;PIK3CA*$^{H1047R/+}$*;p27*$^{-/-}$ mice (upper diagram) as well as *Pdx1-Cre;Kras*$^{G12D/+}$ (or *Pdx1-Flp;Kras*$^{G12D/+}$), *Pdx1-Cre;Kras*$^{G12D/+}$*;p27*$^{+/-}$ and *Pdx1-Cre;Kras*$^{G12D/+}$*;p27*$^{-/-}$ mice (lower diagram). **E:** Proportion of mice harboring CBD carcinomas irrespective of PDAC for *Pdx1-Cre;PIK3CA*$^{H1047R/+}$ versus *Pdx1-Cre;PIK3CA*$^{H1047R/+}$*;p27*$^{+/-}$ and *Pdx1-Cre;PIK3CA*$^{H1047R/+}$*;p27*$^{-/-}$ mice as well as *Pdx1-Cre;Kras*$^{G12D/+}$ (or *Pdx1-Flp;Kras*$^{G12D/+}$) versus *Pdx1-Cre;Kras*$^{G12D/+}$*;p27*$^{+/-}$ and *Pdx1-Cre;Kras*$^{G12D/+}$*;p27*$^{-/-}$ mice. Fisher's exact test was performed to analyze the effect of wild type *p27* versus deleted *p27* with p-values indicated in the graph.

In contrast, a heterozygous deletion of *p27* in the *Pdx1-Cre;Kras*$^{G12D/+}$ background did not significantly affect the survival time (Figure 4-12-C), but changed the tumor type distribution fundamentally (Figure 4-12-D, lower graph). Up to now, only two animals have been analyzed histologically and both of them presented with carcinomas in the CBD and one of them harbored a PDAC as well. Despite the very low number of animals, the difference compared to *Pdx1-Cre;Kras*$^{G12D/+}$ only animals, which never develop carcinomas in the CBD, is obvious. A full knock-out of *p27* significantly reduced the median survival compared to both *Pdx1-Cre;Kras*$^{G12D/+}$ and *Pdx1-Cre;Kras*$^{G12D/+}$*;p27*$^{+/-}$ mice down to 112 days. *Pdx1-Cre;Kras*$^{G12D/+}$*;p27*$^{-/-}$ mice equally developed carcinomas in the extrahepatic bile duct but PDAC formation was common as well and could occur in the absence of a CBD carcinoma. Loss of one or both *p27* alleles in the *Pdx1-Cre;Kras*$^{G12D/+}$ model significantly shifted the tumor type distribution towards a biliary tumorigenesis while the proportion of CBD carcinomas was similarly high in *Pdx1-Cre;PIK3CA*$^{H1047R/+}$ and *Pdx1-Cre;PIK3CA*$^{H1047R/+}$*;p27*$^{+/-}$*/p27*$^{-/-}$ mice (Figure 4-12-E). Overall, these data suggest that downregulation of p27 especially promotes tumor progression in the extrahepatic bile duct while PDAC formation is accelerated to a lower extend.

While p53 did not seem to play a major role in tumor formation in the extrahepatic bile duct, p16/p19 and p27 have caught our interest, especially in the context of mutant Kras expression. Besides aged animals, CBD tissues from 3-month-old *Pdx1-Cre;Kras*$^{G12D/+}$, *Pdx1-Cre;Kras*$^{G12D/+}$*;Cdkn2a*$^{f/+}$ and *Pdx1-Cre;Kras*$^{G12D/+}$*;p27*$^{+/-}$ mice have been analyzed histologically as well (Figure 4-13-A). In accordance with the complete absence of CBD carcinomas in old *Pdx1-Cre;Kras*$^{G12D/+}$ mice, 3-month-old *Pdx1-Cre;Kras*$^{G12D/+}$ mice displayed only low-grade neoplasia in the extrahepatic bile duct. In contrast, 66% of *Pdx1-Cre;Kras*$^{G12D/+}$*;Cdkn2a*$^{f/+}$ and 50% of *Pdx1-Cre;Kras*$^{G12D/+}$*;p27*$^{+/-}$ mice of the same age presented already with beginning carcinomas and high-grade BilIN lesions have been observed as well. Histological examples of CBD carcinomas that developed in the *Pdx1-Cre;Kras*$^{G12D/+}$ background upon loss of *Cdkn2a* or *p27* are depicted in Figure 4-13-B.

Tumors from mice with loss of *Cdkn2a* are highly cellular, well demarcated, irregularly shaped and infiltrative. They grow in a tubular-trabecular pattern of densely arranged cells supported by an abundant, extracellular matrix rich stroma. The tumor cells are polygonal, moderately sized, with indistinct margins and a sparse, amphophilic cytoplasm. Their nuclei are round to ovoid, centrally located with finely stippled marginated chromatin and up to three deeply eosinophilic nucleoli. Mild anisocytosis and anisokaryosis can be observed with up to 20 mitotic figures per high power filed, occasional apoptosis and pronounced invasion of the stroma. The *p27*-deficient tumors are highly cellular, well demarcated, papillary or irregularly shaped. They grow in a tubular-papillary pattern of densely arranged cells. Tumor cells are columnar to polygonal, moderately sized, with a moderate amount of granular, amphophilic cytoplasm. The nuclei are round to ovoid, eccentric or paracentral with marginated chromatin and up to four nucleoli. Moderate anisocytosis and anisokaryosis is present as well as up to eight mitotic figures per high power field. Invasion of the stroma or underlying connective tissue occurs. These results further confirm that the heterozygous or homozygous deletion of the tumor suppressor genes *Cdkn2a* or *p27*, both of which are involved in cell cycle checkpoints (Sherr, 2004), can enable extrahepatic bile duct tumor formation in a mutant *Kras* background, while expression of mutant $Kras^{G12D}$ alone is not sufficient for tumor formation in the CBD (Figure 4-8).

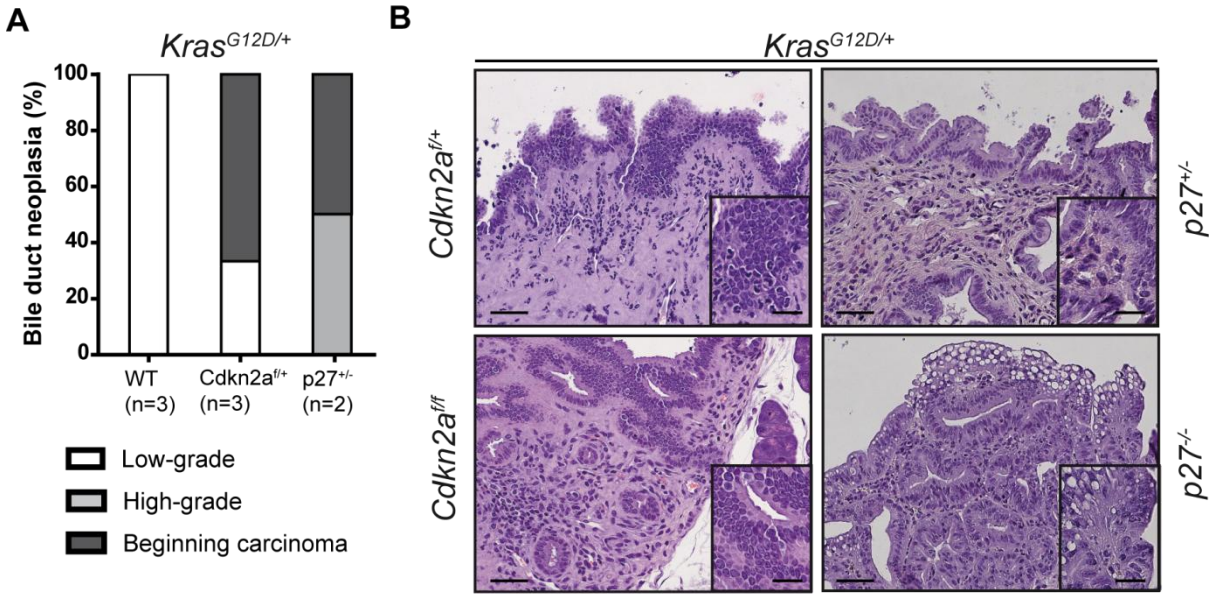

Figure 4-13: Loss of cell cycle regulators enables extrahepatic bile duct tumor formation in a *Kras^{G12D}* background.

A: Histological analysis of bile duct tissue from 3-month-old *Pdx1-Cre;Kras$^{G12D/+}$*, *Pdx1-Cre;Kras$^{G12D/+}$;Cdkn2a$^{f/+}$*, and *Pdx1-Cre;Kras$^{G12D/+}$;p27$^{+/-}$* mice. Low-grade and high-grade neoplasia correspond to BilIN-1/2 and BilIN-3 respectively. All mice displayed only mild changes in the pancreas. **B:** Representative H&E stainings of extrahepatic bile duct carcinomas from *Pdx1-Cre;Kras$^{G12D/+}$;Cdkn2a$^{f/+}$*, *Pdx1-Cre;Kras$^{G12D/+}$;Cdkn2a$^{f/f}$*, *Pdx1-Cre;Kras$^{G12D/+}$;p27$^{+/-}$*, and *Pdx1-Cre;Kras$^{G12D/+}$;p27$^{-/-}$* mice. Scale bars represent 50 µm in main pictures and 20 µm in inserts.

In contrast to the expression of mutant Kras^{G12D} in the extrahepatic bile duct, the expression of mutant p110α ^{H1047R} alone was sufficient for tumor induction and progression in the CBD of mice. From a therapeutic point of view, it is crucial to understand if inhibition of p110α in a developing or more importantly established tumor in the CBD can revert carcinogenesis. Besides application of molecular inhibitors, it is possible in GEMMs to genetically disrupt signaling molecules. For this purpose, part of this work was the generation of a mouse model that enables activation of oncogenic p110α and its inactivation at a later time point.

4.2.5 Generation and characterization of a new mouse line for Flp-dependent activation of the *PIK3CA* mutation

The group of Prof. Dr. Dieter Saur has generated a next generation dual-recombination system which enables modeling of human disease in GEMMs at a new level of complexity (Schönhuber et al., 2014). By crossing of a *Pdx1-Flp* mouse line with a Flp responsive *FSF-Kras^{G12D}* mouse line, they could phenocopy the established Cre-dependent *Pdx1-Cre;Kras^{G12D}* model (Hingorani et al., 2003). The great advantage of using the Flp-frt system for tumor initiation is the fact that the commonly used Cre-loxP system with a huge repository of different Cre lines and floxed or LSL-silenced alleles can be used for secondary genetic manipulation. This secondary manipulation can for example occur in a different cell type or at a later time point.

According to the *FSF-Kras^{G12D}* mouse line, a *FSF-PIK3CA^{H1047R}* mouse line has been generated in this work (Figure 4-14-A) in order to generate *Pdx1-Flp;FSF-PIK3CA^{H1047R}* mice as tumor initiating step. The expression of the constitutive active mutant p110α^{H1047R} is silenced by a stop cassette composed of a neomycin resistance gene, three consecutive *SV40* derived pA signals, and an RNA polymerase pausing element and can be excised by Flp mediated recombination of the frt sites. In addition, it should be possible to switch off the expression of mutant p110α at a later time point in order to mimic therapeutic targeting of p110α. This will be achieved through application of a third site-specific recombinase called Dre which recognizes so called rox sites. The Dre recombinase has been identified by Sauer and McDermott and shows a similar efficiency compared with Cre thus being superior to the Flp recombinase (Sauer and McDermott, 2004; Anastassiadis et al., 2009). Cloning of a tamoxifen inducible *Dre-ERT2* mouse line is still in progress and will be used to induce disruption of mutant *PIK3CA* via tamoxifen application. For this purpose, the whole frt-stop-frt-PIK3CA^{H1047R} expression cassette is flanked by two rox sites (Figure 4-14-A). The rox-frt-stop-frt-PIK3CA^{H1047R}-rox expression cassette was targeted as a knock-in to the *Rosa26* gene locus via homologous recombination. The cloning strategy is described in chapter 3.1.1.3.

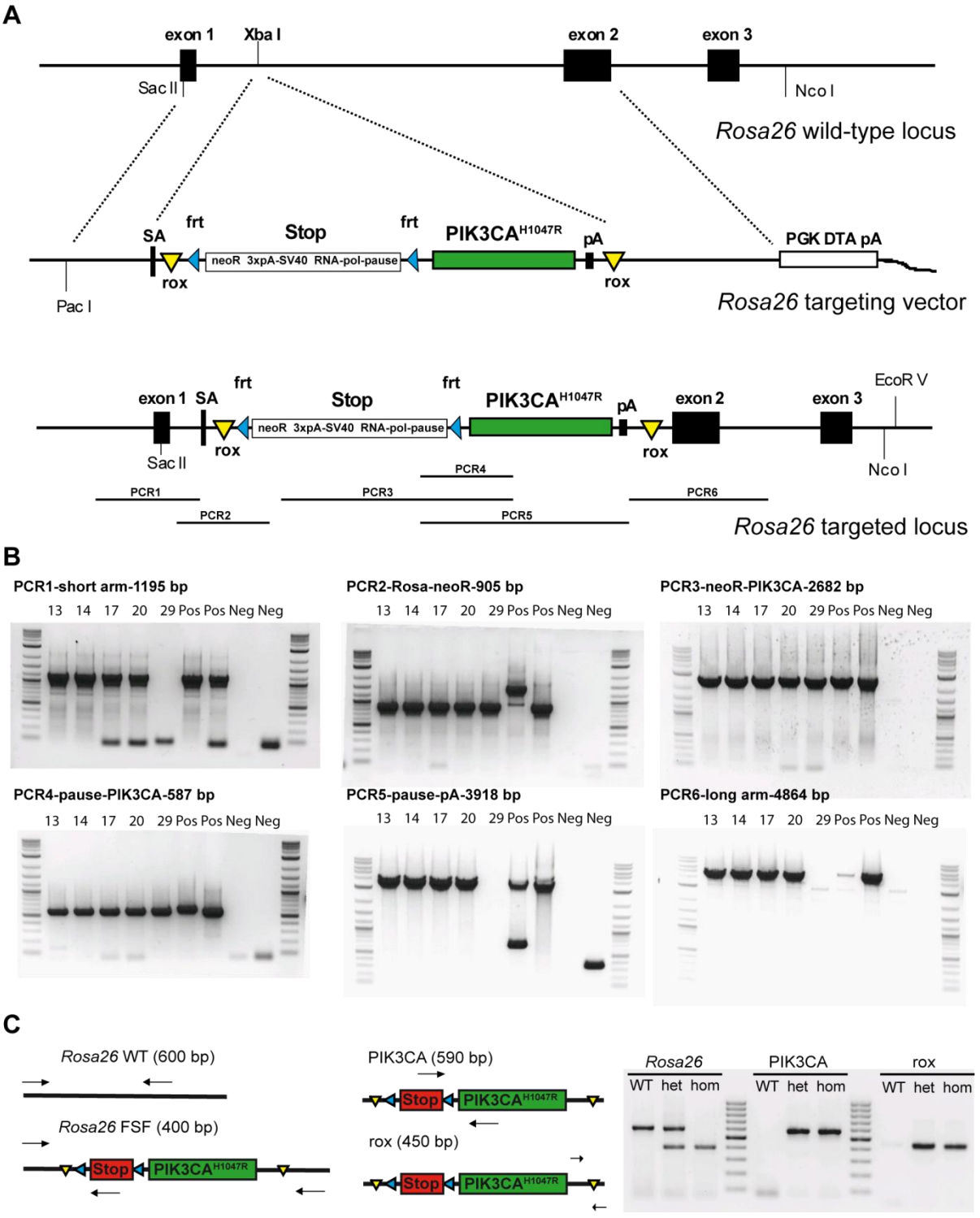

Figure 4-14: Targeting of a rox-frt-stop-frt-PIK3CA$^{H1047R/+}$-rox expression cassette to the murine *Rosa26* locus.

A: From top to bottom, diagrams of: *Rosa26* wild-type locus; the *Rosa26* targeting vector containing the frt-stop-frt silenced *PIK3CA^{H1047R}* expression cassette flanked by rox sites; the targeted *Rosa26* locus. Restriction sites and location of PCRs covering the whole construct are indicated. **B:** PCR analysis of 5 different ES cell clones (13, 14, 17, 20, and 29) for confirmation of correct homologous recombination and complete integration of the expression cassette. Two similar *Rosa26* targeting vectors served as positive controls. Variations in PCR product sizes are possible due to differing elements in those vectors, such as additional promoter sequences. Negative controls were DNA from wild-type ES cells and DNA free reactions. ES cell clones 14 and 17 were selected for blastocyst injection. **C:** Schemes of PCR primer binding sites for the detection of the *FSF-PIK3CA$^{H1047R/+}$* allele and PCR analysis of tail DNA from wild type (WT), heterozygous (het), and homozygous (hom) *FSF-PIK3CA^{H1047R}* mice . The „*Rosa26*“ PCR is required to test zygosity of the knock-in, „PIK3CA“ and „rox“ PCRs specifically show presence of the *PIK3CA^{H1047R}* cassette and the terminal rox site respectively.

The final construct was shuttled into W4/129S6 ES cells through electroporation. Geneticin® treatment of ES cells was used to select for positive clones expressing the neomycin resistance gene. As the stop cassette did not carry any promoter upstream of the resistance gene, only integration of the construct downstream of an endogenous promoter enabled expression of the neomycin resistance gene. In addition, cells with random integration of the targeting construct died due to expression of the diphtheria toxin A (DTA) gene under control of the *phosphoglycerate kinase (PGK)* promoter as a negative selection mechanism. 30 Geneticin®-resistant ES cell clones were picked and analyzed by PCR screen for integration in the *Rosa26* locus. Five clones were further analyzed by six PCRs spanning the whole construct and the upstream and downstream integration sites (Figure 4-14-B). Clones 13, 14, 17, and 20 proved to be correct according to the PCR analysis and two clones (14 and 17) were sent to the PolyGene AG (Rümlang, Switzerland) for blastocyst injection and generation of germline chimeras. Two highly chimeric males were bred with *C57BL/6J* females to obtain heterozygous *FSF-PIK3CA*$^{H1047R/+}$ mutant offspring on a mixed *129S6;C57BL/6J* genetic background. Both of them transmitted the knock-in allele to the progeny and both heterozygous and homozygous mice were viable and did not show any phenotype. Three PCRs are regularly performed on tail DNA in order to determine the genotype of new offspring (Figure 4-14-C). While the "*Rosa26*" PCR shows the zygosity of mutant alleles in the *Rosa26* gene locus, the "PIK3CA" PCR proves presence of the stop cassette as well as the *PIK3CA* ORF and the "rox" PCR detects the pA sequence and the downstream rox site.

The newly generated *FSF-PIK3CA*^{H1047R} mice were crossed with *Pdx1-Flp* mice resulting in *Pdx1-Flp;FSF-PIK3CA*$^{H1047R/+}$ mice. PCR analysis of various tissues from these compound mice revealed recombination in CBD, gallbladder, pancreas and stomach (Figure 4-15-A). The first *Pdx1-Flp;FSF-PIK3CA*$^{H1047R/+}$ mice analyzed show a similar phenotype as the *Pdx1-Cre;LSL-PIK3CA*$^{H1047R/+}$ mice. Figure 4-15-B shows macroscopic pictures of 1- and 6-month-old *Pdx1-Flp;FSF-PIK3CA*$^{H1047R/+}$ mice. The left pictures present the view on the open abdominal cavity with craniodorsally reflected liver lobes (a+d), the other pictures show dissected organs from the same mice. The extrahepatic bile duct of the 1-month-old mouse is slightly dilated to a diameter of 1.5 mm and is transparent while the gallbladder is whitish. The duodenum displays hyperplasia and the pancreas is entirely enlarged, white and slightly more firm. These neoplastic changes are more advanced in the 6-month-old mouse with an elongated and slightly dilated transparent CBD, a transmurally growing spherical adenoma with a diameter of 5 mm in the proximal duodenum and a further enlarged tan pancreas harboring a cyst measuring 5 mm in diameter in the tail region.

Histological analysis of the different tissues from these mice is shown in Figure 4-15-C. The CBD epithelium from the 1-month-old mouse (a) is papillary, well-demarcated and shows a

tubular, densely packed arrangement. The cells are columnar, moderately sized with indistinct margins and an increased amount of granular, amphophilic cytoplasm. Their nuclei are round to ovoid with variable localization resulting in pseudostratification and finely stippled, marginated chromatin containing up to four nucleoli. There is moderate anisocytosis and anisokaryosis with up to 28 mitotic figures per high power field in the most rapidly growing area. The pancreas of this mouse (b) appeared mostly normal with only one acinar-to-ductal metaplasia (ADM) showing a tubular arrangement of cuboidal cells smaller than acinar cells. The cells have a moderate amount of granular, amphophilic cytoplasm with distinct margins. The nuclei are round to ovoid, central or paracentral with finely stippled, marginated chromatin and one to three nucleoli. An aberrant region in the liver was found adjacent to normal tissue in a 1-month-old *Pdx1-Flp;FSF-PIK3CA*$^{H1047R/+}$ mouse (c). The large, polygonal cells show an abundant eosinophilic, granulated cytoplasm with indistinct margins and multiple small vacuoles. The nuclei are round, centrally located with dense chromatin and more than five deeply eosinophilic nucleoli. Moderate anisokaryosis with some giant nuclei is present. Neoplastic changes in the 6-month-old mouse are generally more severe. The bile duct epithelium is papillary and occasionally poorly demarcated and infiltrative (d). The cells show a tubular and densely packed arrangement and are columnar to polygonal, moderately sized with a moderate amount of granular, amphophilic cytoplasm with indistinct margins. Their nuclei are round to ovoid, basal or paracentral with finely stippled, marginated chromatin and up to three nucleoli. Moderate anisokaryosis with up to ten mitotic figures per high power field and marked anisocytosis can be observed. There is occasional invasion into the connective tissue. Pancreas histology reveals the presence of ADMs and low-grade pancreatic intraepithelial neoplasia (PanINs) as well as an increased amount of stroma (e). The neoplastic cells are cuboidal or columnar and smaller than acinar cells with a sparse to moderate amount of amphophilic cytoplasm and distinct margins. The nuclei are round to ovoid, mostly basally located with marginated chromatin and up to four nucleoli. As already seen macroscopically, there is an adenoma in the proximal duodenum showing elongated villi with increased density (f). The tumor cells grow in a serrated pattern with densely packed cells. The cells are cuboidal to columnar with a moderate amount of granular, amphophilic cytoplasm and indistinct margins. Their nuclei are round to ovoid, basal or paracentral with sparse marginated chromatin and large deeply eosinophilic nucleoli. Moderate anisokaryosis and occasional apoptosis are present. These preliminary results indicate that the newly generated *FSF-PIK3CA*^{H1047R} allele is functional and able to induce pathological changes in CBD, gallbladder, pancreas, liver and duodenum when crossed with the *Pdx1-Flp* line. Thus, *Pdx1-Flp;FSF-PIK3CA*$^{H1047R/+}$ mice nicely recapitulate the phenotype of *Pdx1-Cre;LSL-PIK3CA*$^{H1047R/+}$ mice and can be used for further genetic manipulation using Cre and Dre recombinases.

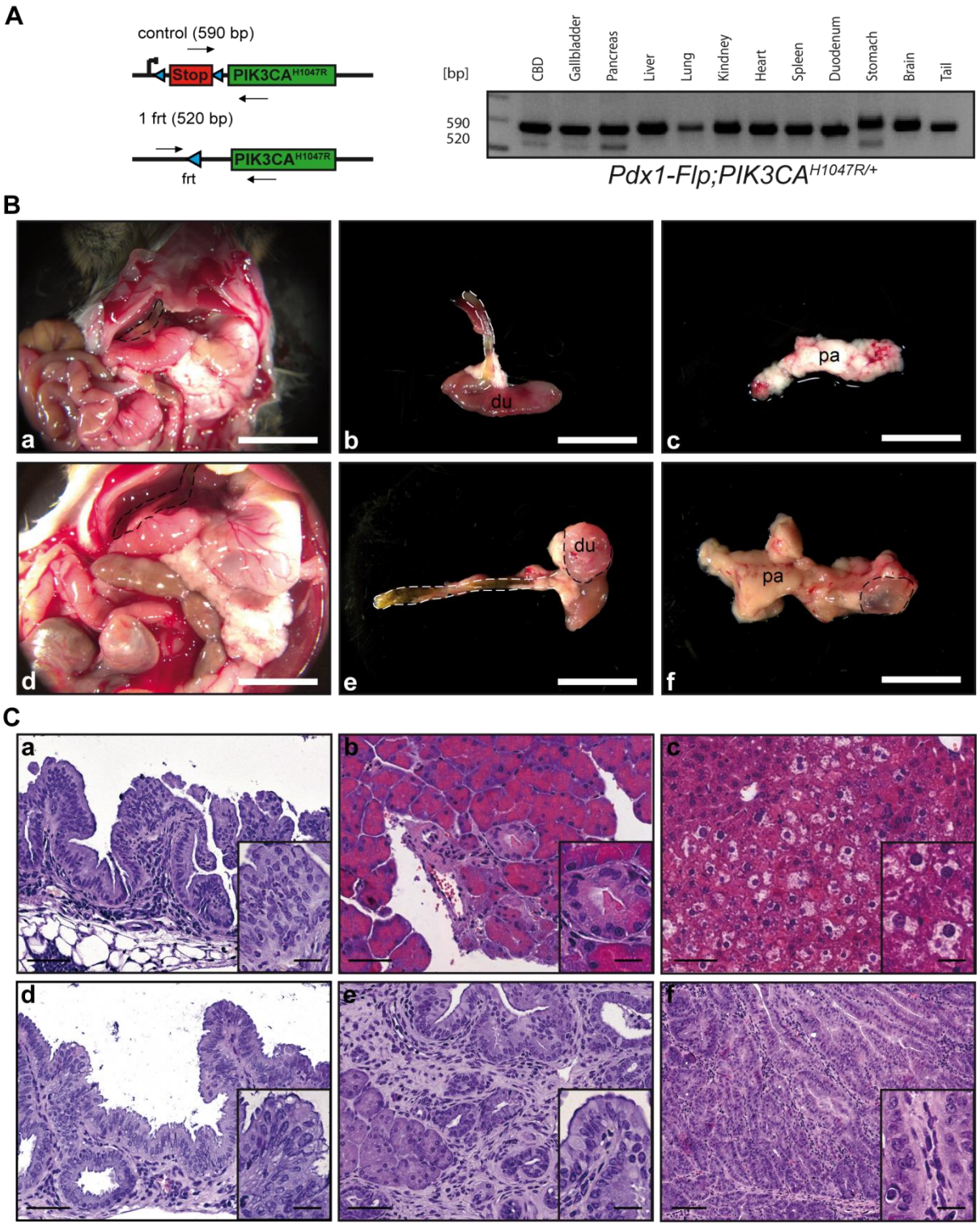

Figure 4-15: *Pdx1-Flp* dependent PI3K pathway activation recapitulates the *Pdx1-Cre;LSL-PIK3CA*$^{H1047R/+}$ mouse model.

A: Recombination scheme of the *FSF-PIK3CA*$^{H1047R/+}$ allele including primers for PCR analysis and PCR analysis of DNA from different tissues of a *Pdx1-Flp;FSF-PIK3CA*$^{H1047R/+}$ mouse after Flp-mediated recombination. **B:** Macroscopic pictures from *Pdx1-Flp;FSF-PIK3CA*$^{H1047R/+}$ mice at the age of 1 month (a-c) and 6 months (d-f). The extrahepatic bile ducts are demarcated by dashed lines (a+d black, b+e white). An adenoma in the duodenum (du) is shown in panel e. Pancreata (pa) are shown in panel c+f, a pancreatic cyst is demarcated in panel f. Scale bars represent 1 cm. **C:** H&E stainings from *Pdx1-Flp;FSF-PIK3CA*$^{H1047R/+}$ mice at the age of 1 month (a-c) and 6 months (d-f). Examples of extrahepatic bile ducts (a+d), pancreata (b+e), as well as fatty changes in the liver (c) and an adenoma of the duodenum (f) are depicted. Scale bars represent 50 µm in panels a-e, 100 µm in panel f and 20 µm in all inserts.

5 Discussion

Liver cancer is a fatal disease being the second most common cause of cancer related deaths worldwide (Steward and Wild, 2014). The majority of primary liver cancers are HCCs but intrahepatic CCCs, although relatively rare, should be considered as well due to their very poor outcome with a 5-year survival below 5% (Weledji et al., 2014; Shaib and El-Serag, 2004). The related extrahepatic CCC is a rare disease as well with limited diagnosis and treatment options and a 5-year survival of 15-20% (Shaib and El-Serag, 2004; Chung et al., 2009). Deciphering the molecular pathways underlying these diseases and their accessibility for drug treatment is crucial for improving the treatment of HCC and CCC patients. GEMMs are a valuable tool for modeling the human disease as the expression of candidate human oncogenes in transgenic mice can trigger tumorigenesis and deletion of candidate human tumor suppressor genes in mice can increase cancer susceptibility thereby validating the role of these genes for tumorigenesis (Rangarajan and Weinberg, 2003). This work focuses on the investigation of the role mutant p110α in HCC and CCC as the PI3K-AKT-mTOR pathway is frequently overactivated in these cancers (Sahin et al., 2004; Boyault et al., 2007; Simbolo et al., 2014; Riener et al., 2008; Chung et al., 2009).

5.1 A new model for hepatic steatosis, NASH and liver cancer

This work presents the first GEMM overexpressing mutant p110α^{H1047R} specifically in the liver. The use of the *Alb-Cre* line enables liver mutagenesis already during embryonic development in the hepatoblast stage thus targeting developing hepatocytes and cholangiocytes (Gualdi et al., 1996; Postic et al., 1999; Postic and Magnuson, 2000). Although PCR analysis of various tissues from an 1-month-old *Alb-Cre;PIK3CA*$^{H10470R/+}$ mouse revealed that Cre mediated recombination of the *LSL-PIK3CA*^{H1047R} allele occurred exclusively in the liver, this recombination was not complete. An efficiency of only 40% immediately after birth increasing to 90% in mice older than 6 weeks of age has been reported (Postic and Magnuson, 2000). While mature hepatocytes retain albumin expression and therefore albumin promoter activation, the albumin promoter is not stimulated in mature biliary cells (Brill et al., 2002). This means that after aging of the mice most likely the great majority of hepatocytes has undergone Cre-mediated recombination while only a fraction of cholangiocytes which are directly derived from hepatoblasts with Cre activity would express the mutant p110α.

The most obvious phenotype of *Alb-Cre;PIK3CA*$^{H10470R/+}$ mice was their massive increase in liver size and the pale appearance of the liver. A more than two-fold increased liver to body weight ratio was already prominent at an age of 1 month and rose further with aging. This

hepatomegaly and pale coloring of the liver was equally observed in *Alb-Cre;Pten*$^{f/f}$ mice, which share the overactivation of the PI3K-AKT-mTOR signaling pathway through inference with the balance between phosphatidylinositol-4,5-bisphosphate (PIP2) and PIP3 (Horie et al., 2004; Stiles et al., 2004). In contrast, *Alb-Cre;PIK3CA*$^{f/f}$ mice, which lack p110α in the liver, displayed a liver weight loss of approximately 20% and mice lacking the insulin receptor (IR) in the liver (*Alb-Cre;IR*$^{f/f}$) presented with livers slightly darker and 40% smaller compared to controls (Sopasakis et al., 2010; Michael et al., 2000). In addition, AKT2 deficiency combined with liver specific *Pten* knock-out could reduce hepatomegaly compared to *Alb-Cre;Pten*$^{f/f}$ mice (He et al., 2010). These data indicate an important role of IR and PI3K-AKT signaling in the regulation of liver size.

Histology of the livers from *Alb-Cre;PIK3CA*$^{H10470R/+}$ mice uncovered that the increased liver size and pale appearance resulted from an extensive lipid deposition inside the hepatocytes. This steatosis was both macrovesicular and microvesicular and resulted in disturbance of the liver zonation already at an age of 3 months. More severe steatosis and mild immune cell infiltration was observed at 6 months of age indicating the progression to steatohepatitis. The nature and amount of immune cells has not been analyzed yet. A very similar histopathology was present in the livers from *Alb-Cre;Pten*$^{f/f}$ mice. Horie and coworkers reported lipid accumulation around the central vein area at 10 weeks of age and steatohepatitis at an age of 40 weeks (Horie et al., 2004). In accordance with that, Stiles and colleagues observed mild lipid deposition followed by substantial lipid accumulation in 1- and 3-month-old mice respectively, and additional inflammation and mild fibrosis in 6-month-old mice (Stiles et al., 2004). Steatosis and steatohepatitis are the typical hepatic manifestation of the metabolic syndrome in humans and are designated NAFLD and NASH respectively (Takahashi et al., 2012). In theory, four different causes can lead to a metabolic imbalance resulting in hepatic steatosis (Takahashi et al., 2012). First, the uptake of long-chain fatty acids can be increased. Second, *de novo* long-chain fatty acid and triglyceride synthesis in the liver can be increased. Third, lipid export as lipoproteins or triglycerides can be impaired. Last, long-chain-fatty acid metabolism via mitochondrial β-oxidation can be decreased. Data from *Alb-Cre;Pten*$^{f/f}$ mice suggest that the hepatic lipid synthesis is elevated to a non-physiological level. This is supported by induction of the regulatory molecules peroxisome proliferator-activated receptor (PPAR) γ and sterol regulatory element-binding protein-1c (SREBP-1c) as well as lipogenic enzymes such as fatty acid synthetase, acetyl-CoA carboxylase, and stearyl-CoA desaturase combined with a downregulation of gluconeogenic enzymes such as glucose-6-phosphatase and phosphoenolpyruvate carboxykinase (Horie et al., 2004; Stiles et al., 2004; Kenerson et al., 2013). Contrary, lipogenic genes were found to be down-regulated in livers of *Alb-Cre;PIK3CA*$^{f/f}$ mice (Sopasakis et al., 2010). Furthermore, *AKT2* knock-out mice show more than 2-fold decreased liver triglyceride levels and a reduction in the

expression of lipogenic enzymes (He et al., 2010). It can be concluded that active signaling through p110α and AKT stimulates hepatic lipid synthesis.

p110α has been shown to be the major PI3K catalytic subunit involved in hepatic insulin signaling (Sopasakis et al., 2010) and it can therefore be assumed that expression of mutant p110α and in a very similar way deletion of PTEN constantly activates signaling downstream of the insulin receptor. An increased glucose tolerance and increased insulin sensitivity observed in *Alb-Cre;Pten*$^{f/f}$ mice suggests that livers with constitutive PI3K signaling are highly efficient in glucose uptake from the blood (Stiles et al., 2004). In addition, fasting glucose levels were decreased in *Alb-Cre;Pten*$^{f/f}$ mice compared to control mice at an age of 1 and 3 months, indicating that glucose uptake by the liver might be high even at fasting conditions depriving peripheral organs from energy supply (Stiles et al., 2004). This lack of energy in other organs resulted in a 50% reduction in total body fat content in 1-month-old *Alb-Cre;Pten*$^{f/f}$ mice and the fact that the liver to body weight ratio in *Alb-Cre;PIK3CA*$^{H10470R/+}$ mice increased while the total body weight remained normal equally suggests a redistribution of body fat (Stiles et al., 2004). A similar phenotype could be observed in *protein tyrosine phosphatase-1B* null mice (Klaman et al., 2000). These mice, which lack an important negative regulator of IR signaling, showed low body fat stores as well as increased glucose tolerance and insulin sensitivity that could be explained by a 75% increased glucose uptake into the skeletal muscle. On the other hand, *Alb-Cre;PIK3CA*$^{f/f}$ mice developed mild adult-onset obesity (Sopasakis et al., 2010).

The link between constitutive insulin signaling and steatosis is the fact that fatty acid synthesis in the liver can be stimulated by insulin in order to convert excess glucose to fatty acids for storage (Goldstein et al., 2006). Insulin selectively up-regulates the expression of the SREBP isoform SREBP-1c, which acts as transcription factor to activate genes involved in fatty acid synthesis, in rat livers and primary hepatocytes and this activation can be abolished by PI3K inhibition (Goldstein et al., 2006; Shimomura et al., 1999; Fleischmann and Iynedjian, 2000). Activation of the main PI3K effector AKT *in vitro* (MyrAKT-ER) increased SREBP-1 mRNA and SREBP-1 processing without affecting SREBP-2. As a consequence, a large number of genes encoding for enzymes of sterol or fatty acid synthesis were transcriptionally up-regulated and the cells displayed accumulation of lipids after 48 h of AKT activation (Porstmann et al., 2005). In contrast, SREBP-1c expression was considerably reduced in *AKT2*$^{-/-}$ mice as well as *Alb-Cre;Pten*$^{f/f}$*;AKT2*$^{-/-}$ mice (He et al., 2010). It can be hypothesized that expression of mutant p110α specifically in the liver mimics constant insulin signaling resulting in high glucose uptake and metabolism as well as induction of lipogenesis.

Stiles and coworkers could show for *Alb-Cre;Pten*$^{f/f}$ mice that besides lipid synthesis, lipid secretion was increased assessed by measuring triglyceride levels in the blood of mice that

got injected with a detergent (Stiles et al., 2004). Triglycerides progressively increased in the blood as the detergent inhibited peripheral absorption, but the triglyceride concentration without detergent treatment was similar to controls. Analysis of the serum from *Alb-Cre;PIK3CA*$^{H10470R/+}$ mice showed minor differences in the triglyceride concentration compared to control mice at an age of 3 months. There were no significant differences between mutant *PIK3CA* and control mice at later time points, but high fluctuations in both groups that could possibly be attributed to different feeding states. In accordance with the data obtained from *Alb-Cre;Pten*$^{f/f}$ mice, it is possible that lipid secretion from the liver is increased, but that those lipids are quickly absorbed in the peripheral organs, which most likely obtain only minor amounts of glucose. In contrast to the triglyceride concentration, the concentration of cholesterol in the serum was 3-fold increased in young as well as older *Alb-Cre;PIK3CA*$^{H10470R/+}$ mice monitored up to an age of 11 months. A tendency for increased serum cholesterol concentrations has been observed in *Alb-Cre;Pten*$^{f/f}$ mice as well (Horie et al., 2004). In accordance with these findings, acute liver *PIK3CA* knock-out resulted in a 28% reduction in serum cholesterol (Sopasakis et al., 2010). In addition, serum triglyceride concentrations were reduced by 44% in this model further supporting the assumption that PI3K-AKT-mTOR pathway activation in the liver stimulates triglyceride secretion (Sopasakis et al., 2010). Increased serum cholesterol and triglyceride concentrations can also be seen in patients with metabolic syndrome and liver steatosis (Palmieri et al., 2006).

Alb-Cre;Pten$^{f/f}$ mice have not only been described as liver cancer model but also as an animal model for NAFLD and NASH. Especially, the reproduction of human histopathology and the spontaneous progression from steatosis to steatohepatitis and fibrosis distinguish this model from many other models (Takahashi et al., 2012). The main disadvantage of *Alb-Cre;Pten*$^{f/f}$ mice in modeling NAFLD is the fact that these mice do not combine all features of the metabolic syndrome. The reduced amount of adipose tissue and the insulin hypersensitivity observed in this model represent the opposite effects of obesity and diabetes (Stiles et al., 2004). The whole spectrum of the metabolic syndrome is better reflected in other animal models of NAFLD including ob/ob, Db/Db and KK-A$^{\gamma}$ mice, which all function through impaired appetite suppression. In contrast to *Alb-Cre;Pten*$^{f/f}$ mice, spontaneous progression to steatohepatitis does not occur in these mice (Takahashi et al., 2012). As the *Alb-Cre;PIK3CA*$^{H10470R/+}$ mice investigated in this work share many characteristics of liver specific *PTEN* knock-out mice, they might classify as well as a model reflecting the liver manifestation of human metabolic syndrome but not the whole spectrum of systemic symptoms.

Massive hepatic steatosis impairs the normal liver functions and provokes oxidative stress, hepatocyte injury, hepatotoxicity by free fatty acids and abnormal cholesterol loading in the

liver altogether triggering an inflammatory response (Takahashi et al., 2012). Liver injury can be assessed non-invasively by quantification of liver enzymes in the blood. Serum concentrations of the amino transferases aspartate amino transferase and alanine amino transferase as well as alkaline phosphatase have been analyzed here. Increases in amino transferase levels are mostly due to hepatocyte injury caused for example by chronic hepatitis virus infection or hepatic steatosis (Giannini et al., 2005; Pratt and Kaplan, 2000). Palmieri and coworkers reported a more than doubled alanine amino transferase concentration in patients with metabolic syndrome compared to healthy controls (Palmieri et al., 2006). The concentration of this enzyme was up to 15-fold increased in the serum of *Alb-Cre;PIK3CA*$^{H10470R/+}$ mice, suggesting a severe hepatocyte damage. Aspartate amino transferase concentrations were highly fluctuating in these mice and only displayed a significant increase compared to controls in mice older than 6 months. Both amino transferase concentrations were significantly elevated *Alb-Cre;Pten*$^{f/f}$ mice (Horie et al., 2004; Galicia et al., 2010). Furthermore, a diet induced NAFLD model that is based on a methionine and choline deficient diet equally presented increased serum alanine amino transferase concentrations (Dela Peña et al., 2005). Alkaline phosphatase concentrations were more than 2-fold elevated in *Alb-Cre;PIK3CA*$^{H10470R/+}$ mice at different time points. Increased serum concentrations of this enzyme can originate predominantly from liver or bone. If alkaline phosphatase concentrations are elevated in combination with 5'-nucleotidase and γ-glutamyl transferase, a cholestatic disease is indicated (Giannini et al., 2005; Pratt and Kaplan, 2000). Although concentrations of 5'-nucleotidase and γ-glutamyl transferase have not been analyzed in *Alb-Cre;PIK3CA*$^{H10470R/+}$ mice, the liver specific mutagenesis and the fact that mutant p110α can be expressed in cholangiocytes in this model suggest that the mice suffer from cholestatic damage as well. 40-weeks-old *Alb-Cre;Pten*$^{f/f}$ mice equally showed significant elevations in serum alkaline phosphatase concentrations (Horie et al., 2004). Altogether, the presence of liberated liver enzymes in the blood as well as the loss of liver zonation in *Alb-Cre;PIK3CA*$^{H10470R/+}$ mice indicates that normal liver function is severely impaired. This could in part contribute to the fluctuating health condition and sudden death in 3- to 6-month-old mice. Neurologic damage in chronic liver disease has been reported in humans, is linked to decreased hepatic function in detoxification of ammonia and could be responsible for the reduced vitality in *Alb-Cre;PIK3CA*$^{H10470R/+}$ mice (Tapper et al., 2015). A further explanation for occasional periods of apathy observed in *Alb-Cre;PIK3CA*$^{H10470R/+}$ mice could be hypoglycemia at fasting conditions as observed in 1- and 3-months old *Alb-Cre;Pten*$^{f/f}$ mice (Stiles et al., 2004). This is supported by the fact that feeding of oatmeal and glucose improves the activity of *Alb-Cre;PIK3CA*$^{H10470R/+}$ mice (non-quantified observation). Interestingly, 6-month-old *Alb-Cre;Pten*$^{f/f}$ mice showed fasting glucose levels comparable to controls arguing for a certain

adaptation mechanism (Stiles et al., 2004). Our data on the survival of *Alb-Cre;PIK3CA*$^{H10470R/+}$ mice accordingly show that mice that did not die until an age of 200 days further survived to an age of 300 to 400 days, then presenting with a huge tumor burden.

Hepatic steatosis is a major risk factor for developing chronic liver disease and liver tumors especially in Western countries (Sanyal et al., 2010). The metabolic syndrome is despite a low relative risk for HCC development responsible for 20-30% of HCC cases in the US (El-Serag and Kanwal, 2014). Following a long period of steatosis and steatohepatitis, *Alb-Cre;PIK3CA*$^{H10470R/+}$ mice develop liver tumors starting from an age of approximately 145 days. Mice reaching an age of more than 196 days show liver tumors with complete penetrance and usually present with several tumor nodules. Although steatosis is mainly associated with HCC formation, both HCCs and CCCs could be observed in *Alb-Cre;PIK3CA*$^{H10470R/+}$ mice even within one animal. About 10% of human CCC cases are preceded by a state of chronic inflammation as well, and the elevated alkaline phosphatase levels already at an age of 3 months indicate that the ductal compartment is severely damaged in *Alb-Cre;PIK3CA*$^{H10470R/+}$ mice (Shaib and El-Serag, 2004). Thus, a strong environmental predisposition for the development of both HCC and CCC is given in the *Alb-Cre;PIK3CA*$^{H10470R/+}$ model. Furthermore, the expression of mutant p110α is expected in hepatocytes as well as intrahepatic cholangiocytes due to *Alb-Cre* activity in progenitor cells. Several studies investigating liver tumorigenesis in *Alb-Cre;Pten*$^{f/f}$ mice have been reported with contradictory results concerning the presence of HCC and CCC formation. The first publication by Horie and coworkers demonstrated HCC formation only with a relatively high incidence of 67% at an age of 74-78 weeks (Horie et al., 2004). Subsequent studies comparing *Alb-Cre;Pten*$^{f/f}$ mice to other genotypes all reported liver tumor formation around an age of one year and an incidence of 40-90% with presence of both HCCs and CCCs plus mixed or bi-lineage tumors (Xu et al., 2006; Kenerson et al., 2013; Morris et al., 2014; Galicia et al., 2010). Differences in tumor incidence and tumor type distribution are most likely attributable to differences in the background strains. Most studies used a mixed *C57Bl/6;129* background (Horie et al., 2004; Morris et al., 2014; Galicia et al., 2010) while the study with the lowest general tumor incidence was performed in a *129;FVB;BALBc;Black Swiss* background (Xu et al., 2006). Xu and colleagues specifically investigated the role of the background strain and could increase the HCC incidence from 33% in the *129;FVB;BALBc;Black Swiss* background to 91% in a *C57Bl/6;129* background (Xu et al., 2006). Differences in the susceptibility of different mouse strains to hepatocarcinogenesis have been reported but *C57Bl/6*, *129* and *BALBc* strains share a low incidence of spontaneous hepatocellular neoplasia formation (Buchmann et al., 1991; Maronpot, 2009). The *Alb-Cre;PIK3CA*$^{H10470R/+}$ mice described in this work were bred on a mixed *C57Bl/6*;*129S6/SvEv* genetic background.

Two mechanisms concerning the origin of HCCs and CCCs in *Alb-Cre;PIK3CA*$^{H10470R/+}$ mice are possible. On the one hand, mature hepatocytes or cholangiocytes expressing mutant p110α can transform after acquisition of additional mutations and give rise to HCCs or CCCs respectively. On the other hand, bipotent progenitor cells which equally express mutant p110α could cause HCCs, CCCs and mixed tumors. Interestingly, the expansion of a CD133^{+} CD45^{-} non-parenchymal lineage has been observed in premalignant livers from *Alb-Cre;Pten*$^{f/f}$ mice (Rountree et al., 2009). These cells turned out to maintain a bipotent phenotype after cultivation *in vitro*, were tumorigenic when injected into nude mice and were suggested to represent a bipotent progenitor cell population with cancer stem cell characteristics. The expansion of this lineage could either result from transformation of progenitor cells due to the activation of PI3K-AKT-mTOR signaling or be caused by the liver injury that occurs already in young *Alb-Cre;Pten*$^{f/f}$ mice. The fact that the same type of bipotential cells equally expands in the PTEN/PI3K independent *methionine adenosyltransferase 1A*-deficient steatosis model argues for an injury induced phenotype (Rountree et al., 2008). Furthermore, Kenerson and coworkers characterized a fraction of CCCs in *Alb-Cre;Pten*$^{f/f}$ mice, that were not derived from cells with targeted *PTEN* deletion but rather developed from reactive proliferation of *PTEN* wild type cells (Kenerson et al., 2013). In contrast, it could be demonstrated that tumorigenesis in a *PTEN*-deficient liver is possible in the absence of steatosis. This was achieved in *Alb-Cre;Pten*$^{f/f}$*;AKT2*$^{-/-}$ mice, which do not develop early onset steatosis but develop tumors composed of hepatocytes, cholangiocytes and bi-lineage cells with a latency of 6 months compared to *Alb-Cre;Pten*$^{f/f}$ mice (Galicia et al., 2010). The study further suggests that tumors start to develop in *Alb-Cre;Pten*$^{f/f}$ mice around an age of 9 months when massive hepatocyte apoptosis coincided with strong proliferation of progenitor cells and expansion of the ductal lineage. The same expansion of progenitors and cholangiocytes can be induced in *Alb-Cre;Pten*$^{f/f}$*;AKT2*$^{-/-}$ mice through a hepatotoxic diet, showing that transformation of *PTEN*-deficient progenitors is not inhibited by *AKT2* loss but that the stimulus for proliferation of mutant progenitors is mostly lacking. These data provide evidence that cell transformation and environmental stimuli cooperate in tumorigenesis in *Alb-Cre;Pten*$^{f/f}$ mice.

Similar mechanisms most likely account for tumorigenesis in *Alb-Cre;PIK3CA*$^{H1047R/+}$ mice. The expression of mutant p110α could directly influence tumorigenesis through oncogene expression or indirectly by creating a tumor promoting environment. Deletion of the oncogene at a time point when steatosis and liver damage are already established could help to shed light on this question. Next-generation mouse models described later will be crucial for this investigation and up to now, only speculative conclusions are possible. The fact that mutations in *PIK3CA* are in general relatively rare indicate that p110α is not a main driver in HCC formation (Boyault et al., 2007; Tanaka et al., 2006). Only Lee and colleagues

reported a *PIK3CA* mutation frequency of 35.6% in human HCC samples but half of them were not located in the two typical hot spots and it is not known if they harbor any oncogenic activity (Lee et al., 2005). In the end, not only mutations in *PIK3CA* itself but also mutations or aberrant expression of other signaling components contribute to a frequent PI3K-AKT-mTOR pathway activation. As PI3K-AKT-mTOR signaling is often increased in human HCCs and CCCs, there seems to be a role beyond induction of lipid synthesis and creation of a pro-tumorigenic environment. This is supported by the fact that mouse models overactivating PI3K-AKT-mTOR signaling in the liver, e.g. *Alb-Cre;Pten*$^{f/f}$ or *Alb-Cre;PIK3CA*$^{H10470R/+}$, show progression to carcinogenesis while other NAFLD models based on disrupted leptin sensitivity or metabolic dysfunction do not spontaneously develop tumors (Takahashi et al., 2012).

Overall, *Alb-Cre;PIK3CA*$^{H10470R/+}$ mice mostly phenocopy the *Alb-Cre;Pten*$^{f/f}$ mouse model. A more extensive characterization of the new model will probably show more parallels, for example concerning insulin sensitivity or expression of lipogenic enzymes. *Alb-Cre;PIK3CA*$^{H10470R/+}$ mice therefore provide a model for the study of NAFLD, NASH and liver carcinogenesis. Interestingly, a localized steatosis phenotype in the liver has been observed when the same mutant allele was expressed in the *Pdx1-Cre* lineage, thus independently underpinning the role of mutant p110α in inducing focal hepatic steatosis.

5.2 The first genetically engineered mouse model for carcinogenesis in the extrahepatic bile duct gives insight into relevant molecular pathways

Several *Pdx1-Cre* transgenic mouse lines are used mainly in order to target all three lineages of the pancreas and the first *Pdx1-Cre* line was indeed designed for Cre-mediated recombination in the pancreas (Magnuson and Osipovich, 2013; Gannon et al., 2000). Meanwhile, it turned out that ventral pancreas, dorsal pancreas, duodenum, gallbladder, cystic duct and CBD show *Pdx1-Cre* dependent recombination (Spence et al., 2009). This can be explained by the fact that Pdx1 is expressed during embryonic development in precursor cells of the foregut endoderm which further differentiate into pancreas, duodenum, antral stomach, and CBD (Ohlsson et al., 1993; Guz et al., 1995; Offield et al., 1996). It is still expressed in postnatal pancreatic islets, the epithelium lining the duodenal villi, and the CBD including peribiliary glands and mucin producing cells (Ohlsson et al., 1993; Guz et al., 1995; Fukuda et al., 2006). In accordance with these findings, *Pdx1-Cre;R26*^{tdTo} and *Pdx1-Cre;R26*$^{mT/mG}$ reporter mice analyzed in this work proved Cre mediated recombination in pancreas, CBD epithelium, gallbladder, stomach and duodenum. A similar recombination pattern has been described for *Pdx1-Flp* (Schönhuber et al., 2014).

When *Pdx1-Cre* was used to drive expression of p110α^{H1047R}, a broad spectrum of pathological changes involving pancreas, duodenum, liver and extrahepatic biliary tract was observed. Pancreata from *Pdx1-Cre;PIK3CA$^{H1047R/+}$* mice were increased in size with a whitish appearance and displayed histologically ADM, PanIN and PDAC formation. This was expected as *Ptf1a$^{Cre/+}$;PIK3CA$^{H1047R/+}$* mice show pancreatic tumor formation comparable to *Ptf1a$^{Cre/+}$;Kras$^{G12D/+}$* mice, suggesting the PI3K-AKT-mTOR pathway as the main Kras effector pathway in pancreatic carcinogenesis (Eser et al., 2013). Duodenal hyperplasia was frequently observed in *Pdx1-Cre;PIK3CA$^{H1047R/+}$* as well as *Pdx1-Cre;Kras$^{G12D/+}$* mice and correlated with reporter expression in *Pdx1-Cre;R26^{tdTo}* mice. The highest tdTomato expression was visible in the very proximal part of the duodenum and this is the location where approximately 10% of *Pdx1-Cre;PIK3CA$^{H1047R/+}$* mice develop adenomas.

About one fifth of the *Pdx1-Cre;PIK3CA$^{H1047R/+}$* mice presented with fatty changes in the liver that could be seen macroscopically as irregularly shaped, whitish and soft outgrowths. They did not resemble metastasis, frequently occurred locally already before formation of any solid tumors and histologically resembled the steatosis phenotype seen in *Alb-Cre;PIK3CA$^{H1047R/+}$* mice. *R26$^{mT/mG}$* recombination in these altered structures revealed their origin in the Pdx1^{+} lineage. Neither macroscopic fluorescence pictures of *Pdx1-Cre;R26^{tdTo}* mice nor PCR analysis of liver tissue from *Pdx1-Cre;R26$^{mT/mG}$* mice indicated *Pdx1-Cre* activity in the liver. This suggests that the fraction of liver cells targeted by *Pdx1-Cre* is extremely low in the normal liver but can expand when oncogenic p110α ^{H1047R} is expressed. A possible source for Pdx1^{+} cells in the liver resides in peribiliary glands. Peribiliary glands exist in association with bile ducts along the biliary tree from the ampullary region to the large intrahepatic bile ducts and contain multipotent progenitor cells expressing endodermal transcription factors and surface markers but are completely absent in *Pdx1* null mice (Carpino et al., 2012; Fukuda et al., 2006). Subpopulations of peribiliary gland cells exhibit stem cell properties such as nuclear expression of pluripotency genes and a high proliferative capacity *in vitro* while maintaining an undifferentiated state (Wang et al., 2013; Cardinale et al., 2011). They can be differentiated *in vitro* into hepatocyte, cholangiocyte and pancreatic islet lineages under conditions providing appropriate extracellular matrix and soluble components (Cardinale et al., 2011). 30 days after implantation of undifferentiated human peribiliary gland cells into livers of SCID mice, mature human hepatocytes occupied 6.5% of the liver parenchyma and mature human cholangiocytes made up 12.7% of the intrahepatic bile ducts (Cardinale et al., 2011). Besides pluripotency markers, expression of Pdx1, Sox17, insulin, albumin or HepPar1 could be detected in peribiliary glands (Wang et al., 2013; Carpino et al., 2012). In peribiliary glands of the ampullary region, the expression of markers for goblet cells, cholangiocytes and β-islet cells is more prominent than albumin or HepPar1 expression (Carpino et al., 2012). In contrast, peribiliary glands associated with large intrahepatic bile

ducts show a large proportion of HepPar1$^+$ cells but only few cells expressing insulin or Pdx1 (Carpino et al., 2012). Although the fraction of Pdx1$^+$ peribiliary gland cells in the liver is very low, they might have a high proliferative capacity and contribute to hepatocyte and cholangiocyte turnover without major hepatic injury as shown by the implantation experiments. It is therefore possible, that cells with these properties and additionally equipped with an oncogenic mutation can undergo massive proliferation and be responsible for the liver phenotype in *Pdx1-Cre;PIK3CA*$^{H1047R/+}$ mice. The confocal picture of a *Pdx1-Cre;R26*$^{mT/mG}$ bile duct (Figure 4-5) shows co-expression of EGFP, labeling recombined cells, and the ductal marker CK19 in the epithelial layer surrounding the duct lumen while an evagination from the duct as well as a more distal small ductular structure are CK19 negative. These CK19 negative cells could be less differentiated peribiliary gland cells. It has been hypothesized that peribiliary glands can be the origin of intrahepatic and extrahepatic CCCs in human, supported by the finding that the highest density of peribiliary glands is present in the perihilar and ampullary region where extrahepatic CCCs most frequently occur (Cardinale et al., 2010). It cannot be excluded that peribiliary glands contribute to the carcinogenesis in the CBD of *Pdx1-Cre;PIK3CA*$^{H1047R/+}$ mice.

This work represents the first study focusing on targeted mutagenesis in the extrahepatic bile duct. Up to now, no obvious bile duct phenotype has been described for *Pdx1-Cre* dependent models, such as the classical *Pdx1-Cre;Kras*$^{G12D/+}$ model, most likely because the genes analyzed had only a minor effect in the CBD (Hingorani et al., 2003). When *Pdx1-Cre* was used to drive expression of p110α ^{H1047R}, a dilation of the extrahepatic bile duct as well as tumor formation in aged mice could be observed and contrasts the phenotype of *Pdx1-Cre;Kras*$^{G12D/+}$ mice. Nevertheless, both *Pdx1-Cre;Kras*$^{G12D/+}$ and *Pdx1-Cre;PIK3CA*$^{H1047R/+}$ mice developed pancreatic tumors and displayed a similar median survival. The discrepancy concerning tumorigenesis in the CBD is surprising as both mutant Kras and mutant p110α are supposed to activate PI3K-AKT-mTOR signaling. When comparing AKT and GSK3β phosphorylation as an indicator of active PI3K-AKT-mTOR signaling in the pancreata of *Ptf1a*$^{Cre/+}$*;PIK3CA*$^{H1047R/+}$ and *Ptf1a*$^{Cre/+}$*;Kras*$^{G12D/+}$ mice, the phosphorylations appeared slightly weaker in the *Ptf1a*$^{Cre/+}$*;Kras*$^{G12D/+}$ model (Eser et al., 2013). Although using the same Cre-line for the expression of both oncogenes, their respective expression level could differ largely because Kras^{G12D} is expressed from its endogenous locus while p110α^{H1047R} is expressed from the *Rosa26* locus. Therefore, the expression of the oncogenic p110α might be above physiological levels in the *Pdx1-Cre;PIK3CA*$^{H1047R/+}$ model. Interestingly, a study where both Kras^{G12D} and p110α^{H1047R} were expressed from their endogenous loci dependent on the inducible *Pdx1::CreER*^{T2} revealed PanIN formation in the mice expressing mutant Kras but not in mice expressing mutant p110α (Collisson et al., 2012). Furthermore, expression of endogenous levels of mutant Kras^{G12D} or Kras^{G12V} in MEFs results in a

completely different phenotype than ectopic expression of mutant RAS proteins (Guerra et al., 2003; Tuveson et al., 2004). These studies indicate that the expression level of oncogenic proteins has a high impact on the results obtained from GEMMs. The idea that a certain threshold level of p110α activity is required for tumorigenesis is supported by the finding that mice carrying two *PIK3CA*^{H1047R} alleles show a considerably accelerated tumor formation, especially increasing the proportion of CBD cancers at the expense of PDAC formation. It seems that very high levels of PI3K activation are specifically required for extrahepatic bile duct carcinogenesis and that expression of mutant Kras^{G12D} from its endogenous locus is not sufficient to reach these levels. This could be due to the activity of PTEN that has been suggested to function as a brake that inhibits Kras^{G12V} dependent induction of biliary neoplasia in an *AhCreER*^{T}-driven model (Marsh et al., 2013). Using the same Cre-line, *PTEN* knock-out induced multifocal low-grade biliary neoplasia and concomitant expression of mutant Kras and *PTEN* knock-out cooperated in generation of biliary tract abnormalities. A cooperative effect for *PTEN* deletion and *Kras* mutation has equally been described for PDAC formation, whereas *PTEN* knock-out alone gave rise to ADMs only (Ying et al., 2011). Nevertheless, these data do not exclude that *KRAS* mutations can contribute to human CCC formation if expressed at sufficient levels or in combination with other mutations given that 10-47% of human extrahepatic CCCs display *KRAS* mutations (Suto et al., 2000; Deshpande et al., 2011; Simbolo et al., 2014). Thus, molecular differences encountered in bile ducts of *Pdx1-Cre;Kras*$^{G12D/+}$ and *Pdx1-Cre;PIK3CA*$^{H1047R/+}$ mice might not be solely consequential of the mutation in one or the other gene but also depend on their expression levels. Certainly, molecular differences between these models will provide important hints on molecular events required for tumor initiation and progression in the CBD.

The requirements for tumor formation in the pancreas seem to be different as both *Pdx1-Cre;Kras*$^{G12D/+}$ and *Pdx1-Cre;PIK3CA*$^{H1047R/+}$ mice developed PanINs and PDACs. Organ specific differences in the dependency on certain Kras effector pathways have been reported (Eser et al., 2013). Although Kras-driven PDAC formation is dependent on PI3K/PDK1 signaling, the expression level obtained by endogenous expression of mutant Kras seems high enough for tumor induction in the pancreas. Furthermore, CMV-Cre;LSL-Kras$^{G12V\text{-}IRES\text{-}\beta\text{-}geo}$ mice, where the oncogenic Kras is expressed in every tissue at endogenous levels, elucidate that the susceptibility to Kras-induced tumorigenesis is highly variable and might depend on tissue specific transcriptional programs (Guerra et al., 2003). Most tissues tolerated a certain level of mutant Kras expression without any histological alterations.

Although tumor formation did not occur in the CBD of *Pdx1-Cre;Kras*$^{G12D/+}$ mice, the epithelium did not appear completely normal. Low grade neoplasia corresponding to BilIN-1

and -2 could be observed in these mice, but even at an age of 12 to 16 months no tumor progression occurred. This is in accordance with findings that the proportion of *KRAS* mutations is higher in BilINs, IPN-Bs and early tumors than in advanced carcinomas (Hsu et al., 2013; Suto et al., 2000; Schlitter et al., 2014). These observations suggest that the majority of CCCs originate from clones carrying mutations in other genes than *KRAS* and only part of the precursor lesions with activated KRAS are able to progress to invasive carcinomas. *Pdx1-Cre;PIK3CA*$^{H1047R/+}$ mice develop carcinomas in the extrahepatic bile duct, but with a relatively long latency indicating that further genetic events are necessary for tumor progression. They display all three grades of BilINs during carcinogenesis and most likely acquire additional mutations in a step-wise fashion. While 1-month-old *Pdx1-Cre;PIK3CA*$^{H1047R/+}$ mice already show mild neoplasia in the CBD, they enter a senescent state around the age of 3 months as assessed by senescence-associated β-galactosidase staining. Activation of the PI3K-AKT-mTOR pathway by *PTEN* knock-out or expression of activated AKT1 equally induced senescence in the prostate epithelium (Chen et al., 2005; Majumder et al., 2008). In contrast, the bile duct from a *Pdx1-Cre;Kras*$^{G12D/+}$ mouse showing mild bile duct neoplasia did not undergo senescence. It has been shown in MEFs that expression of mutant Kras^{G12D} at endogenous levels does not induce senescence (Tuveson et al., 2004). Oncogene-induced senescence was nevertheless encountered in the pancreas of *Pdx1-Cre;Kras*$^{G12D/+}$ mice, again arguing for tissue specific differences (Caldwell et al., 2012).

Oncogene-induced senescence is frequently dependent on the tumor suppressors p53, INK4a and ARF, which are barely expressed under non-stressful conditions but are induced by oncogenic signaling. They exert a tumor suppressing defense mechanism through the induction of cell cycle arrest (Collado and Serrano, 2010; Xu et al., 2014). Xu and colleagues suggested that senescence in response to PI3K-AKT-mTOR pathway activation is dependent on p53 induction, mTORC1 activity and in contrast to RAS-induced senescence not associated with a DNA-damage response (Xu et al., 2014). Therefore, the role of a conditional *p53* deletion in *Pdx1-Cre;Kras*$^{G12D/+}$ and *Pdx1-Cre;PIK3CA*$^{H1047R/+}$ mice has been analyzed here.

p53 is a haplo-insufficient tumor suppressor and heterozygous deletion of *p53* in both *Pdx1-Cre;Kras*$^{G12D/+}$ and *Pdx1-Cre;PIK3CA*$^{H1047R/+}$ mice significantly reduced the survival and accelerated tumor development. Full deletion of *p53* further decreased survival in *Pdx1-Cre;PIK3CA*$^{H1047R/+}$ mice. The acceleration in tumor development indicates that p53 is still functional in both genotypes. Interestingly, there was a shift in the histological tumor type distribution towards PDAC formation at the expense of CBD carcinogenesis in *Pdx1-Cre;PIK3CA*$^{H1047R/+}$*;p53*$^{f/+}$ mice compared to *Pdx1-Cre;PIK3CA*$^{H1047R/+}$ mice. This shift in the

tumor type distribution does not mean that tumorigenesis in the CBD is completely blocked as BilIN lesions were still present and would probably further progress to cancer if the mice survived longer. A shift in the tumor type distribution rather shows that one tissue is more susceptible to the specific combination of mutations than another for its malignant transformation. The frequencies of *TP53* mutations are lower in BilINs compared to PanINs as well as in CCCs with 44% compared to PDACs with 85% (Aishima et al., 2014; Ong et al., 2012). Based on these data, pancreatic tumor formation is highly dependent on the disruption of p53 while alternative routes to cancer formation seem to exist in the biliary tract explaining the shift towards pancreatic carcinogenesis. Nevertheless, more than 30% human CCCs present p53 impairment with a higher frequency in extrahepatic CCCs compared to intrahepatic CCCs but a study of Jarnagin and coworkers demonstrated that proliferation rates in distal CCCs were equally high in p53 positive and p53 negative tumors (Hsu et al., 2013; Suto et al., 2000; Jarnagin et al., 2006; Borger et al., 2012; Simbolo et al., 2014). Only PDAC formation and no CCCs were observed in *Pdx1-Cre;Kras*$^{G12D/+}$*;p53*$^{f/+}$ mice although *p53* deletion in *Alb-Cre;Kras*$^{G12D/+}$ mice strongly enhanced intrahepatic CCC formation (O'Dell et al., 2012).

The conditional deletion of the *Cdkn2a* locus encoding p16 (Ink4a) and p19 (Arf) achieved completely different results in the two models. A heterozygous deletion of *Cdkn2a* in the *Pdx1-Cre;PIK3CA*$^{H1047R/+}$ model neither affected the median survival time nor the tumor type distribution. Preliminary results propose that *Pdx1-Cre;PIK3CA*$^{H1047R/+}$*;Cdkn2a*$^{f/f}$ mice have a shortened survival. The finding that there is no effect of a heterozygous *Cdkn2a* deletion suggests that p16 and/or p19 inactivation is induced in *PIK3CA*^{H1047R} initiated carcinogenesis eliminating the pressure to lose the second *Cdkn2a* allele. An analysis of primary PDAC cell lines derived from *Pdx1-Cre;Kras*$^{G12D/+}$*;Pten*$^{f/+}$ mice revealed a p16 deletion or *p16* promoter methylation as an obligatory cooperating event (Ying et al., 2011). MyrAKT-induced mammary carcinomas equally displayed loss of p16 expression (Blanco-Aparicio et al., 2010). *p16* promoter methylation is a frequent event in cancer and has been observed together with LOH of the *CDKN2A* locus in extrahepatic CCCs (Esteller, 2007; Caca et al., 2002). Preliminary data from mutant p110α-driven PDAC and CBD murine cell lines indicate a specific DNA methylation in the *p16* promoter region but not in the *p19* promoter. Interestingly, *Ptf1a*$^{Cre/+}$*;PIK3CA*$^{H1047R/+}$*;Cdkn2a*$^{f/+}$ mice lived significantly shorter than *Ptf1a*$^{Cre/+}$*;PIK3CA*$^{H1047R/+}$ mice but almost identical with *Pdx1-Cre;PIK3CA*$^{H1047R/+}$*;Cdkn2a*$^{f/+}$ mice (Eser et al., 2013). This indicates that the deletion of *Cdkn2a* can provide an advantage in the *Ptf1a*$^{Cre/+}$*;PIK3CA*$^{H1047R/+}$ model where pancreatic tumors develop very slowly with a median survival of 427 days (Eser et al., 2013). In contrast to the mutant p110α-driven model, heterozygous and to an even higher extent homozygous deletion of *Cdkn2a* decreased the survival when crossed into the *Pdx1-Cre;Kras*$^{G12D/+}$ model. *Pdx1-*

Cre;Kras$^{G12D/+}$*;Cdkn2a*$^{f/f}$ mice all died with an age of 2 to 3 months and this is in agreement with the data reported by Aguirre and colleagues on the same model (Aguirre et al., 2003). The survival data suggest that p16 and p19 are still functional in the Kras-driven model and that loss of the *Cdkn2a* locus provides a growth advantage to the tumor cells. Surprisingly, loss of *Cdkn2a* in *Pdx1-Cre;Kras*$^{G12D/+}$ mice enabled tumor progression in the CBD and revealed beginning carcinomas already in 3-month-old *Pdx1-Cre;Kras*$^{G12D/+}$*;Cdkn2a*$^{f/+}$ mice. Thus, mutant Kras and deletion of one or two *Cdkn2a* alleles appear to cooperate in tumor progression in the extrahepatic bile duct. Aguirre and colleagues did not describe any primary bile duct tumors in *Pdx1-Cre;Kras*$^{G12D/+}$*;Cdkn2a*$^{f/f}$ mice but biliary obstruction in 10 out of 24 mice which could have been misinterpreted primary CBD tumors (Aguirre et al., 2003).

Besides p19/p53/p21 and p16/Rb pathways a third mechanism of senescence, which is directly linked to PI3K-AKT signaling and p27, has been proposed (Bringold and Serrano, 2000). Several studies uncovered that inhibition of PI3K-AKT signaling results in upregulation of p27 (Shanmugasundaram et al., 2013; Nakamura et al., 2008; Viglietto et al., 2002). Along these lines, a tendency of decreased p27 expression was detected immunohistochemically on CBD tissue from *Pdx1-Cre;PIK3CA*$^{H1047R/+}$ mice when compared to wild type mice or *Pdx1-Cre;Kras*$^{G12D/+}$ mice. Nuclear p27 staining has been described in normal human biliary cells and is expected as p27 protein levels reach a maximum in cells in the G0 or G1 phase of the cell cycle (Jarnagin et al., 2006; Hui et al., 1999; Bloom and Pagano, 2003). Several mechanisms regulate p27 expression, stability as well as localization and all of them have been associated with PI3K-AKT signaling. First, p27 transcription is enhanced by FOXOs which are inactivated through AKT mediated phosphorylation (Stahl et al., 2002; Medema et al., 2000). Second, ubiquitination of p27 is mainly performed by the ubiquitin ligase SKP2 which is an E2F1 target gene and whose expression is induced by PI3K-AKT activation (Shanmugasundaram et al., 2013; Reichert et al., 2007). Third, AKT phosphorylates p27 on threonine 198, threonine 187, serine 10 and in humans but not in rodents on threonine 157 (Fujita et al., 2002; Viglietto et al., 2002; Liang et al., 2002; Shin et al., 2002). Most of these modifications induce nuclear export or retention of p27 in the cytoplasm (Kelly-Spratt et al., 2009; Chu et al., 2008). Reduced p27 expression occurs in several human cancers and is rarely due to mutations in the p27 encoding gene *CDKN1B* but rather results from reduced protein levels or mislocalization to the cytoplasm (Chu et al., 2008). While p27 threonine 187 phosphorylation and subsequent ubiquitination is crucial in an intestinal carcinoma mouse model, p27 is down-regulated on the mRNA level in lung cancer models (Timmerbeul et al., 2006; Kelly-Spratt et al., 2009). Nuclear p27 is decreased in extrahepatic CCCs and reduced p27 levels frequently co-occur with increased cyclin D1 expression (Jarnagin et al., 2006; Hui et al., 1999). Because of an autoinduction loop involving p27, SKP2, Rb and E2F, it is hard to

distinguish if p27 down-regulation in cancer is a primary event or the result of cyclin D1 and Rb deregulation (Assoian and Yung, 2008). A change in the p27 localization could not be observed in stainings of CBD tissue from *Pdx1-Cre;PIK3CA*$^{H1047R/+}$ mice but western blot analysis of nuclear and cytoplasmic fractions might be more sensitive for revealing cytoplasmic p27. In contrast to *Pdx1-Cre;PIK3CA*$^{H1047R/+}$ mice, *Pdx1-Cre;Kras*$^{G12D/+}$ mice did not show altered p27 expression in the CBD. Microinjection of recombinant Ras was able to reduce p27 expression *in vitro* and a chemically induced Kras-driven lung cancer model displayed reduced p27 mRNA and nuclear expression but *RAS* mutations in human NSCLC did not correlate with p27 levels (Sa and Stacey, 2004; Kelly-Spratt et al., 2009; Catzavelos et al., 1999). Expression levels of the oncogene might be relevant again and the inability of mutant Kras to reduce p27 expression might account for the fact that *Pdx1-Cre;Kras*$^{G12D/+}$ mice do not develop carcinomas in the extrahepatic bile duct.

Indeed, when one or both *p27* alleles were genetically deleted in the *Pdx1-Cre;Kras*$^{G12D/+}$ model, a highly significant shift towards CBD carcinogenesis occurred and the survival was significantly reduced in *Pdx1-Cre;Kras*$^{G12D/+}$*;p27*$^{-/-}$ mice. A heterozygous loss of *p27* was sufficient in *Pdx1-Cre;PIK3CA*$^{H1047R/+}$ mice to induce a significant reduction in the median survival time and a reduced tumor formation in the pancreas was observed as well. This indicates that the loss of p27 expression is a genetic event that can induce tumor progression in the extrahepatic bile duct and seems to be less relevant in pancreatic carcinogenesis. p27 has been described as haplo-insufficient tumor suppressor gene and the alterations in phenotype and survival time described here for mice lacking only one *p27* allele confirm this notion (Fero et al., 1998). Bloom and Pagano suggested that the growth advantage conferred by loss of one allele can be greater than by complete deletion and this can be due to the fact that p27 has functions related to cell migration in addition to its activity as cell cycle regulator (Bloom and Pagano, 2003; Iancu-Rubin and Atweh, 2005; Wander et al., 2013; Chu et al., 2008). Nevertheless, only deletion of both alleles significantly accelerated tumor formation in *Pdx1-Cre;Kras*$^{G12D/+}$ mice and this may be due to differences in posttranslational modifications when compared to *Pdx1-Cre;PIK3CA*$^{H1047R/+}$ mice.

A cooperation of heterozygous *PTEN* loss and *p27* knock-out on tumor formation in prostate, thyroid, endometrium and small intestine has been described (Di Cristofano et al., 2001). Equally, a cooperation of activated AKT and p27 loss has been observed in prostate cancer formation, but not for mammary carcinoma, again emphasizing tissue specific differences (Majumder et al., 2008; Blanco-Aparicio et al., 2010). Analysis of prostate carcinogenesis driven by expression of activated AKT or activated Myc revealed senescence associated with elevated p27 expression induced by the phenotypic changes occurring in prostatic intraepithelial neoplasia (Majumder et al., 2008). A senescence mechanism dependent on p27, p21 and Atf4 has been demonstrated *in vitro* and *in vivo* by Lin and colleagues (Lin et

al., 2010). *Pdx1-Cre;PIK3CA*$^{H1047R/+}$ mice show senescence in premalignant CBD tissue at an age of three months but p27 expression is not stabilized at that time point but already decreased, thus conflicting with the mechanism proposed by Majumder and coworkers (Majumder et al., 2008). Potentially, loss of p27 is already beneficial in a very early step of carcinogenesis enhancing proliferation of mutant p110α-induced clones and further loss of another tumor suppressor such as p16 is required to circumvent senescence. Last, a non-cell autonomous effect of genetic *p27* deletion on carcinogenesis is conceivable as a general knock-out mouse line has been used. A non-cell autonomous effect has been excluded by neonatal lung tissue transplantation for the lung cancer model described by Kelly-Spratt and colleagues (Kelly-Spratt et al., 2009). A cell autonomous mechanism is very likely in CBD carcinogenesis as regulation of p27 expression has been observed in *p27*-proficient biliary epithelial cells.

Independent of the exact mechanism, reduced p27 expression is a common feature of CBD carcinomas that developed in *Pdx1-Cre;PIK3CA*$^{H1047R/+}$, *Pdx1-Cre;PIK3CA*$^{H1047R/H1047R}$, *Pdx1-Cre;PIK3CA*$^{H1047R/+}$*;p27*$^{+/-}$, *Pdx1-Cre;Kras*$^{G12D/+}$*;p27*$^{+/-}$ and *Pdx1-Cre;Kras*$^{G12D/+}$*;p27*$^{-/-}$ mice and has been observed in human extrahepatic CCCs as well (Jarnagin et al., 2006; Hui et al., 1999). Due to the fact that the *CDKN1B* gene is intact in the great majority of human cancers and only the expression and localization are deregulated, Chu and coworkers suggested that stabilization of p27 may be an efficient therapeutic strategy (Chu et al., 2008). Treatment of mice harboring chemically induced lung tumors with a PI3K inhibitor indeed reversed mislocalization of p27 (Kelly-Spratt et al., 2009). Inhibitors of PI3K or AKT are currently tested in clinical trials for various solid cancers including biliary tract cancers (Sheppard et al., 2012; Geynisman and Catenacci, 2012; Noel and Hezel, 2013). Treatment with inhibitors of PI3K-AKT-mTOR signaling could be specifically beneficial for extrahepatic CCC patients that exhibit low nuclear p27 levels.

5.3 A next-generation triple-recombination system

The *FSF-PIK3CA*^{H1047R} mouse line generated in this work will contribute to a next-generation triple-recombination system in the future that will enable among other applications modeling of therapeutic PI3K inhibition in established p110α^{H1047R}-driven tumors. The generation of the *pRosa26-FSF-PIK3CA*^{H1047R} targeting vector as well as ES cell targeting were accomplished successfully. Tissue specific expression of the mutant p110α allele occurred in a Flp-dependent manner and was able to generate neoplastic changes in the affected tissues. Preliminary results from the first *Pdx1-Flp;FSF-PIK3CA*$^{H1047R/+}$ mice indicate a recapitulation of the multi-organ phenotype observed in *Pdx1-Cre;LSL-PIK3CA*$^{H1047R/+}$ mice.

A special feature of the new *FSF-PIK3CA*^{H1047R} mouse line is the presence of two rox sites flanking the frt-stop-frt-PIK3CA^{H1047R} expression cassette, which can be recognized by the Dre recombinase. The cloning of a *Dre-ERT2* knock-in into the ubiquitously transcribed *hypoxanthine guanine phosphoribosyl transferase 1* locus is still in progress (Yang et al., 2009). The expression of Dre-ERT2 will be driven by the exogenous caggs promoter, which ensures strong expression in all tissues (Okabe et al., 1997). The expression is further dependent on the Cre or Flp mediated excision of a stop cassette located downstream of the caggs promoter (Figure 5-1). The *Dre* coding sequence with truncation of the nuclear localization signal is fused in frame to a tamoxifen-inducible, mutant *estrogen binding domain (ERT2)*. A 15 base pair sequence that has been established in the *FlpeERT2* construct has been used to link the *Dre* sequence with the *ERT2* sequence (Hunter et al., 2005). In addition, a woodchuck hepatitis virus posttranscriptional regulatory element has been cloned between the *Dre-ERT2* stop codon and the pA sequence in order to increase the stability of the transcript (Madisen et al., 2010).

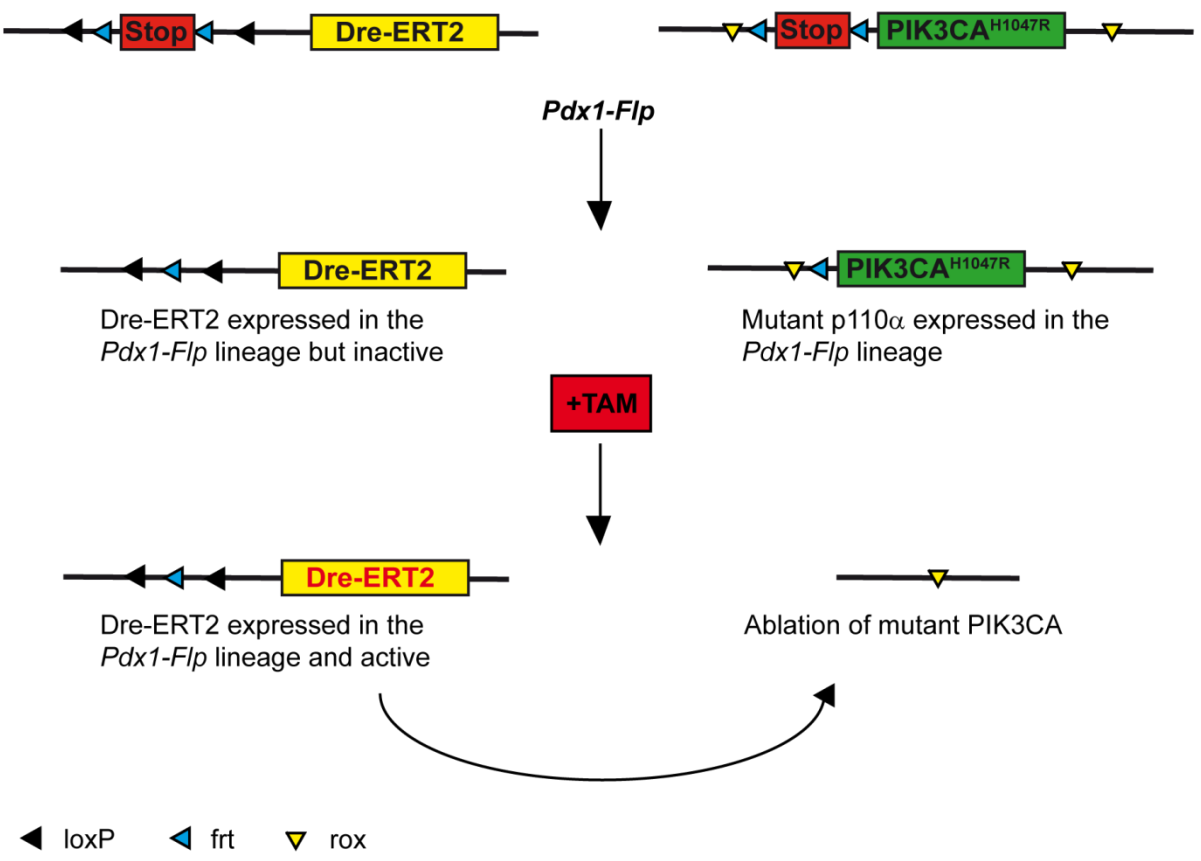

Figure 5-1: Mode of action of the triple-recombination system.

When combining *FSF-PIK3CA*^{H1047R} and *Dre-ERT2* alleles with a Flp recombinase mouse line (e.g. *Pdx1-Flp*), both stop cassettes are cut out and oncogenic p110α^{H1047R} and Dre-ERT2 are expressed dependent on Flp activity. Dre-ERT2 executes its recombinase activity in the nucleus only following tamoxifen administration resulting in excision of the mutant *PIK3CA* allele. Endogenous *PIK3CA* is not affected.

Figure 5-1 depicts how this new mouse line can be used in combination with the *Pdx1-Flp* and *FSF-PIK3CA*^{H1047R} mouse lines to induce expression of mutant p110α in the *Pdx1-Flp* lineage beginning at E8.5 and disrupt the expression of mutant p110α at any time point of interest by tamoxifen administration. One possibility is to start tamoxifen administration once a tumor has developed in order to mimic therapy with a PI3K inhibitor. This can provide information on the dependency of the tumor on PI3K-AKT-mTOR signaling, on resistance mechanisms as demonstrated by Liu and colleagues in a tetracycline-inducible system, or show molecular effects of PI3K inhibition such as potential changes in p27 localization (Liu et al., 2011). Tamoxifen administration can be started at earlier time points to study the role of PI3K-AKT-mTOR signaling in developing tumors or primary tumor cells lines isolated from *Pdx1-Flp;FSF-PIK3CA*$^{H1047R/+}$*;Dre-ERT2* mice can be treated with tamoxifen *in vitro*.

Furthermore, the new *FSF-PIK3CA*^{H1047R} mouse line can be crossed with other tissue specific Flp mouse lines and combined with the Cre-loxP system offering a great variety of applications in tumor modeling as described by Schönhuber and coworkers (Schönhuber et al., 2014).

5.4 Outlook

In this work, GEMMs for the carcinogenesis in the hepatobiliary tract have been established and characterized. The *Alb-Cre;PIK3CA*$^{H10470R/+}$ model displayed many parallels with the established *Alb-Cre;Pten*$^{f/f}$ mouse model and provides a model for the study of NAFLD, NASH and liver carcinogenesis. It remains unclear whether the expression of mutant p110α in the liver directly induces transformation of hepatocytes, cholangiocytes or progenitor cells or if the steatosis environment induced by constitutive insulin signaling triggers tumorigenesis. We are currently investigating if the knock-out of *Pdk1* in the liver of *Alb-Cre;PIK3CA*$^{H10470R/+}$ mice can block or attenuate steatosis and tumor formation. The new triple recombination system could also help to address the question if mutant p110α-induced steatosis is sufficient for tumorigenesis. Combining *FSF-PIK3CA*^{H1047R} and *Dre-ERT2* mouse lines with an *Alb-Flp* line could be used to inactivate mutant p110α at an age of 3 to 6 months when steatosis is established. This experiment could reveal if mutant p110α is still required when liver steatosis has already developed.

The carcinogenesis in the extrahepatic bile duct has not been extensively studied in GEMMs up to now. This work analyzed the cooperation of mutant p110α^{H1047R} and mutant Kras^{G12D} with different tumor suppressor gene deletions in carcinogenesis in the extrahepatic bile duct. Survival and histological data gave first insights into the relevance of different molecular pathways but the exact mechanisms driving tumorigenesis in the CBD are still unknown. Deletion of the cell cycle regulator p27 showed the most promising effects *in vivo* and will be

studied further *in vitro* due to limited amount of CBD tissue. A CRISPR-Cas9 mediated *p27* knock-out has already been achieved in primary tumor cells from *Pdx1-Cre;PIK3CA*$^{H10470R/+}$ mice and an overexpression plasmid is available as well (Ran et al., 2013). Transcriptome analysis of *p27* wild type, *p27* knock-out and *p27* overexpressing cells derived from the same parental cell line will broaden the knowledge on p27 functions and p27 regulated pathways in biliary tumor cells. Analysis of p27 mRNA expression and p27 localization will provide insights into the regulation of p27 in cells expressing oncogenic p110α. A heterozygous deletion of *Cdkn2a* turned out to cooperate with mutant Kras in CBD carcinogenesis but did not provide any advantage in *Pdx1-Cre;PIK3CA*$^{H10470R/+}$ mice. The integrity of the *Cdkn2a* locus and promoter methylation status should be analyzed in *Pdx1-Cre;PIK3CA*$^{H10470R/+}$ mice. Pathways involving different tumor suppressors including p53, p16 and p27 can contribute to oncogene-induced senescence and it is not clear yet which pathway triggers the senescence phenotype observed in 3-month-old *Pdx1-Cre;PIK3CA*$^{H10470R/+}$ mice (Bringold and Serrano, 2000). Generation of stress-induced senescence in tumor cells isolated from *Pdx1-Cre;PIK3CA*$^{H10470R/+}$ mice and subsequent analysis of the protein expression of p19, p53, p16, p21 and p27 could elucidate which pathways are involved.

6 Summary

Liver cancers are the second most common cause of cancer related deaths worldwide and the PI3K-AKT-mTOR signaling pathway is frequently overactivated in these cancers. Therefore, a genetically engineered mouse model expressing oncogenic p110α^{H1047R} specifically in the liver has been generated. Expression of p110α^{H1047R} results in early onset liver steatosis and steatohepatis followed by hepatocellular carcinoma (HCC) and cholangiocellular carcinoma (CCC) formation in older mice, thus providing a new model for human Nonalcoholic Fatty Liver Disease and progression to liver cancer.

Extrahepatic bile duct cancer is the most common form of CCC, but molecular mechanisms driving this tumor entity are still largely unknown. Here a novel genetically engineered mouse model of human extrahepatic CCC has been generated and revealed that oncogenic p110α induces tumor formation. Expression of p110α^{H1047R} induces biliary intraepithelial neoplasms that progress with long latency to invasive CCC. In contrast, oncogenic Kras^{G12D} is not capable of inducing major neoplastic changes in the bile duct epithelium. While a conditional deletion of *p53* in these models does not favor extrahepatic CCC formation, the conditional deletion of the *Cdkn2a* locus cooperates with oncogenic Kras^{G12D} in CCC progression in the extrahepatic bile duct. Molecular analyses revealed a selective downregulation of p27 by p110α^{H1047R} in the bile duct. In line, deletion of *p27* considerably accelerates tumor formation in the *PIK3CA*^{H1047R} model. Interestingly, the knock-out of *p27* induces also extrahepatic bile duct cancer in the *Kras*^{G12D} model. These findings indicate that the cell cycle regulator p27 contributes to an initial barrier towards bile duct tumorigenesis that has to be eliminated before invasive tumors can develop. While expression of mutant p110α is sufficient to reduce p27 levels, expression of mutant Kras cannot overcome this barrier. This contrasts pancreatic carcinogenesis, where both, p110α^{H1047R} and Kras^{G12D} induce tumor formation independent of p27 inactivation. These results demonstrate tissue specific differences in p110α^{H1047R} and Kras^{G12D}-induced cancer initiation and progression, and suggest that p27 might be a target for therapy of extrahepatic CCC.

In order to mimic therapeutic PI3K inhibition *in vivo*, a new mouse line has been generated that enables conditional expression of oncogenic p110α^{H1047R} via Flp-mediated recombination and subsequent inactivation of the oncogene through Dre-mediated recombination after tumor formation.

7 Zusammenfassung

Leberkrebs stellt weltweit die zweithäufigste Ursache für tumorbedingte Todesfälle dar und der PI3K-AKT-mTOR Signalweg ist in diesen Tumoren häufig überaktiviert. Deshalb wurde ein genetisch definiertes Mausmodell generiert, in dem onkogenes p110α^{H1047R} speziell in der Leber exprimiert wird. Die Expression von p110α^{H1047R} führt sehr früh zur Entwicklung einer nicht-alkoholischen Fettleber und Steatohepatitis sowie zur Entstehung von hepatozellulären (HCC) und cholangiozellulären (CCC) Karzinomen in älteren Mäusen. Damit stellt diese genetisch definierte Mauslinie ein neues Modell für die humane Fettlebererkrankung und Lebertumorentwicklung dar.

Karzinome der extrahepatischen Gallengänge sind die häufigste Form des CCC. Die molekularen Mechanismen, die diese Tumore verursachen, sind größtenteils aber noch nicht bekannt. Hier wurde ein neuartiges genetisch definiertes Mausmodell für humane extrahepatische CCCs geschaffen, wobei sich herausstellte, dass onkogenes p110α die Tumorentstehung induzieren kann. Die Expression von p110α^{H1047R} induziert biliäre intraepitheliale Neoplasien, die mit einer langen Latenzzeit zum invasiven CCC fortschreiten. Im Gegensatz dazu ist onkogenes Kras^{G12D} nicht in der Lage, invasive Tumoren im Gallengangsepithel zu induzieren. Während eine konditionale Deletion von *p53* in diesen Modellen die extrahepatische CCC-Entwicklung nicht akzeleriert, kooperiert eine konditionale Deletion des *Cdkn2a*-Locus mit onkogenem Kras^{G12D} hinsichtlich der CCC-Progression im extrahepatischen Gallengang. Molekulare Analysen zeigten eine selektive Herunterregulierung von p27 durch p110α^{H1047R} im Gallengang. Damit einhergehend beschleunigt auch eine Deletion von *p27* die Tumorentstehung im *PIK3CA^{H1047R}*-Modell beträchtlich. Interessanterweise induziert der Knock-out von *p27* auch im *Kras^{G12D}*-Modell Karzinome im extrahepatischen Gallengang. Diese Ergebnisse weisen darauf hin, dass der Zellzyklusregulator p27 eine Barriere darstellt, die ausgeschaltet werden muss bevor sich Gallengangstumore entwickeln können. Während die Expression von mutiertem p110α hinreichend ist, um die Expression von p27 zu reduzieren, kann die Expression von mutiertem Kras diese Barriere nicht überwinden. Dies steht im Gegensatz zur Karzinogenese im Pankreas, in der sowohl p110α^{H1047R} als auch Kras^{G12D} die Tumorentstehung unabhängig von einer p27-Inaktivierung induzieren. Diese Ergebnisse zeigen gewebsspezifische Unterschiede bezüglich der Rolle von p110α^{H1047R} und Kras^{G12D} bei der Initiierung und Progression von Karzinomen und legen nahe, dass sich p27 als Zielstruktur zur Behandlung von extrahepatischen CCCs eignen könnte.

Um eine therapeutische Hemmung von PI3K *in vivo* zu imitieren, wurde eine neue Mauslinie entwickelt, die onkogenes p110α^{H1047R} Flp-abhängig konditional exprimiert, gefolgt von einer induzierbaren Deletion des *PIK3CA*^{H1047R} Onkogens im ausgebildeten Tumor durch Dre-vermittelte Rekombination.

8 References

Abraham, S.C., Lee, J.H., Hruban, R.H., et al. (2003) Molecular and immunohistochemical analysis of intraductal papillary neoplasms of the biliary tract. **Human Pathology**, 34: 902–910

Aguirre, A.J., Bardeesy, N., Sinha, M., et al. (2003) Activated Kras and Ink4a / Arf deficiency cooperate to produce metastatic pancreatic ductal adenocarcinoma. **Genes & Development**, 17 (24): 3112–3126

Aishima, S., Kubo, Y., Tanaka, Y., et al. (2014) Histological features of precancerous and early cancerous lesions of biliary tract carcinoma. **Journal Hepatobiliary Pancreatic Sciences**, 21: 448–452

Alexandrov, L.B., Nik-Zainal, S., Wedge, D.C., et al. (2013) Signatures of mutational processes in human cancer. **Nature**, 500 (7463): 415–21

Anastassiadis, K., Fu, J., Patsch, C., et al. (2009) Dre recombinase, like Cre, is a highly efficient site-specific recombinase in E. coli, mammalian cells and mice. **Disease Models & Mechanisms**, 2 (9-10): 508–15

Artandi, S.E., Chang, S., Lee, S.L., et al. (2000) Telomere dysfunction promotes non-reciprocal translocations and epithelial cancers in mice. **Nature**, 406 (6796): 641–645

Assoian, R.K. and Yung, Y. (2008) A reciprocal relationship between Rb and Skp2: implications for restriction point control, signal transduction to the cell cycle, and cancer. **Cell Cycle**, 7 (1): 24–27

Blanco-Aparicio, C., Cañamero, M., Cecilia, Y., et al. (2010) Exploring the gain of function contribution of AKT to mammary tumorigenesis in mouse models. **PloS ONE**, 5 (2): e9305

Bloom, J. and Pagano, M. (2003) Deregulated degradation of the cdk inhibitor p27 and malignant transformation. **Seminars in Cancer Biology**, 13 (1): 41–47

Boige, V., Laurent-Puig, P., Fouchet, P., et al. (1997) Concerted nonsyntenic allelic losses in hyperploid hepatocellular carcinoma as determined by a high-resolution allelotype. **Cancer Research**, 57: 1986–1990

Borger, D.R., Tanabe, K.K., Fan, K.C., et al. (2012) Frequent mutation of isocitrate dehydrogenase (IDH)1 and IDH2 in cholangiocarcinoma identified through broad-based tumor genotyping. **The Oncologist**, 17: 72–79

Borlak, J., Meier, T., Halter, R., et al. (2005) Epidermal growth factor-induced hepatocellular carcinoma: gene expression profiles in precursor lesions, early stage and solitary tumours. **Oncogene**, 24: 1809–1819

Boyault, S., Rickman, D.S., De Reyniès, A., et al. (2007) Transcriptome classification of HCC is related to gene alterations and to new therapeutic targets. **Hepatology**, 45: 42–52

Boyer, J.L. (2013) Bile formation and secretion. **Comprehensive Physiology**, 3 (3): 1035–1078

Bressac, B., Kew, M., Wands, J., et al. (1991) Selective G to T mutations of p53 gene in hepatocellular carcinoma from southern Africa. **Nature**, 350: 429–431

Brill, S., Zvibel, I., Halpern, Z., et al. (2002) The role of fetal and adult hepatocyte extracellular matrix in the regulation of tissue-specific gene expression in fetal and adult hepatocytes. **European Journal of Cell Biology**, 81 (1): 43–50

Bringold, F. and Serrano, M. (2000) Tumor suppressors and oncogenes in cellular senescence. **Experimental Gerontology**, 35: 317–329

Buchmann, A., Bauer-Hofmann, R., Mahr, J., et al. (1991) Mutational activation of the c-Ha-ras gene in liver tumors of different rodent strains: correlation with susceptibility to hepatocarcinogenesis. **Proceedings of the National Academy of Sciences of the United States of America**, 88: 911–915

Caca, K., Feisthammel, J., Klee, K., et al. (2002) Inactivation of the INK4A/ARF locus and p53 in sporadic extrahepatic bile duct cancer and bile tract cancer cell lines. **International Journal of Cancer**, 97: 481–488

Caldwell, M.E., DeNicola, G.M., Martins, C.P., et al. (2012) Cellular features of senescence during the evolution of human and murine ductal pancreatic cancer. **Oncogene**, 31 (12): 1599–1608

Campbell, D.J., Dumur, C.I., Lamour, N.F., et al. (2012) Novel organotypic culture model of cholangiocarcinoma progression. **Hepatology Research**, 42 (11): 1119–1130

Cardinale, V., Semeraro, R., Torrice, A., et al. (2010) Intra-hepatic and extra-hepatic cholangiocarcinoma: New insight into epidemiology and risk factors. **World Journal of Gastrointestinal Oncology**, 2 (11): 407–416

Cardinale, V., Wang, Y., Carpino, G., et al. (2011) Multipotent stem/progenitor cells in human biliary tree give rise to hepatocytes, cholangiocytes, and pancreatic islets. **Hepatology**, 54 (6): 2159–2172

Carnero, A. and Paramio, J.M. (2014) The PTEN/PI3K/AKT pathway in vivo, cancer mouse models. **Frontiers in Oncology**, 4: 1–10

Carpino, G., Cardinale, V., Onori, P., et al. (2012) Biliary tree stem/progenitor cells in glands of extrahepatic and intraheptic bile ducts: an anatomical in situ study yielding evidence of maturational lineages. **Journal of Anatomy**, 220: 186–199

Castellano, E. and Downward, J. (2011) RAS interaction with PI3K: more than just another effector pathway. **Genes & Cancer**, 2 (3): 261–274

Catzavelos, C., Tsao, M.S., DeBoer, G., et al. (1999) Reduced expression of the cell cycle inhibitor p27Kip1 in non-small cell lung carcinoma: a prognostic factor independent of Ras. **Cancer Research**, 59 (3): 684–688

Chen, Z., Trotman, L.C., Shaffer, D., et al. (2005) Crucial role of p53-dependent cellular senescence in suppression of Pten-deficient tumorigenesis. **Nature**, 436 (7051): 725–730

Chetty, R. and Govender, D. (2013) Gene of the month: KRAS. **Journal of Clinical Pathology**, 66 (7): 548–550

Chu, I.M., Hengst, L. and Slingerland, J.M. (2008) The Cdk inhibitor p27 in human cancer: prognostic potential and relevance to anticancer therapy. **Nature Reviews Cancer**, 8 (4): 253–267

Chung, J.-Y., Hong, S.-M., Choi, B.Y., et al. (2009) The expression of phospho-AKT, phospho-mTOR, and PTEN in extrahepatic cholangiocarcinoma. **Clinical Cancer Research**, 15 (2): 660–7

Collado, M. and Serrano, M. (2010) Senescence in tumours: evidence from mice and humans. **Nature Reviews Cancer**, 10 (1): 51–57

Collisson, E.A., Trejo, C.L., Silva, J.M., et al. (2012) A central role for RAF→MEK→ERK signaling in the genesis of pancreatic ductal adenocarcinoma. **Cancer Discovery**, 2 (8): 685–693

Confer, D.B. and Stenger, R.J. (1966) Nodules in the livers of C3H mice after long-term carbon tetrachloride administration: a light and electron microscopic study. **Cancer Research**, 26: 834–843

Di Cristofano, A., Acetis, M. De, Koff, A., et al. (2001) Pten and p27KIP1 cooperate in prostate cancer tumor suppression in the mouse. **Nature Genetics**, 27 (2): 222–224

Deshpande, V., Nduaguba, A., Zimmerman, S.M., et al. (2011) Mutational profiling reveals PIK3CA mutations in gallbladder carcinoma. **BMC Cancer**, 11: 60

El-Serag, H.B. (2011) Hepatocellular carcinoma. **New England Journal of Medicine**, 365 (12): 1118–1127

El-Serag, H.B. and Kanwal, F. (2014) Epidemiology of hepatocellular carcinoma in the United States: Where are we? Where do we go? **Hepatology**, 60 (5): 1767–1775

El-Serag, H.B. and Rudolph, K.L. (2007) Hepatocellular carcinoma: epidemiology and molecular carcinogenesis. **Gastroenterology**, 132: 2557–2576

Eser, S., Reiff, N., Messer, M., et al. (2013) Selective requirement of PI3K/PDK1 signaling for Kras oncogene-driven pancreatic cell plasticity and cancer. **Cancer Cell**, 23: 1–15

Eser, S., Schnieke, A., Schneider, G., et al. (2014) Oncogenic KRAS signalling in pancreatic cancer. **British Journal of Cancer**, 111: 817–822

Esteller, M. (2007) Epigenetic gene silencing in cancer: the DNA hypermethylome. **Human Molecular Genetics**, 16 (Spec No 1): R50–59

Farazi, P. a, Zeisberg, M., Glickman, J., et al. (2006) Chronic bile duct injury associated with fibrotic matrix microenvironment provokes cholangiocarcinoma in p53-deficient mice. **Cancer Research**, 66 (13): 6622–6627

Fava, G., Alpini, G., Rychlicki, C., et al. (2008) Leptin enhances cholangiocarcinoma cell growth. **Cancer Research**, 68 (16): 6752–6761

Fava, G., Marucci, L., Glaser, S., et al. (2005) γ-aminobutyric acid inhibits cholangiocarcinoma growth by cyclic AMP-dependent regulation of the protein kinase A/extracellular signal-regulated kinase 1/2 pathway. **Cancer Research**, 65 (24): 11437–11446

Fearon, E.R. and Vogelstein, B. (1990) A genetic model for colorectal tumorigenesis. **Cell**, 61 (5): 759–67

Ferlay, J., Soerjomataram, I., Ervik, M., et al. (2013) **GLOBOCAN 2012 v1.0, Cancer Incidence and Mortality Worldwide: IARC CancerBase No. 11 [internet]**. Lyon, France. http://globocan.iarc.fr, accessed 19/06/2015

Fero, M.L., Randel, E., Gurley, K.E., et al. (1998) The murine gene p27Kip1 is haplo-insufficient for tumour suppression. **Nature**, 396: 177–180

Fero, M.L., Rivkin, M., Tasch, M., et al. (1996) A syndrome of multiorgan hyperplasia with features of gigantism, tumorigenesis, and female sterility in p27Kip1-deficient mice. **Cell**, 85 (5): 733–44

Fleischmann, M. and Iynedjian, P.B. (2000) Regulation of sterol regulatory-element binding protein 1 gene expression in liver : role of insulin and protein kinase B/cAkt. **Biochemical Journal**, 349: 13–17

Forbes, S.A., Beare, D., Gunasekaran, P., et al. (2015) COSMIC: exploring the world's knowledge of somatic mutations in human cancer. **Nucleic Acids Research**, 43 (Database issue): D805–D811

Fujimoto, A., Totoki, Y., Abe, T., et al. (2012) Whole-genome sequencing of liver cancers identifies etiological influences on mutation patterns and recurrent mutations in chromatin regulators. **Nature Genetics**, 44 (7): 760–764

Fujita, N., Sato, S., Katayama, K., et al. (2002) Akt-dependent phosphorylation of p27Kip1 promotes binding to 14-3-3 and cytoplasmic localization. **The Journal of Biological Chemistry**, 277 (32): 28706–28713

Fukuda, A., Kawaguchi, Y., Furuyama, K., et al. (2006) Loss of the major duodenal papilla results in brown pigment biliary stone formation in pdx1 null mice. **Gastroenterology**, 130 (3): 855–67

Galicia, V. a, He, L., Dang, H., et al. (2010) Expansion of hepatic tumor progenitor cells in Pten-null mice requires liver injury and is revered by loss of AKT2. **Gastroenterology**, 139 (6): 2170–2182

Gannon, M., Herrera, P. and Wright, C.V.E. (2000) Mosaic Cre-mediated recombination in pancreas using the pdx-1 enhancer/promoter. **Genesis**, 26: 143–144

Geynisman, D.M. and Catenacci, D.V.T.T. (2012) Toward personalized treatment of advanced biliary tract cancers. **Discovery Medicine**, 14 (74): 41–57

Giannini, E.G., Testa, R. and Savarino, V. (2005) Liver enzyme alteration: a guide for clinicians. **Canadian Medical Association Journal**, 172 (3): 367–379

Goldstein, J.L., DeBose-Boyd, R. a. and Brown, M.S. (2006) Protein sensors for membrane sterols. **Cell**, 124 (1): 35–46

Gray, R., Peto, R., Brantom, P., et al. (1991) Chronic nitrosamine ingestion in 1040 rodents: the effect of the choice of nitrosamine, the species studied, and the age of starting exposure. **Cancer Research**, 51: 6470–6491

Gualdi, R., Bossard, P., Zheng, M., et al. (1996) Hepatic specification of the gut endoderm in vitro: cell signaling and transcriptional control. **Genes & Development**, 10: 1670–1682

Guerra, C., Mijimolle, N., Dhawahir, A., et al. (2003) Tumor induction by an endogenous K-ras oncogene is highly dependent on cellular context. **Cancer Cell**, 4 (2): 111–120

Guz, Y., Montminy, M.R., Stein, R., et al. (1995) Expression of murine STF-1, a putative insulin gene transcription factor, in β cells of pancreas, duodenal epithelium and pancreatic exocrine and endocrine progenitors during ontogeny. **Development**, 121: 11–18

Hacker, H.J., Mtiro, H., Bannasch, P., et al. (1991) Histochemical profile of mouse hepatocellular adenomas and carcinomas induced by a single dose of diethylnitrosamine. **Cancer Research**, 51 (7): 1952–1958

Hansel, D.E., Rahman, A., Hidalgo, M., et al. (2003) Identification of novel cellular targets in biliary tract cancers using global gene expression technology. **The American Journal of Pathology**, 163 (1): 217–229

Harada, N., Oshima, H., Katoh, M., et al. (2004) Hepatocarcinogenesis in mice with beta-catenin and Ha-ras gene mutations. **Cancer Research**, 64: 48–54

He, L., Hou, X., Kanel, G., et al. (2010) The critical role of AKT2 in hepatic steatosis induced by PTEN loss. **The American journal of pathology**, 176 (5): 2302–8

Heindryckx, F., Colle, I. and Van Vlierberghe, H. (2009) Experimental mouse models for hepatocellular carcinoma research. **International Journal of Experimental Pathology**, 90: 367–386

Hingorani, S.R., Iii, E.F.P., Maitra, A., et al. (2003) Preinvasive and invasive ductal pancreatic cancer and its early detection in the mouse. **Cancer Cell**, 4: 437–450

Hino, O., Tabata, S. and Hotta, Y. (1991) Evidence for increased in vitro recombination with insertion of human hepatitis B virus DNA. **Proceedings of the National Academy of Sciences of the United States of America**, 88 (20): 9248–9252

Honig, G., Liou, A., Berger, M., et al. (2010) Precise pattern of recombination in serotonergic and hypothalamic neurons in a Pdx1-cre transgenic mouse line. **Journal of Biomedical Science**, 17 (1): 82

Horie, Y., Suzuki, A., Kataoka, E., et al. (2004) Hepatocyte-specific Pten deficiency results in steatohepatitis and hepatocellular carcinomas. **The Journal of Clinical Investigation**, 113 (12): 1774–1783

Hou, Y.-J., Dong, L.-W., Tan, Y.-X., et al. (2011) Inhibition of active autophagy induces apoptosis and increases chemosensitivity in cholangiocarcinoma. **Laboratory Investigation**, 91 (8): 1146–1157

Hruban, R.H., Goggins, M., Parsons, J., et al. (2000) Progression model for pancreatic cancer. **Clinical Cancer Research**, 6: 2969–2972

Hsu, I.C., Matcalf, R.A., Sun, T., et al. (1991) Mutational hotspot in the p53 gene in human hepatocellular carcinomas. **Nature**, 350 (6317): 427–428

Hsu, M., Sasaki, M., Igarashi, S., et al. (2013) KRAS and GNAS mutations and p53 overexpression in biliary intraepithelial neoplasia and intrahepatic cholangiocarcinomas. **Cancer**, 119 (9): 1669–1674

Hu, T.-H., Huang, C.-C., Lin, P.-R., et al. (2003) Expression and prognostic role of tumor suppressor gene PTEN/MMAC1/TEP1 in hepatocellular carcinoma. **Cancer**, 97 (8): 1929–1940

Hui, A.-M., Cui, X., Makuuchi, M., et al. (1999) Decreased p27Kip1 expression and cyclin D1 overexpression, alone and in combination, influence recurrence and survival of patients with resectable extrahepatic bile duct carcinoma. **Hepatology**, 30 (5): 1167–1173

Hunter, N.L., Awatramani, R.B., Farley, F.W., et al. (2005) Ligand-activated Flpe for temporally regulated gene modifications. **Genesis**, 41 (3): 99–109

Huynh, H., Soo, K.C., Chow, P.K.H., et al. (2006) Xenografts of human hepatocellular carcinoma: a useful model for testing drugs. **Clinical Cancer Research**, 12 (14): 4306–4314

Iancu-Rubin, C. and Atweh, G.F. (2005) p27Kip1 and stathmin share the stage for the first time. **TRENDS in Cell Biology**, 15 (7): 346–348

Jackson, E.L., Willis, N., Mercer, K., et al. (2001) Analysis of lung tumor initiation and progression using conditional expression of oncogenic K-ras. **Genes & Development**, 15: 3243–3248

Janssen, K.P., Abala, M., El Marjou, F., et al. (2005) Mouse models of K-ras-initiated carcinogenesis. **Biochimica et Biophysica Acta**, 1756 (2): 145–154

Jarnagin, W.R., Klimstra, D.S., Hezel, M., et al. (2006) Differential cell cycle-regulatory protein expression in biliary tract adenocarcinoma: correlation with anatomic site, pathologic variables, and clinical outcome. **Journal of Clinical Oncology**, 24 (7): 1152–1160

Jhappan, C., Stahle, C., Harkins, R.N., et al. (1990) TGFα overexpression in transgenic mice induces liver neoplasia and abnormal development of the mammary gland and pancreas. **Cell**, 61: 1137–1146

Jonkers, J., Meuwissen, R., van der Gulden, H., et al. (2001) Synergistic tumor suppressor activity of BRCA2 and p53 in a conditional mouse model for breast cancer. **Nature Genetics**, 29 (4): 418–425

Kelly-Spratt, K.S., Philipp-Staheli, J., Gurley, K.E., et al. (2009) Inhibition of PI-3K restores nuclear p27Kip1 expression in a mouse model of Kras-driven lung cancer. **Oncogene**, 28 (41): 3652–3662

Kenerson, H.L., Yeh, M.M., Kazami, M., et al. (2013) Akt and mTORC1 have different roles during liver tumorigenesis in mice. **Gastroenterology**, 144 (5): 1055–1065

Kiguchi, K., Carbajal, S., Chan, K., et al. (2001) Constitutive expression of ErbB-2 in gallbladder epithelium results in development of adenocarcinoma. **Cancer Research**, 61: 6971–6976

Kipp, B.R., Voss, J.S., Kerr, S.E., et al. (2012) Isocitrate dehydrogenase 1 and 2 mutations in cholangiocarcinoma. **Human Pathology**, 43 (10): 1552–1558

Klaman, L.D., Boss, O., Peroni, O.D., et al. (2000) Increased energy expenditure, decreased adiposity, and tissue-specific insulin sensitivity in protein-tyrosine phosphatase 1B-deficient mice. **Molecular and Cellular Biology**, 20 (15): 5479–5489

Knight, B., Yeoh, G.C., Husk, K.L., et al. (2000) Impaired preneoplastic changes and liver tumor formation in tumor necrosis factor receptor type 1 knockout mice. **The Journal of Experimental Medicine**, 192 (12): 1809–1818

Kornek, M., Raskopf, E., Tolba, R., et al. (2008) Accelerated orthotopic hepatocellular carcinomas growth is linked to increased expression of pro-angiogenic and prometastatic factors in murine liver fibrosis. **Liver International**, 28 (4): 509–518

Ku, J.-L., Yoon, K.-A., Kim, I.-J., et al. (2002) Establishment and characterisation of six human biliary tract cancer cell lines. **British Journal of Cancer**, 87 (2): 1871–1893

Lakhtakia, R., Kumar, V., Reddi, H., et al. (2003) Hepatocellular carcinoma in a hepatitis B “x” transgenic mouse model : a sequential pathological evaluation. **Journal of Gastroenterology and Hepatology**, 18: 80–91

Laurent-Puig, P. and Zucman-Rossi, J. (2006) Genetics of hepatocellular tumors. **Oncogene**, 25: 3778–3786

Lazaridis, K.N. and Gores, G.J. (2005) Cholangiocarcinoma. **Gastroenterology**, 128: 1655–1667

Lee, J.W., Soung, Y.H., Kim, S.Y., et al. (2005) PIK3CA gene is frequently mutated in breast carcinomas and hepatocellular carcinomas. **Oncogene**, 24 (8): 1477–1480

Lerat, H., Honda, M., Beard, M.R., et al. (2002) Steatosis and liver cancer in transgenic mice expressing the structural and nonstructural proteins of hepatitis C virus. **Gastroenterology**, 122: 352–365

Li, M., Zhao, H., Zhang, X., et al. (2011) Inactivating mutations of the chromatin remodeling gene ARID2 in hepatocellular carcinoma. **Nature Genetics**, 43 (9): 828–829

Liang, J., Zubovitz, J., Petrocelli, T., et al. (2002) PKB/Akt phosphorylates p27, impairs nuclear import of p27 and opposes p27-mediated G1 arrest. **Nature Medicine**, 8 (10): 1153–1160

De Lima, V.M.R., Oliveira, C.P.M.S., Alves, V.A.F., et al. (2008) A rodent model of NASH with cirrhosis, oval cell proliferation and hepatocellular carcinoma. **Journal of Hepatology**, 49 (6): 1055–1061

Lin, H.-K., Chen, Z., Wang, G., et al. (2010) Skp2 targeting suppresses tumorigenesis by Arf-p53-independent cellular senescence. **Nature**, 464 (7287): 374–379

Liu, P., Cheng, H., Santiago, S., et al. (2011) Oncogenic PIK3CA-driven mammary tumors frequently recur via PI3K pathway-dependent and PI3K pathway-independent mechanisms. **Nature Medicine**, 17 (9): 1116–1120

Livezey, K.W. and Simon, D. (1997) Accumulation of genetic alterations in a human hepatoma cell line transfected with hepatitis B virus. **Mutation Research**, 377 (2): 187–198

Llovet, J.M., Chen, Y., Wurmbach, E., et al. (2006) A molecular signature to discriminate dysplastic nodules from early hepatocellular carcinoma in HCV cirrhosis. **Gastroenterology**, 131 (6): 1758–1767

Madisen, L., Zwingman, T.A., Sunkin, S.M., et al. (2010) A robust and high-throughput Cre reporting and characterization system for the whole mouse brain. **Nature Neuroscience**, 13 (1): 133–140

Magnuson, M. a. and Osipovich, A.B. (2013) Pancreas-specific Cre driver lines and considerations for their prudent use. **Cell Metabolism**, 18 (1): 9–20

Majumder, P.K., Grisanzio, C., O'Connell, F., et al. (2008) A prostatic intraepithelial neoplasia-dependent p27Kip1 checkpoint induces senescence and inhibits cell proliferation and cancer progression. **Cancer Cell**, 14 (2): 146–55

Maronpot, R.R. (2009) Biological basis of differential susceptibility to hepatocarcinogenesis among mouse strains. **Journal of Toxicologic Pathology**, 22 (1): 11–33

Marsh, V., Davies, E.J., Williams, G.T., et al. (2013) PTEN loss and KRAS activation cooperate in murine biliary tract malignancies. **Journal of Pathology**, 230 (2): 1651–73

Mazur, P.K., Grüner, B.M., Nakhai, H., et al. (2010) Identification of epidermal Pdx1 expression discloses different roles of Notch1 and Notch2 in murine KrasG12D-induced skin carcinogenesis in vivo. **PloS ONE**, 5 (10): e13578

McGlynn, K.A., Hunter, K., LeVoyer, T., et al. (2003) Susceptibility to aflatoxin B1-related primary hepatocellular carcinoma in mice and humans. **Cancer Research**, 63: 4594–4601

Medema, R.H., Kops, G.J., Bos, J.L., et al. (2000) AFX-like Forkhead transcription factors mediate cell-cycle regulation by Ras and PKB through p27kip1. **Nature**, 404 (6779): 782–787

Meng, F., Yamagiwa, Y., Ueno, Y., et al. (2006) Over-expression of Interleukin-6 enhances cell survival and transformed cell growth in human malignant chlangiocytes. **Journal of Hepatology**, 44 (6): 1055–1065

Michael, M.D., Kulkarni, R.N., Postic, C., et al. (2000) Loss of insulin signaling in hepatocytes leads to severe insulin resistance and progressive hepatic dysfunction. **Molecular Cell**, 6 (1): 87–97

Moriya, K., Fujie, H., Shintani, Y., et al. (1998) The core protein of hepatitis C virus induces hepatocellular carcinoma in transgenic mice. **Nature Medicine**, 4 (9): 1065–1067

Morris, S.M., Carter, K.T., Baek, J.Y., et al. (2014) TGF-β signaling alters the pattern of liver tumorigenesis induced by Pten inactivation. **Oncogene**, [Epub]: 1–10

Müsch, A. (2014) The unique polarity phenotype of hepatocytes. **Experimental Cell Research**, 328 (2): 276–283

Muzumdar, M.D., Tasic, B., Miyamichi, K., et al. (2007) A global double-fluorescent Cre reporter mouse. **Genesis**, 45: 593–605

Naas, T., Ghorbani, M., Alvarez-Maya, I., et al. (2005) Characterization of liver histopathology in a transgenic mouse model expressing genotype 1a hepatitis C virus core and envelope proteins 1 and 2. **Journal of General Virology**, 86: 2185–2196

Nakamura, K., Sakaue, H., Nishizawa, A., et al. (2008) PDK1 regulates cell proliferation and cell cycle progression through control of cyclin D1 and p27Kip1 expression. **The Journal of Biological Chemistry**, 283 (25): 17702–17711

Nakanishi, Y., Zen, Y., Kondo, S., et al. (2008) Expression of cell cycle-related molecules in biliary premalignant lesions: biliary intraepithelial neoplasia and biliary intraductal papillary neoplasm. **Human Pathology**, 39: 1153–1161

Nakazawa, K., Dobashi, Y., Suzuki, S., et al. (2005) Amplification and overexpression of c-erbB-2, epidermal growth factor receptor, and c-met in biliary tract cancers. **Journal of Pathology**, 206: 356–365

Nakeeb, A., Pitt, H., Sohn, T., et al. (1996) Cholangiocarcinoma. A spectrum of intrahepatic, perihilar, and distal tumors. **Annals of Surgery**, 224 (4): 463–475

Nault, J.C., Mallet, M., Pilati, C., et al. (2013) High frequency of telomerase reverse-transcriptase promoter somatic mutations in hepatocellular carcinoma and preneoplastic lesions. **Nature Communications**, 4: 2218

Noel, M.S. and Hezel, A.F. (2013) New and emerging treatment options for biliary tract cancer. **OncoTargets and Therapy**, 6: 1545–1552

O'Dell, M.R., Huang, J.L., Whitney-Miller, C.L., et al. (2012) KrasG12D and p53 mutation cause primary intrahepatic cholangiocarcinoma. **Cancer Research**, 72 (6): 1557–1567

Offield, M.F., Jetton, T.L., Labosky, P.A., et al. (1996) PDX-1 is required for pancreatic outgrowth and differentiation of the rostral duodenum. **Development**, 122: 983–995

Ohlsson, H., Karisson, K. and Edlund, T. (1993) IPF1, a homeodomain-containing transactivator of the insulin gene. **The EMBO Journal**, 12 (11): 4251–4259

Okabe, M., Ikawa, M., Kominami, K., et al. (1997) "Green mice" as a source of ubiquitous green cells. **FEBS Letters**, 407 (3): 313–319

Olaru, A. V, Ghiaur, G., Yamanaka, S., et al. (2011) A microRNA downregulated in human cholangiocarcinoma controls cell cycle through multiple targets involved in the G1/S checkpoint. **Hepatology**, 54 (6): 2089–2098

Ong, C.K., Subimerb, C., Pairojkul, C., et al. (2012) Exome sequencing of liver fluke–associated cholangiocarcinoma. **Nature Genetics**, 44 (6): 690–693

Palmieri, V.O., Grattagliano, I., Portincasa, P., et al. (2006) Systemic oxidative alterations are associated with visceral adiposity and liver steatosis in patients with metabolic syndrome. **The Journal of Nutrition**, 136: 3022–3026

Park, J.W., Park, D.M., Choi, B.K., et al. (2014) Establishment and characterization of metastatic gastric cancer cell lines from murine gastric adenocarcinoma lacking Smad4, p53, and E-cadherin. **Molecular Carcinogenesis**, [Epub]

Pawar, P., Ma, L., Byon, C.H., et al. (2009) Molecular mechanisms of tamoxifen therapy for cholangiocarcinoma: role of calmodulin. **Clinical Cancer Research**, 15 (4): 1288–1296

Dela Peña, A., Leclercq, I., Field, J., et al. (2005) NF-κB activation, rather than TNF, mediates hepatic inflammation in a murine dietary model of steatohepatitis. **Gastroenterology**, 129 (5): 1663–1674

Perraud, F., Dalemans, W., Gendrault, J.L., et al. (1991) Characterization of trans-immortalized hepatic cell lines established from transgenic mice. **Experimental Cell Research**, 195: 59–65

Plengsuriyakarn, T., Eursitthichai, V., Labbunruang, N., et al. (2012) Ultrasonography as a tool for monitoring the development and progression of cholangiocarcinoma in opisthorchis viverrini/dimethylnitrosamine-induced hamsters. **Asian Pacific Journal of Cancer Prevention**, 13: 87–90

Porstmann, T., Griffiths, B., Chung, Y.-L., et al. (2005) PKB/Akt induces transcription of enzymes involved in cholesterol and fatty acid biosynthesis via activation of SREBP. **Oncogene**, 24 (43): 6465–6481

Postic, C. and Magnuson, M. a. (2000) DNA excision in liver by an albumin-Cre transgene occurs progressively with age. **Genesis**, 26: 149–150

Postic, C., Shiota, M., Niswender, K.D., et al. (1999) Dual roles for glucokinase in glucose homeostasis as determined by liver and pancreatic beta cell-specific gene knock-outs using Cre recombinase. **The Journal of Biological Chemistry**, 274 (1): 305–315

Pratt, D. and Kaplan, M. (2000) Evaluation of abnormal liver-enzyme results in asymptomatic patients. **The New England Journal of Medicine**, 342 (17): 1266–1271

Pylayeva-Gupta, Y., Grabocka, E. and Bar-Sagi, D. (2011) RAS oncogenes: weaving a tumorigenic web. **Nature Reviews Cancer**, 11 (11): 761–774

R Development Core Team (2014) R: A language and environment for statistical computing. **R Foundation for Statistical Computing, Vienna, Austria.**

Radaeva, S., Ferreira-Gonzalez, A. and Sirica, A.E. (1999) Overexpression of C-NEU and C-MET during rat liver cholangiocarcinogenesis: a link between biliary intestinal metaplasia and mucin-producing cholangiocarcinoma. **Hepatology**, 29 (5): 1453–1462

Ran, F.A., Hsu, P.D., Lin, C.-Y., et al. (2013) Double nicking by RNA-guided CRISPR Cas9 for enhanced genome editing specificity. **Cell**, 154 (6): 1380–1389

Rangarajan, A. and Weinberg, R. a (2003) Comparative biology of mouse versus human cells: modelling human cancer in mice. **Nature Reviews Cancer**, 3 (12): 952–959

Rao, M.S. and Reddy, J.K. (1996) Hepatocarcinogenesis of peroxisome proliferators. **Annals of the New York Academy of Sciences**, 804: 573–587

Reichert, M., Saur, D., Hamacher, R., et al. (2007) Phosphoinositide-3-kinase signaling controls S-phase kinase-associated protein 2 transcription via E2F1 in pancreatic ductal adenocarcinoma cells. **Cancer Research**, 67 (9): 4149–4156

Riener, M.-O., Bawohl, M., Clavien, P.-A., et al. (2008) Rare PIK3CA hotspot mutations in carcinomas of the biliary tract. **Genes, Chromosomes & Cancer**, 47 (5): 363–367

Rizvi, S. and Gores, G.J. (2013) Pathogenesis, diagnosis, and management of cholangiocarcinoma. **Gastroenterology**, 145 (6): 1215–1229

Rocha, F.G., Lee, H., Katabi, N., et al. (2012) Intraductal papillary neoplasm of the bile duct: a biliary equivalent to intraductal papillary mucinous neoplasm of the pancreas? **Hepatology**, 56 (4): 1352–1360

Rogers, A. and Dintzis, R. (2012) **Comparative Anatomy and Histology - Chapter 13: Liver and gallbladder**. Treuting, P. and Dintzis, S. (eds.). Elsevier

Rountree, C.B., Ding, W., He, L., et al. (2009) Expansion of CD133-expressing liver cancer stem cells in liver-specific phosphatase and tensin homolog deleted on chromosome 10-deleted mice. **Stem Cells**, 27: 290–299

Rountree, C.B., Senadheera, S., Mato, J.M., et al. (2008) Expansion of liver cancer stem cells during aging in methionine adenosyltransferase 1A-deficient mice. **Hepatology**, 47 (4): 1288–1297

Sa, G. and Stacey, D.W. (2004) P27 expression is regulated by separate signaling pathways, downstream of Ras, in each cell cycle phase. **Experimental Cell Research**, 300 (2): 427–439

Sahin, F., Kannangai, R., Adegbola, O., et al. (2004) mTOR and P70 S6 kinase expression in primary liver neoplasms. **Clinical Cancer Research**, 10 (24): 8421–8425

Samatar, A. a and Poulikakos, P.I. (2014) Targeting RAS – ERK signalling in cancer : promises and challenges. **Nature Reviews Drug Discovery**, 13 (12): 928–942

Sandgren, E.P., Quaife, C.J., Pinkert, C.A., et al. (1989) Oncogene-induced liver neoplasia in transgenic mice. **Oncogene**, 4 (6): 715–724

Sanyal, A.J., Yoon, S.K. and Lencioni, R. (2010) The etiology of hepatocellular carcinoma and consequences for treatment. **The Oncologist**, 15 (suppl 4): 14–22

Sauer, B. and McDermott, J. (2004) DNA recombination with a heterospecific Cre homolog identified from comparison of the pac-c1 regions of P1-related phages. **Nucleic Acids Research**, 32 (20): 6086–6095

Schlitter, A.M., Born, D., Bettstetter, M., et al. (2014) Intraductal papillary neoplasms of the bile duct: stepwise progression to carcinoma involves common molecular pathways. **Modern Pathology**, 27 (1): 73–86

Schönhuber, N., Seidler, B., Schuck, K., et al. (2014) A next-generation dual-recombinase system for time- and host-specific targeting of pancreatic cancer. **Nature Medicine**, 20 (11): 1340–1347

Schulze, K., Imbeaud, S., Letouzé, E., et al. (2015) Exome sequencing of hepatocellular carcinomas identifies new mutational signatures and potential therapeutic targets. **Nature Genetics**, 47 (5): 505–511

Sell, S., Hunt, J.M., Dunsford, H. a, et al. (1991) Synergy between hepatitis B virus expression and chemical hepatocarcinogens in transgenic mice. **Cancer Research**, 51: 1278–1285

Serra, S. (2014) Precursor neoplastic lesions of the biliary tract. **Journal of Clinical Pathology**, 67 (10): 875–882

Shaib, Y. and El-Serag, H.B. (2004) The epidemiology of cholangiocarcinoma. **Seminars in Liver Disease**, 24 (2): 115–125

Shanmugasundaram, K., Block, K., Nayak, B.K., et al. (2013) PI3K regulation of the SKP-2/p27 axis through mTORC2. **Oncogene**, 32 (16): 2027–2036

Sheppard, K., Kinross, K.M., Solomon, B., et al. (2012) Targeting PI3 kinase/AKT/mTOR signaling in cancer. **Critical Reviews in Oncogenesis**. 17 (1) pp. 69–95

Sherr, C.J. (2004) Principles of tumor suppression. **Cell**, 116 (2): 235–246

Shibata, T. and Aburatani, H. (2014) Exploration of liver cancer genomes. **Nature Reviews Gastroenterology & Hepatology**, 11 (6): 340–349

Shimomura, I., Bashmakov, Y., Ikemoto, S., et al. (1999) Insulin selectively increases SREBP-1c mRNA in the livers of rats with streptozotocin-induced diabetes. **Proceedings of the National Academy of Sciences of the United States of America**, 96 (24): 13656–13661

Shin, I., Yakes, F.M., Federico, R., et al. (2002) PKD/Akt mediates cell-cycle progression by phosphorylation of p27Kip1 at threonine 157 and modulation of its cellular localization. **Nature Medicine**, 8 (10): 1145–1152

Simbolo, M., Fassan, M., Ruzzenente, A., et al. (2014) Multigene mutational profiling of cholangiocarcinomas identifies actionable molecular subgroups. **Oncotarget**, 5 (9): 2839–2852

Singal, A.K., Vauthey, J.-N., Grady, J.J., et al. (2011) Intra-hepatic cholangiocarcinoma--frequency and demographic patterns: thirty-year data from the M.D. Anderson Cancer Center. **Journal of Cancer Research and Clinical Oncology**, 137: 1071–1078

Sirica, A.E., Zhang, Z., Lai, G.H., et al. (2008) A novel “patient-like” model of cholangiocarcinoma progression based on bile duct inoculation of tumorigenic rat cholangiocyte cell lines. **Hepatology**, 47 (4): 1178–1190

Sopasakis, V.R., Liu, P., Suzuki, R., et al. (2010) Specific roles of the p110α isoform of phosphatidylinsositol 3-kinase in hepatic insulin signaling and metabolic regulation. **Cell Metabolism**, 11 (3): 220–230

Spence, J.R., Lange, A.W., Lin, S.C.J., et al. (2009) Sox17 regulates organ lineage segregation of ventral foregut progenitor cells. **Developmental Cell**, 17 (1): 62–74

Stahl, M., Dijkers, P.F., Kops, G.J.P.L., et al. (2002) The forkhead transcription factor FoxO regulates transcription of p27Kip1 and Bim in response to IL-2. **The Journal of Immunology**, 168 (10): 5024–5031

Steward, B. and Wild, C. (2014) **World Cancer Report 2014**. ISBN 978-92-832-0429-9

Stiles, B., Wang, Y., Stahl, A., et al. (2004) Liver-specific deletion of negative regulator Pten results in fatty liver and insulin hypersensitivity [corrected]. **Proceedings of the National Academy of Sciences of the United States of America**, 101 (7): 2082–2087

Suto, T., Habano, W., Sugai, T., et al. (2000) Aberrations of the K-ras, p53, and APC genes in extrahepatic bile duct cancer. **Journal of Surgical Oncology**, 73: 158–163

Suzuki, T., Takano, Y., Kakita, A., et al. (1993) An immunohistochemical and molecular biological study of c-erbB-2 amplification and prognostic relevance in gallbladder cancer. **Pathology - Research and Practice**, 189 (3): 283–292

Takahashi, Y., Soejima, Y. and Fukusato, T. (2012) Animal models of nonalcoholic fatty liver disease/nonalcoholic steatohepatitis. **World Journal of Gastroenterology**, 18 (19): 2300–2308

Tanaka, Y., Kanai, F., Tada, M., et al. (2006) Absence of PIK3CA hotspot mutations in hepatocellular carcinoma in Japanese patients. **Oncogene**, 25 (20): 2950–2952

Tang, T., Zheng, J.W., Chen, B., et al. (2007) Effects of targeting magnetic drug nanoparticles on human cholangiocarcinoma xenografts in nude mice. **Hepatobiliary & Pancreatic Diseases International**, 6 (3): 303–307

Taniguchi, C.M., Kondo, T., Sajan, M., et al. (2006) Divergent regulation of hepatic glucose and lipid metabolism by phosphoinositide 3-kinase via Akt and PKCλ/ζ. **Cell Metabolism**, 3 (5): 343–353

Tannapfel, A., Benicke, M., Katalinic, A., et al. (2000) Frequency of p16INK4A alterations and k-ras mutations in intrahepatic cholangiocarcinoma of the liver. **Gut**, 47: 721–727

Tapper, E.B., Jiang, Z.G. and Patwardhan, V.R. (2015) Refining the ammonia hypothesis: a physiology-driven approach to the treatment of hepatic encephalopathy. **Mayo Clinic Proceedings**, 90 (5): 646–658

Thorpe, L.M., Yuzugullu, H. and Zhao, J.J. (2015) PI3K in cancer: divergent roles of isoforms, modes of activation and therapeutic targeting. **Nature Reviews Cancer**, 15 (1): 7–24

Timmerbeul, I., Garrett-Engele, C.M., Kossatz, U., et al. (2006) Testing the importance of p27 degradation by the SCFskp2 pathway in murine models of lung and colon cancer. **Proceedings of the National Academy of Sciences of the United States of America**, 103 (38): 14009–14014

Tuveson, D. a, Shaw, A.T., Willis, N. a, et al. (2004) Endogenous oncogenic K-rasG12D stimulates proliferation and widespread neoplastic and developmental defects. **Cancer Cell**, 5: 375–387

Ueki, T., Hsing, A.W., Gao, Y., et al. (2004) Alterations of p16 and prognosis in biliary tract cancers from a population-based study in China. **Clinical Cancer Research**, 10 (5): 1717–1725

Valle, J., Wasan, H., Palmer, D.H., et al. (2010) Cisplatin plus gemcitabine versus gemcitabine for biliary tract cancer. **The New England Journal of Medicine**, 362 (14): 1273–1281

Vanhaesebroeck, B., Stephens, L. and Hawkins, P. (2012) PI3K signalling: the path to discovery and understanding. **Nature Reviews Molecular Cell Biology**, 13 (3): 195–203

Viglietto, G., Motti, M.L., Bruni, P., et al. (2002) Cytoplasmic relocalization and inhibition of the cyclin-dependent kinase inhibitor p27Kip1 by PKB/Akt-mediated phosphorylation in breast cancer. **Nature Medicine**, 8 (10): 1136–1144

Voss, J.S., Holtegaard, L.M., Kerr, S.E., et al. (2013) Molecular profiling of cholangiocarcinoma shows potential for targeted therapy treatment decisions. **Human Pathology**, 44 (7): 1216–1222

Wander, S. a, Zhao, D., Besser, A.H., et al. (2013) PI3K/mTOR inhibition can impair tumor invasion and metastasis in vivo despite a lack of antiproliferative action in vitro: implications for targeted therapy. **Breast Cancer Research and Treatment**, 138 (2): 369–381

Wang, X.W., Forrester, K., Yeh, H., et al. (1994) Hepatitis B virus X protein inhibits p53 sequence-specific DNA binding, transcriptional activity, and association with transcription factor ERCC3. **Proceedings of the National Academy of Sciences of the United States of America**, 91 (6): 2230–2234

Wang, Y., Lanzoni, G., Carpino, G., et al. (2013) Biliary tree stem cells, precursors to pancreatic comitted progenitors: evidence for possible life-long pancreatic organogenesis. **Stem Cells**, 31 (9): 1966–1979

Weisburger, E.K. (1977) Carcinogenicity studies on halogenated hydrocarbons. **Environmental Health Perspectives**, Vol. 21: 7–16

Weledji, E.P., Enow Orock, G., Ngowe, M.N., et al. (2014) How grim is hepatocellular carcinoma? **Annals of Medicine and Surgery**, 3 (3): 71–76

Whittaker, S., Marais, R. and Zhu, a X. (2010) The role of signaling pathways in the development and treatment of hepatocellular carcinoma. **Oncogene**, 29 (36): 4989–5005

Xu, R.F., Sun, J.P., Zhang, S.R., et al. (2011) KRAS and PIK3CA but not BRAF genes are frequently mutated in Chinese cholangiocarcinoma patients. **Biomedicine & Pharmacotherapy**, 65 (1): 22–26

Xu, X., Kobayashi, S., Qiao, W., et al. (2006) Induction of intrahepatic cholangiocellular carcinoma by liver-specific disruption of Smad4 and Pten in mice. **The Journal of Clinical Investigation**, 116 (7): 1843–1852

Xu, Y., Li, N., Xiang, R., et al. (2014) Emerging roles of the p38 MAPK and PI3K/AKT/mTOR pathways in oncogene-induced senescence. **Trends in Biochemical Sciences**, 39 (6): 268–276

Yang, G.S., Banks, K.G., Bonaguro, R.J., et al. (2009) Next generation tools for high-throughput promoter and expression analysis employing single-copy knock-ins at the Hprt1 locus. **Genomics**, 93 (3): 196–204

Yang, H., Li, T.W.H., Peng, J., et al. (2011) A mouse model of cholestasis-associated cholangiocarcinoma and transcription factors involved in progression. **Gastroenterology**, 141 (1): 378–388

Ying, H., Elpek, K.G., Vinjamoori, A., et al. (2011) PTEN is a major tumor suppressor in pancreatic ductal adenocarcinoma and regulates an NF-κB-cytokine network. **Cancer Discovery**, 1 (2): 158–169

Yu, D.Y., Moon, H.B., Son, J.K., et al. (1999) Incidence of hepatocellular carcinoma in transgenic mice expressing the hepatitis B virus X-protein. **Journal of Hepatology**, 31 (1): 123–132

Zen, Y., Adsay, N.V., Bardadin, K., et al. (2007) Biliary intraepithelial neoplasia: an international interobserver agreement study and proposal for diagnostic criteria. **Modern Pathology**, 20 (6): 701–709

Zender, S., Nickeleit, I., Wuestefeld, T., et al. (2013) A critical role for notch signaling in the formation of cholangiocellular carcinomas. **Cancer Cell**, 23: 784–795

Zhang, J., Han, C. and Wu, T. (2012) MicroRNA-26a promotes cholangiocacinoma growth by activation beta-catenin. **Gastroenterology**, 143 (1): 246–256

Zong, Y. and Stanger, B.Z. (2012) Molecular mechanisms of liver and bile duct development. **WIREs Developmental Biology**, 1 (5): 643–655

9 Acknowledgements

First of all, I thank Prof. Roland M. Schmid for giving me the opportunity to do my PhD research in his department, the II. Medizinische Klinik at Klinikum rechts der Isar.

Above all, I want to thank Prof. Dr. Dieter Saur for giving me the opportunity to do my PhD research in his group. He proposed this exciting research topic to me and always supported me and my project in any possible way, thus contributing considerably to the outcome of my thesis.

Further, I would like to thank my two thesis committee mentors PD Dr. Günter Schneider and PD Dr. Klaus-Peter Janssen for the fruitful discussions in the yearly thesis committee meetings and their suggestions for the advancement of the project.

I want to thank Dr. Katrin Offe and Desislava Zlatanova from the TUM Graduate Center for the great organization of the PhD Program Medical Life Science and Technology and their help with any questions concerning my graduation.

I am very thankful to Prof. Dr. Wilko Weichert and his coworkers from the Ruprecht-Karls-Universität in Heidelberg, who performed the p27 immunohistochemistry as well as histological analysis and quantification for me.

I give many thanks to Thomas Engleitner for all his advice and help concerning the statistical analysis of my data.

Many thanks to all members of the Saur, Schneider and Rad groups for the great working atmosphere in the lab and their constant help and support with any type of technical or scientific questions. I especially thank Stefan Eser and Vanessa Klein for the introduction to the project and techniques. Further, I would like to thank Dr. Sandra Diersch who started the p27 project. I am very thankful to Barbara Seidler for sharing her methodical experience, especially concerning cloning, with me. I further thank Vanessa Klein, Tatiana Schmid, Juliana Götzfried and Magdalena Zukowska for excellent technical support.

I want to thank all the animal keepers from the Zentrum für Präklinische Forschung for taking care of my mice and the nice collaboration.

Finally, I would like to thank my family for always supporting me and believing in me. I am very thankful to all my friends and especially to my boyfriend Markus for all the patience, understanding and help during the last years. Without them, my dissertation would not have been possible.